

4

DTIC FILE COPY

David Taylor Research Center

Bethesda, MD 20084-5000

DTRC-90/016 July 1990

Ship Hydromechanics Department
Research and Development Report

AD-A226 481

Computation of Incompressible Flow Around the DARPA SUBOFF Bodies

by

Joseph J Gorski
Roderick M. Coleman
Henry J. Haussling

DTRC-90/016 Computation of Incompressible Flow Around the DARPA SUBOFF Bodies



Approved for public release; distribution is unlimited.

90 07 14 215

MAJOR DTRC TECHNICAL COMPONENTS

CODE 011 DIRECTOR OF TECHNOLOGY, PLANS AND ASSESSMENT

12 SHIP SYSTEMS INTEGRATION DEPARTMENT

14 SHIP ELECTROMAGNETIC SIGNATURES DEPARTMENT

15 SHIP HYDROMECHANICS DEPARTMENT

16 AVIATION DEPARTMENT

17 SHIP STRUCTURES AND PROTECTION DEPARTMENT

18 COMPUTATION, MATHEMATICS & LOGISTICS DEPARTMENT

19 SHIP ACOUSTICS DEPARTMENT

27 PROPULSION AND AUXILIARY SYSTEMS DEPARTMENT

28 SHIP MATERIALS ENGINEERING DEPARTMENT

DTRC ISSUES THREE TYPES OF REPORTS:

1. **DTRC reports, a formal series**, contain information of permanent technical value. They carry a consecutive numerical identification regardless of their classification or the originating department.
2. **Departmental reports, a semiformal series**, contain information of a preliminary, temporary, or proprietary nature or of limited interest or significance. They carry a departmental alphanumeric identification.
3. **Technical memoranda, an informal series**, contain technical documentation of limited use and interest. They are primarily working papers intended for internal use. They carry an identifying number which indicates their type and the numerical code of the originating department. Any distribution outside DTRC must be approved by the head of the originating department on a case-by-case basis.

UNCLASSIFIED

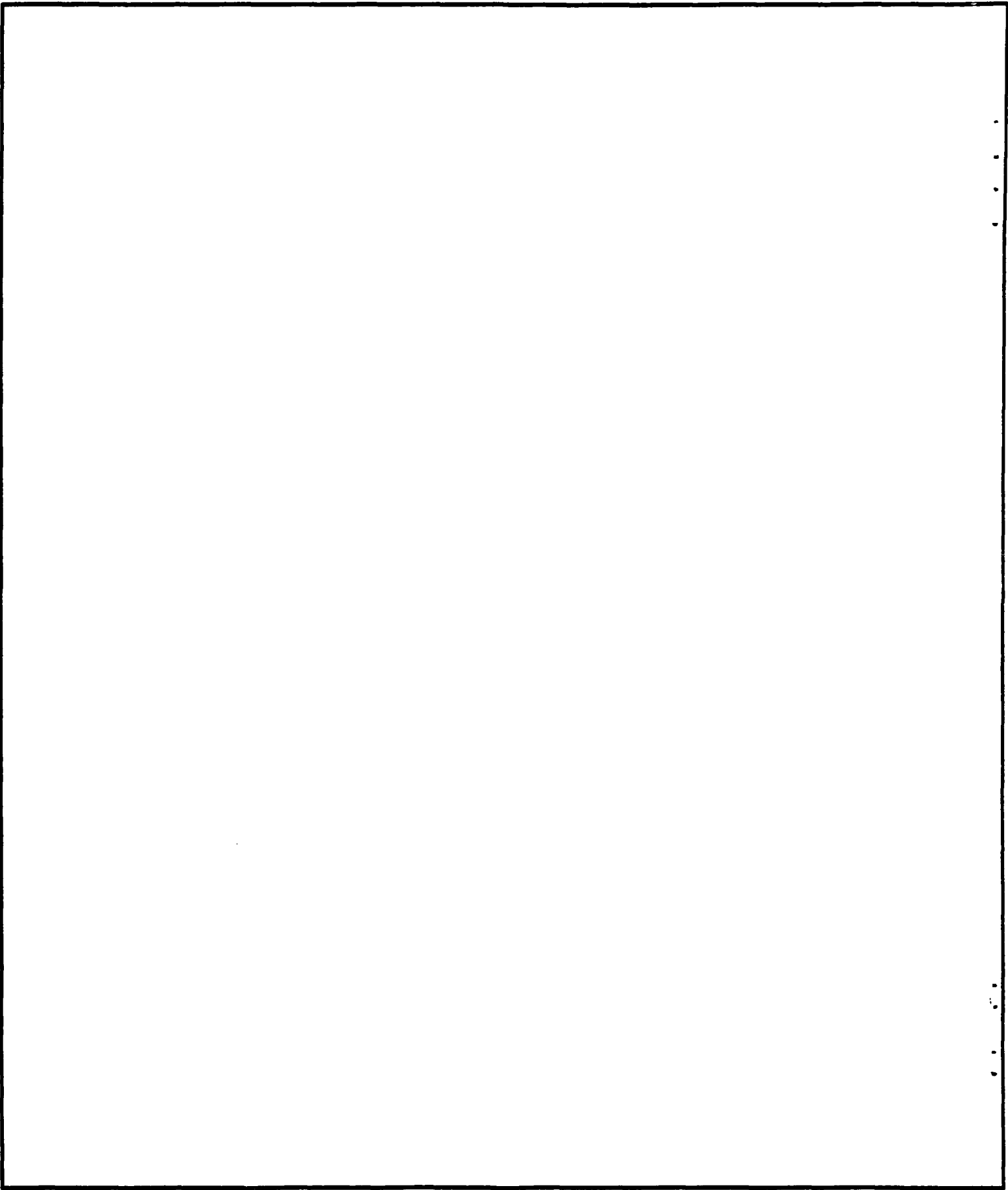
SECURITY CLASSIFICATION OF THIS PAGE

REPORT DOCUMENTATION PAGE

1a. REPORT SECURITY CLASSIFICATION UNCLASSIFIED			1b. RESTRICTIVE MARKINGS	
2a. SECURITY CLASSIFICATION AUTHORITY			3. DISTRIBUTION/AVAILABILITY OF REPORT Approved for Public Release; Distribution is Unlimited.	
2b. DECLASSIFICATION/DOWNGRADING SCHEDULE				
4. PERFORMING ORGANIZATION REPORT NUMBER(S) DTRC-90/016			5. MONITORING ORGANIZATION REPORT NUMBER(S)	
6a. NAME OF PERFORMING ORGANIZATION David Taylor Research Center		6b. OFFICE SYMBOL (If applicable) Code 1501	7a. NAME OF MONITORING ORGANIZATION	
6c. ADDRESS (City, State, and ZIP Code) Bethesda, MD 20084-5000			7b. ADDRESS (City, State, and ZIP Code)	
8a. NAME OF FUNDING/SPONSORING ORGANIZATION Research Projects Agency		8b. OFFICE SYMBOL (If applicable)	9. PROCUREMENT INSTRUMENT IDENTIFICATION NUMBER	
8c. ADDRESS (City, State, and ZIP Code) Submarine Technology Office, STP Support Office 1515 Wilson Blvd., Suite 805 Arlington, VA 22209			10. SOURCE OF FUNDING NUMBERS	
			PROGRAM ELEMENT NO. 63569N	PROJECT NO.
			TASK NO. S1974-030	WORK UNIT ACCESSION NO. DN509067
11. TITLE (Include Security Classification) Computation of Incompressible Flow Around the DARPA SUBOFF Bodies				
12. PERSONAL AUTHOR(S) Gorski, Joseph J., Roderick M. Coleman, and Henry J. Haussling				
13a. TYPE OF REPORT Final		13b. TIME COVERED FROM _____ TO _____		14. DATE OF REPORT (YEAR, MONTH, DAY) 1990, July
15. PAGE COUNT 88				
16. SUPPLEMENTARY NOTATION				
17. COSATI CODES			18. SUBJECT TERMS (Continue on reverse if necessary and identify by block number) DARPA SUBOFF Computational Fluid Dynamics Reynolds-Averaged Navier-Stokes Equations	
FIELD	GROUP	SUB-GROUP		
19. ABSTRACT (Continue on reverse if necessary and identify by block number) This report describes the application of the DTNS flow solvers, both axisymmetric (DTNSA) and three-dimensional (DTNS3D) versions, and the NUGGET grid generation code to the Defense Advanced Research Projects Agency (DARPA) SUBOFF bodies. This work was carried out at the David Taylor Research Center (DTRC) during FY89 and FY90.				
20. DISTRIBUTION/AVAILABILITY OF ABSTRACT <input type="checkbox"/> UNCLASSIFIED/UNLIMITED <input checked="" type="checkbox"/> SAME AS RPT <input type="checkbox"/> DTIC USERS			21. ABSTRACT SECURITY CLASSIFICATION UNCLASSIFIED	
22a. NAME OF RESPONSIBLE INDIVIDUAL Henry J. Haussling			22b. TELEPHONE (Include Area Code) (301) 227-1934	22c. OFFICE SYMBOL Code 1501

UNCLASSIFIED

SECURITY CLASSIFICATION OF THIS PAGE



CONTENTS

Page

ABSTRACT	1
ADMINISTRATIVE INFORMATION	1
INTRODUCTION	1
NUMERICAL FLOW SOLUTION	1
APPROACH	2
RESULTS	4
Unappended Body, Configuration 1	4
Body with Sail, Configuration 2	5
Body with Stern Appendages, Configuration 3	6
Body with Sail at a Two Degree Angle of Attack (Bow up), Configuration 4	7
Body with Sail at Two Degree Angle of Yaw, Configuration 5	8
Body with Ring Wing 1, Configuration 6	8
Body with Ring Wing 2, Configuration 7	9
Body with Sail and Stern Planes, Configuration 8	9
COMMENTS AND CONCLUSIONS	9
Comments on Flow Solution	9
Comments on Grid Generation	11
ACKNOWLEDGEMENTS	12
APPENDIX	75
REFERENCES	77

FIGURES

1. Unappended body with definition of coordinate system, configuration 1.	13
2. Grid in top centerplane for unappended body.	14
3. Cross-sectional grid surface for unappended body.	15
4. Computed pressure coefficient on unappended body.	16
5. Computed wall shear stress on unappended body.	17
6. Mean velocity profiles at $X/L = 0.978$ for unappended body.	18
7. Shear stress at $X/L = 0.978$ for unappended body.	19

FIGURES (Continued)

Page

8. Pressure coefficients on unappended body computed with coarse and fine grids.....	20
9. Streamwise velocity profiles at $X/L = 0.978$ for unappended body computed with coarse and fine grids.	21
10. Wall shear stresses for unappended body computed with coarse and fine grids.	22
11. Body with sail, configurations 2, 4, and 5.	23
12. Upper grid surface for body with sail.	24
13. Cross-sectional grid surface for body with sail.	25
14. Surface grid on sail with cap.	26
15. Cross-sectional grid surface for body with sail.	27
16. Particle traces computed with coarse grid for body with sail.	28
17. Particle traces computed with refined grid for body with sail.	29
18. Velocity vectors in the top center plane in front of the sail.	30
19. Detail of corner flow in the top center plane in front of the sail.	31
20. Crossflow velocity vectors at the base of the sail immediately downstream from the leading edge.	32
21. Crossflow velocity vectors at the base of the sail immediately downstream from the trailing edge.	33
22. Crossflow velocity vectors at the tip of the sail immediately downstream from the trailing edge.	34
23. Streamwise velocity profiles for body with sail at $X/L = 0.978$ and $R/R_{\max} = 0.25, 0.30, 0.35, 0.40, 0.50,$ and 0.60	35
24. Pressure coefficient on the sail at three heights.	36
25. Streamwise velocity profiles for body with sail at $X/L = 0.978$ computed with coarse and fine grids.	37
26. Pressure coefficients on the sail at $Y = 1.17$ feet computed with coarse and fine grids.	38
27. Pressure coefficients on the hull surface centerline upstream and downstream of the sail computed with coarse and fine grids.	39
28. Body with stern appendages, configuration 3.	40
29. Cross-sectional grid surface for body with stern appendages.	41
30. Particle traces for body with stern appendages.	42

FIGURES (Continued)

	Page
31. Crossflow velocity vectors at stern plane trailing edges.....	43
32. Crossflow velocity vectors at $X/L = 1.0$	44
33. Streamwise velocity profiles for body with stern appendages at $X/L = 0.978$ and $R/R_{\max} = 0.25, 0.30, 0.35, 0.40, 0.50$, and 0.60	45
34. Streamwise velocity profiles for body with stern appendages at $X/L = 0.978$ obtained with refined grid	46
35. Velocity vectors in the top center plane in front of the sail for an angle of attack of two degrees.	47
36. Crossflow velocity vectors immediately downstream from the sail trailing edge for an angle of attack of two degrees.	48
37. Crossflow velocity vectors near the tip of the sail immediately downstream from the trailing edge for an angle of attack of two degrees.	49
38. Streamwise velocity profiles at $X/L = 0.978$ and $R/R_{\max} = 0.25, 0.30, 0.35, 0.40, 0.50$, and 0.60 for body with sail at an angle of attack of two degrees.....	50
39. Mean velocity profiles in the top center plane at $X/L = 0.978$ for body with sail at an angle of attack of two degrees.	51
40. Crossflow velocity vectors at the sail trailing edge for an angle of yaw of two degrees.	52
41. Detail of the crossflow near the tip of the sail at the trailing edge for an angle of yaw of two degrees.	53
42. Crossflow velocity vectors downstream from the sail for an angle of yaw of two degrees.	54
43. Streamwise velocity profiles at $X/L = 0.978$ and $R/R_{\max} = 0.25, 0.30, 0.35, 0.40, 0.50$, and 0.60 for body with sail at an angle of yaw of two degrees.	55
44. Mean velocity profiles on the leeward side of the hull at $X/L = 0.978$ for body with sail at an angle of yaw of two degrees.	56
45. Mean velocity profiles in the top center plane at $X/L = 0.978$ for body with sail at an angle of yaw of two degrees.	57
46. Mean velocity profiles on the windward side of the hull at $X/L = 0.978$ for body with sail at an angle of yaw of two degrees.	58
47. Grid cross section in strut center plane of body with ring wing 1.	59
48. Velocity vectors in top center plane for body with ring wing 1.....	60
49. Crossflow velocity vectors at $X/L = 0.97$ for body with ring wing 1.	61

FIGURES (Continued)

Page

50. Streamwise velocity profiles at $X/L = 0.978$ and $R/R_{\max} = 0.22, 0.25, 0.30, 0.35,$ and 0.38 for body with ring wing 1.	62
51. Mean velocity profiles in the top center plane at $X/L=0.978$ for body with ring wing 1.	63
52. Pressure coefficient on hull and ring wing 1.	64
53. Velocity vectors in top center plane for body with ring wing 2.	65
54. Crossflow velocity vectors at $X/L = 0.97$ for body with ring wing 2.	66
55. Streamwise velocity profiles at $X/L = 0.978$ and $R/R_{\max} = 0.22, 0.25, 0.30, 0.35,$ and 0.38 for body with ring wing 2.	67
56. Mean velocity profiles in the top center plane at $X/L=0.978$ for body with ring wing 2.	68
57. Pressure coefficient on hull and ring wing 2.	69
58. Grid cross sections for hull with sail and stern planes, configuration 8.	70
59. Pressure coefficient on hull with sail and stern planes.	71
60. Pressure coefficient in stern plane region on hull with sail and stern planes.	72
61. Streamwise velocity profiles for body with sail and stern appendages at $X/L = 0.978$ and $R/R_{\max} = 0.25, 0.30, 0.35, 0.40, 0.50,$ and 0.60	73

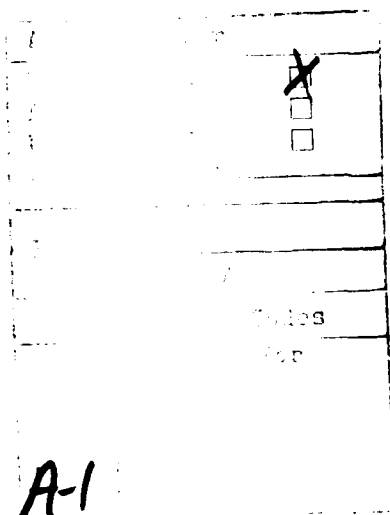


FIGURE 1. Streamwise velocity profiles for body with sail and stern appendages at $X/L = 0.978$ and $R/R_{\max} = 0.25, 0.30, 0.35, 0.40, 0.50,$ and 0.60 .

ABSTRACT

This report describes the application of the DTNS flow solvers, both axisymmetric (DTNSA) and three-dimensional (DTNS3D) versions, and the NUGGET grid generation code to the Defense Advanced Research Projects Agency (DARPA) SUBOFF bodies. This work was carried out at the David Taylor Research Center (DTRC) during FY89 and FY90.

ADMINISTRATIVE INFORMATION

This work was funded by DARPA under Task Area S1974-030, Program Element 63569N with internal DTRC Work Unit Numbers 1500-100 and 1501-310. The development of the computer codes and methodology was funded by the Office of Naval Research.

INTRODUCTION

The Reynolds-averaged Navier-Stokes (RANS) flow solving computer programs, known as the DTNS codes, were developed under the Numerical Analysis of Naval Fluid Dynamics Accelerated Research Initiative. This project, sponsored by the Office of Naval Research, began in FY86 and extends through FY90. The purpose of this project is to develop methods for the analysis of high Reynolds number flows in naval geometries in which viscous effects cannot be neglected or modelled by approximate formulations. The codes, including two-dimensional (DTNS2D), axisymmetric (DTNSA), and three-dimensional (DTNS3D) versions, were designed for easy use in computational fluid dynamics (CFD) analyses. Ease-of-use was accomplished by employing a multiblock approach to automate the treatment of arbitrary geometries. The input to each code contains the specification of the boundary conditions as well as the definition of the geometry in the form of a grid system. The Appendix gives an example of the boundary condition input for DTNS3D. As long as standard boundary conditions are employed and if Baldwin-Lomax or $k-\epsilon$ turbulence models are sufficient, little or no code development is needed no matter how complex the geometry. This generality means that these codes can be applied to a wide variety of flow problems including flows about bodies, local flows such as corner flows, and internal flows. The codes have been validated in a number of previous applications but DTNS3D, the latest development, until now has not been thoroughly exercised. Thus the DARPA-sponsored SUBOFF effort provided an excellent opportunity for validation and for determining whether these general codes can successfully treat a series of specific, related, and challenging geometries [1,2].

The DTNS codes can use any suitable structured grids, no matter how they are generated. The grids used in this work were developed with the INMESH (2D) and NUGGET (3D) elliptic grid generation programs. These codes use the generalized multiblock methodology pioneered by Coleman [3-5] which also forms the basis of the EAGLE and 3DGRAPE grid generation software. B-spline software was used for computer representation and manipulation of the body surfaces. This report gives a brief description of the numerical method, and summarizes the results and the experience gained in carrying out the computations.

NUMERICAL FLOW SOLUTION

Details of the numerical methods used in the DTNS codes have been presented elsewhere [6-10]. The Navier-Stokes equations for steady incompressible flow are solved using pseudo-compressibility where an artificial time dependence is added to the continuity equation. The equations are then marched in time until a steady state solution is achieved. When the steady state is reached all time derivative terms vanish and a solution of the equations for steady incompressible flow is obtained. The equations are discretized with the finite-volume formulation.

Central differencing is applied to the viscous terms but the high accuracy upwind total variation diminishing (TVD) scheme developed by Chakravarthy and Osher [6] is used on the convective terms. The Jacobian matrix of fluxes is used to create a set of eigenvectors and eigenvalues where fluxes are computed at the centers of cell surfaces. The upwind scheme divides the flux between neighboring cells into parts, each associated with an eigenvalue. Based on the signs of the eigenvalues the fluxes are differenced in the appropriate direction to achieve unconditional stability. A third-order accurate scheme is chosen. Flux limiting is used to prevent oscillations from creeping into the solution during start-up, but it is found that flux limiting is generally not needed for these incompressible flow computations. The codes include both Baldwin-Lomax and $k-\epsilon$ turbulence models. When the $k-\epsilon$ model is used, the TVD upwind differencing is also used on the $k-\epsilon$ equations [10]. The results presented here were obtained with the Baldwin-Lomax model.

The equations resulting from the upwind differencing are solved in an implicit coupled manner through the use of approximate factorization. The implicit part of the equations is discretized with a first-order accurate upwind scheme for the convective terms. This creates a diagonally dominant system which requires the inversion of block tridiagonal matrices. Since the implicit terms are zero upon convergence, the solution retains the high-order accuracy of the explicit part of the equations. A spatially varying time step, based on the local eigenvalues, is employed and CFL numbers up to ten have been used with success.

At downstream boundaries, velocity derivatives are set to zero and the static pressure is set to a constant outside of the wake and the pressure derivative is set to zero within the wake. At other outer boundaries, the velocity direction and magnitude are specified and the pressure derivative is set to zero. The outer boundaries were placed far enough away from the body that these simple far-field conditions would be sufficient. At walls the normal pressure derivative is set to zero. The equations are solved directly to all walls and standard no-slip conditions imposed. The law of the wall is not included in the setting of boundary conditions for the Navier-Stokes equations. The kinetic energy and dissipation in the $k-\epsilon$ equations are solved up to walls with the near wall formulation of Gorski [11].

The DTNS codes, which rely on high order accurate upwind differencing of the RANS equations, represent a deviation from the previously more widely used central differencing techniques. A discussion of some of the advantages and disadvantages of these different methods is included in the Comments and Conclusions section.

APPROACH

The following eight configurations were presented in reference 2:

1. Unappended body.
2. Body with fairwater.
3. Body with four stern appendages.
4. Body with fairwater at an angle of attack.
5. Body with fairwater at an angle of drift.
6. Body with ring wing 1.
7. Body with ring wing 2.
8. Body with fairwater and stern planes.

Preliminary calculations and validations were carried out with coarse grids on simplified ring wing geometries and on the unappended body supported by two struts above the tunnel wall [12].

Surface representation was carried out on Apollo workstations. Two computer programs DPOS and DPAC [13] were used for computer representation and manipulation of the body geometries and bounding surfaces along with another program for computing the intersecting curves of the appendages with the hull. These programs are based on a collection of B-spline subroutines developed at DTRC [14]. While these routines were adequate for this work, they need to be further generalized and integrated into a more comprehensive and interactive system. Only with such an investment will it be possible to carry out this time-consuming part of the CFD process with the efficiency made possible by state-of-the-art computer systems.

For the final SUBOFF calculations, grids were generated which were determined to offer a balance of resolution and computer processing time. The grid sizes were limited by the necessity of completing the computer runs on the heavily loaded CRAY 2 computer at the NASA-Ames Research Center in time to meet a rather restrictive deadline. Once the grids were completed, the grid size was halved in each direction. Axisymmetric flow solutions were first obtained using representative azimuthal planes with no appendages for the given coarse grids. These solutions were then rotated and used as the initial conditions for the three-dimensional calculations on the coarse grids. The coarse grid calculations were carried out on the CRAY-XMP computer at DTRC. Once a coarse grid solution was converged, it was interpolated onto the fine grid using bilinear interpolation. Since the fine grids have 8 times as many points as the coarse grids it was necessary to compute the fine grid solutions on the CRAY 2. For Configuration 1 a final grid of about 126,000 points was sufficient because of the axisymmetry of this case. For Configurations 2-7 the coarse grids consisted of about 62,500 points and the fine grids had up to approximately 500,000 points. Because of the necessity of resolving the flow about both a sail and stern planes, Configuration 8 required more grid points than the other cases. A 1,300,000 point grid was created for this Configuration as well as a coarse 160,000 point version. Results have been obtained for all Configurations; although those for Configuration 8 had not been analyzed at the time of the writing of this report. All calculations were performed with a Reynolds number of 12,000,000 based on body length. All calculations were carried out with the Baldwin-Lomax turbulence model. This model is not expected to be accurate in corner regions and in regions where strong vortices exist. However, at this time it is not clear whether the basic assumptions in the $k-\epsilon$ model will enable better results to be produced in these regions. This question will be investigated in the near future.

Grid cell aspect ratios are not now automatically controlled by the INMESH and NUGGET codes. There are plans to modify the codes in the near future to automatically provide quantitative information on aspect ratios as part of the output. The DTNS codes can routinely handle large aspect ratios but accuracy can be impaired by extreme cases. The grids created for these configurations have very large aspect ratios only in the far field where the flow is uniform.

Convergence of solutions with respect to grid size should be verified whenever possible. However, for large computations such as these, verification can be very difficult. The grids used were the largest that would allow computations to be completed within a given time frame and budget. Repeated calculations with successfully denser grids could not be carried out. However, since calculations for several of the configurations were carried out on a coarse version of the grid, some information on grid dependence is available. Comparisons of results with coarse and fine grids are presented in the next section.

Solutions are considered to be converged to steady state when velocity profiles remain unchanged over several hundred time steps. Residuals are typically reduced by two or three orders of magnitude during the duration of a flow calculation.

An Apollo workstation version of PLOT3D, developed at NASA-Ames, was used for flow visualization.

Five and a quarter inch floppy disks were used to transmit the calculated results to DARPA for comparison with experimental measurements and other calculations. These results include velocity and pressure values at locations on the body and in the flow field as specified by DARPA. The values were computed at the specified points through parametric trilinear interpolation among surrounding grid points.

RESULTS

Unappended Body, Configuration 1

Since the unappended DARPA2 body, as seen in Fig. 1, is defined as a body of revolution, calculations were first carried out using the axisymmetric DTNSA code and then repeated with DTNS3D for validation. For this purpose, a two-dimensional, two-block C-grid was generated first between the outline of the body in the (XY)-plane and a smooth outer boundary chosen to be a suitable distance away. The upper portion of this grid, shown in Fig. 2, was then rotated around one quarter of the body to provide 10 points in the azimuthal direction. This procedure yielded the fine grid - a three-dimensional, two-block C/O-grid with dimensions $129 \times 65 \times 10$ and $65 \times 65 \times 10$. Thus 126,100 points were used in the computational quarter-space. Fig. 3 shows part of a coordinate surface of a three-dimensional grid formed by rotating the two-dimensional grid around the *entire* DARPA2 body. In this and other figures, some of the grid points have been deleted to provide clearer illustrations.

The initial axisymmetric calculations took approximately 30 minutes on the CRAY-XMP. The axisymmetric solution was used as the initial condition for the three-dimensional calculation. The three-dimensional solution was computed within a half hour on the CRAY-XMP at DTRC. The speed of this calculation resulted from the similarity of the three-dimensional and axisymmetric numerical solutions. This similarity serves as a validation of the codes. The surface pressure distribution for this case is shown in Fig. 4, the wall shear stress in Fig. 5, the mean velocity profiles at $X/L = 0.978$ in Fig. 6, and the shear stress at $X/L = 0.978$ in Fig. 7. In these and following figures L represents the body length, R represents the normalized distance from the X-axis which is at the centerline of the hulls, R_o represents the radius of the hull at the X/L location under consideration, and R_{max} is the maximum radius of the hull. The velocities in the axial, radial, and azimuthal directions are represented by U_x , V_r , and W_θ , respectively. These and all subsequent calculations were done using the Baldwin-Lomax turbulence model. Because the Baldwin-Lomax model is an algebraic model which does not compute the kinetic energy, no estimates of the normal stresses are available for this or any of the other calculations. At a later date it would be worthwhile to compute some of these flows with the $k-\epsilon$ model to see if better results are obtainable with the more involved model.

To get a measure of the effects of grid resolution the unappended body flow was also computed with a coarse grid where every other point was removed in both the axial and radial directions. The surface pressure is almost identical in the solutions from the two grids except in the last 15% of the body length where there are slight differences (Fig. 8). There is more of a difference in the streamwise velocity profiles at $X/L = 0.978$ as shown in Fig. 9 even though here the two solutions are again quite similar. However, the wall shear stresses computed using the two different grids differ over the whole length of the body as shown in Fig. 10. These results indicate that many of the trends associated with the flowfields are well determined even by the coarse grid calculation. However, for detailed quantitative purposes the fine grid solution is necessary.

Body with Sail, Configuration 2

The body surface, sail surface, and sail cap, as seen in Fig. 11, were created from the analytical description given in reference 1. A curve of intersection, where the sail pierces the hull, was obtained using a numerical routine based on B-splines. A distribution of points was created along the upper portion of the hull centerline, both upstream and downstream of the sail, and along the sail/body intersection curve such that points were concentrated near the sail/body juncture. A grid, shown in Fig. 12, was then generated in the (XY)-plane above the body and on a hypothetical extension of the sail surface to the outer boundary used in Configuration 1. Another grid (2D) was generated in the (XY)-plane below the body. The upper grid was then rotated into the lower grid in a way that created a 3D grid with 49 azimuthal surfaces with concentration of these surfaces near the sail. A portion of this grid is illustrated in Fig. 13. Next, a fully three-dimensional grid was generated to fill the void between the cap of the sail and the outer boundary. The grid block above the cap was designed so that there could be an efficient transfer of flow information between grid cells directly above the sail and those outside this region. This requirement resulted in a sail/cap configuration as illustrated in Fig. 14. The final 500,000-point grid filled the half-space with 8 blocks fit together in a C/O-type arrangement with a 9th block above the sail cap as seen in Fig. 15.

A problem arises with the current version of the flow code when using the Baldwin-Lomax turbulence model with such a 9-block grid as this. The grid contains blocks upstream and downstream of the sail which extend from the body surface up to approximately the top of the sail. Other blocks extend from the top of these former blocks to the free-stream outer boundary. The Baldwin-Lomax modeling must extend into these outer blocks and be correctly related back to the body boundary within the inner blocks. However, this is a substantial programming task and has not yet been automated. To alleviate this problem inner and outer blocks are combined into larger blocks so that the Baldwin-Lomax model is in contact with a wall for determining the eddy viscosity. Therefore, this case was actually computed by combining several of the 9 blocks together and reducing the number to 5 blocks. Consequently, special coding was needed for block boundaries which involved more than one type of boundary condition. Thus, the generality of the multiblock feature of the code is currently somewhat limited when the Baldwin-Lomax model is used. It is less difficult to implement a general geometry capability with higher order turbulence models which do not need to relate every point in the flow field back to the nearest wall as required by simple algebraic models such as Baldwin-Lomax. The $k-\epsilon$ model has no difficulty crossing internal block boundaries, and thus the original 9-block grid could be used without any special coding.

The coarse grid results required about 2 hours of CRAY-XMP time after starting with the axisymmetric solution. Actually two coarse grid solutions were obtained: one with substantial clustering normal to the surface of the sail and one with almost no clustering. As can be seen in Fig. 16, which displays surface streamlines computed with the relatively unclustered grid, the horseshoe vortex at the base of the sail was not captured at all when the clustering was insufficient. With the same number of grid points, but with more clustering near the sail, a much more realistic streamline pattern was obtained as shown in Fig. 17. The limiting streamline on the hull around the sail is clearly visible.

The fine grid required approximately 6 hours to converge on the CRAY-2. In order to reduce execution time, a simple spatially varying time step was used that was based on the local eigenvalues.

Velocity vectors on the top center plane in front of the sail are shown in Fig. 18. The "user units" referred to in the vector plots represent the normalized free-stream velocity of one. Thus a

vector of length equal to the vector below Fig. 18 represents a flow speed of one. All lengths are normalized by the length of the body and the leading edge of the sail is located at approximately $X/L = 0.212$. From this figure it can be seen that there is considerable turning of the flow over the top of the sail and only a small leading edge horseshoe vortex is formed at the juncture of the sail and body. A blow-up of this leading edge horseshoe vortex can be seen in Fig. 19. Fig. 20 shows the velocity vectors in the (YZ) cross-plane immediately downstream of the leading edge of the sail. The crossflow vector plots are all presented looking forward (toward the bow), and except for Configuration 5, they would look identical if viewed from the bow. The center of the sail is located at $Z/L = 0.0$, and the sail extends upward from the body in the Y direction. The effect of the leading edge vortex can be seen here as the flow proceeds downward along the sail near its base and then outward away from the sail along the body. However, the vortex does not roll up in the classical sense which may be due to the combination of the curvature of the hull and the weakness of the leading edge vortex. Even though the vortex does not roll up, there is still a very distinct limiting streamline formed as seen in Fig. 17. In Fig. 21, which displays the velocity vectors in the cross plane immediately downstream of the trailing edge of the sail at $X/L = 0.306$, a secondary vortex can be seen along the body near the sail. Note that $Z/L = 0.0$ corresponds to the center plane. This vortex is rotating in the direction of the leading edge vortex but it does not form until near the trailing edge of the sail. Since the leading edge horseshoe vortex forces flow outward away from the sail, next to the body, it may only be downstream near the trailing edge of the sail that the curvature of the sail is sufficient enough to bring high momentum flow back toward the sail thus creating the vortex seen here. In Fig. 22, which displays the same cross section as Fig. 21, but higher up on the sail, a vortex can be seen near the tip of the sail, which is at approximately $Y/L = 0.105$. This tip vortex dissipates in the numerical results and is not apparent at the stern. Figure 23 shows streamwise velocity profiles at various R, versus θ at $X/L = 0.978$. In Fig. 23, and those following, the streamwise velocity increases with increasing R. The angle θ is defined to be zero in the top centerplane and positive on the port (positive Z) side of the hull and U_{ref} is the freestream velocity. The effect of the sail wake is noticeable in the v-shaped notches at $\theta = 0$ and the effect of the sail corner vortices is seen in the large humps in which these notches are imbedded. While the coarseness of even the fine grid used here has most likely distorted these results somewhat, it is encouraging that these two effects are retained this far downstream from the sail.

The pressure coefficient along the sail at three different Y locations is shown in Fig. 24. From this figure it appears that the flow along the sail behaves much like a two-dimensional flow except near the base and the tip of the sail. Comparisons of results obtained with the coarse (60,000 points) and fine (1/2 million points) grids are shown in Figs. 25 - 27. In Fig. 25 which presents streamwise velocity profiles, it can be seen that the two solutions are comparable near the top centerline of the hull but deviate away from the top. These conditions are not surprising as the grids were clustered around the top centerline to adequately resolve the flow around the sail but become significantly coarser away from the sail. There is almost no difference in the pressure distributions along the sail, at $Y = 1.17$ feet, computed with the two grids as shown in Fig. 26. As shown in Fig. 27, the two grids produce almost identical pressures along the top centerline in front of the sail but there is considerable difference behind the sail.

Body with Stern Appendages, Configuration 3

The body geometry is shown in Fig. 28. Computations were carried out in a quadrant bounded by planes passing through the centers of two of the stern appendages. Generation of the grid was done in basically the same way as the body/sail configuration. The stern appendages are different from the sail in that they have a nonuniform cross section and the tips are flat rather than rounded. All stern appendages were of the same shape and were at the same longitudinal position as given in the SUBOFF geometry report [1]. As before, a grid was generated in the upper (XY)-

plane with a bulge corresponding to the shape of an appendage extending from the appendage tip to the outer boundary. A similar grid was constructed in the (XZ)-plane accounting for the second appendage. The vertical grid was then rotated into the horizontal grid again giving a C/O-grid with 49 surfaces in the azimuthal direction with concentration near both appendages. Two 3D grid blocks were then fitted between the appendage's tips and the outer boundary to complete the 10-block, 525,000-point grid in the computational quarter-space. Details of the coarse grid (every other point deleted) in the stern plane region are shown in Fig. 29.

As for Configuration 2, to alleviate potential problems with the Baldwin-Lomax turbulence model several blocks were combined for the flow calculations. This resulted in the computations being performed on a 6 block grid. The computations required about 2.5 hours of computing time on the CRAY-XMP with the coarse grid which had about 65,000 points. Surface streamlines for this case, computed on the coarse grid, are shown in Fig. 30. Here again, limiting streamlines are clearly visible. In Fig. 31 cross-plane velocity vectors, at the trailing edge of the stern planes, show vortices formed at the tips of both stern planes. For this case one of the stern planes is centered on $Y/L = 0.0$ extending from the hull in the $-Z$ direction and the other is at $Z/L = 0.0$ extending in the Y direction. As can be seen in Fig. 32 the tip vortices persist to the stern but become fairly weak, most likely because of the coarseness of the grid. With calculations being carried out in the quadrant, it is necessary to resolve boundary layers on two appendages. Thus, for the same number of grid points, the resolution for this configuration is about half of that for Configuration 1. Figure 33 shows streamwise velocity profiles versus θ at $X/L = 0.978$ and $R/R_{\max} = 0.25, 0.30, 0.35, 0.40, 0.50$, and 0.60 . The weakness of the wake effect and the absence of corner vortex effects in these profiles is again attributed to the coarseness of the grid used for this configuration. To verify this attribution, the grid was refined by taking further advantage of symmetry to reduce the computational region to an octant and thereby double the resolution in the azimuthal direction. In addition, the resolution was further increased by doubling the number of points in the streamwise direction. The results obtained with this refined 120,000-point grid are displayed in Fig. 34. They show considerable improvement with the effects of the planes being much better represented at $X/L = 0.978$. Even further grid refinement would be necessary to obtain accurate profiles.

Body with Sail at a Two Degree Angle of Attack (Bow up), Configuration 4

The same grid was used here as was used for the body with sail in Configuration 2. The angle of attack was included merely by changing the input for the far-field boundary condition. Symmetry about $Z = 0.0$ allowed the computations to be confined to one half of the flow region. The coarse grid solution for the body with sail was used as the initial condition for this case. Convergence problems were encountered with the coarse grid because of the complicated nature of the flow near the trailing edge of the sail tip. Thus the grid was refined in the radial direction. This case took approximately 8 hours to converge on the CRAY-XMP. A rather small time step had to be used because of the complexity of the flow and the inadequacies of the grid near the tip of the sail. The leading edge horseshoe vortex is still quite small as can be seen in Fig. 35 which shows the velocity vectors in the plane of symmetry in front of the sail. Again a vortex is formed near the corner of the body and sail near the trailing edge of the sail and this vortex can be seen in the cross-plane velocity vectors just downstream from the trailing edge, as shown in Fig. 36. From these results it appears that the flow near the juncture of the body and sail is not changed significantly by the angle of attack. However, the tip vortex has disappeared as is evident in the blow up of the tip region shown in Fig. 37. Although there is still flow coming downward behind the sail, the upward motion of the free-stream outer flow must be enough to prevent a vortex from forming to the side of the sail tip. Figure 38 shows streamwise velocity profiles versus θ at $X/L = 0.978$ and $R/R_{\max} = 0.25, 0.30, 0.35, 0.40, 0.50$, and 0.60 . Mean velocity profiles versus radius at $X/L = 0.978$ and $\theta = 0$ are shown in Fig. 39.

Body with Sail at Two Degree Angle of Yaw, Configuration 5

In this case there is no symmetry in the flowfield and a grid covering the entire domain was used. For this purpose, the grid used for the body with sail at zero angle of attack was reflected about the $Z = 0.0$ plane. This resulted in a 10-block grid on which the calculations were performed. The results for Configuration 2 were used as an initial condition and the solution required about 5 hours on the CRAY-XMP for the coarse grid. Again the leading edge horseshoe vortex is very similar to that obtained for Configuration 2. However, the effect of the two degrees of yaw can be seen in Fig. 40 which shows velocity vectors in the cross-plane at the trailing edge of the sail. The two-degree yaw creates a small crossflow which moves from left to right (port to starboard) in the picture. Again the sail is at $Z/L = 0.0$ and extends upward from the body in the Y/L direction. The small corner vortex near the body is reduced by the crossflow on the upstream side of the sail and is increased on the downstream side of the sail. Due to the angle of yaw the tip vortices of equal strength on each side of the sail have been replaced with a strong vortex on the windward side and a much smaller counter-rotating vortex on the lee side as seen in Fig. 41. This vortex structure quickly dissipates with distance downstream (perhaps at least partially due to the coarseness of the grid) and a simpler crossflow field is obtained as shown in Fig. 42 which displays vectors in a plane about 10% of the body length downstream from the sail. Fig. 43 shows streamwise velocity profiles versus θ at $X/L = 0.978$ and $R/R_{\max} = 0.25, 0.30, 0.35, 0.40, 0.50$ and 0.60 . Mean velocity profiles versus radius at $X/L = 0.978$ and $\theta = -45, 0$ and 45 degrees are shown in Figs. 44-46, respectively.

Body with Ring Wing 1, Configuration 6

Initial calculations were carried out on the ring-wing geometries minus the struts that connect the ring wings to the body. This simplification allowed for two-dimensional grid generation with INMESH and axisymmetric flow solution with DTNSA. Results were reported in reference [12]. The axisymmetric grids consisted of eight two-dimensional blocks. A C-type configuration was used for the body with H-type topologies for the struts and ring wings. The three-dimensional calculations, including the struts, were limited to an octant by taking advantage of the symmetry of the geometry. The three-dimensional grids were generated first by rotating, through the octant of interest, seven of the grid blocks of the axisymmetric cases. Then NUGGET was used to generate three fully three-dimensional blocks to fit within the ring wing/strut/body region. Variable grid spacing was used to concentrate grid surfaces near the body, shroud, and strut surfaces. The two 10-block fine grids for ring wings 1 and 2 each contained about 412,000 grid points within the octant computed. A cross section of the grid in the strut center plane for ring wing 1 is displayed in Fig. 47.

About 2 hours were required on the CRAY-XMP to obtain a converged solution for ring wing 1 on the coarse grid and the fine grid solution required about 6 hours on the CRAY-2. Velocity vectors on the top center plane are shown in Fig. 48. Although the flow is well resolved in the streamwise direction, the fine grid has only 17 points in the azimuthal direction. However, for ring wing 1 a vortex is still resolved in the corner where the strut intersects the ring wing. This vortex is visible in Fig. 49, which shows velocity vectors in the crossflow plane at $X/L = 0.97$ just downstream from the strut which supports the ring wing. The strut centerline is located along the 45-degree line between the Y and Z axes. In the figure the effect of the ring wing on the flow is evident by the lack of flow in the radial direction at the top.

The streamwise velocity profiles versus θ at $X/L = 0.978$ and $R/R_{\max} = 0.22, 0.25, 0.30, 0.35$, and 0.38 are shown in Fig. 50. The "kinks" which appear in the profiles at $\theta = 0, \pm 90$, and ± 180 degrees are due to a lack of grid resolution in the azimuthal direction (the first grid point is approximately 10 degrees from the top centerplane). Mean velocity profiles versus radius at $X/L =$

0.978 and $\theta = 0$ degrees are shown in Fig. 51. The boundary layers on top of the ring wing and between the ring wing and the hull are clearly noticeable. The pressure coefficient on the inner and outer surfaces of the ring wing and along the hull in the vicinity of the ring wing is shown in Fig. 52.

Body with Ring Wing 2, Configuration 7

The velocity vectors in the top centerplane for this case are shown in Fig. 53. From Fig. 54, at $X/L = 0.97$, no vortex is noticeable in the corner where the strut intersects the ring wing. The streamwise velocity profiles versus θ at $X/L = 0.978$ and $R/R_{\max} = 0.22, 0.25, 0.30, 0.35$, and 0.38 are shown in Fig. 55. Again the "kinks" appear in the profiles at $\theta = 0, \pm 90$, and ± 180 degrees due to poor grid resolution in the azimuthal direction. Mean velocity profiles versus radius at $X/L = 0.978$ and $\theta = 0$ degrees are shown in Fig. 56. The boundary layers on top of the ring wing and between the ring wing and the hull are again clearly noticeable. The pressure coefficient on the inner and outer surfaces of the ring wing and along the hull in the vicinity of the ring wing is shown in Fig. 57.

Body with Sail and Stern Planes, Configuration 8

The geometric information that was developed for the body/sail configuration and the body/stern planes configuration was used to construct a grid for the fully appended body. The final 29-block grid, while similar to the earlier grids, required more points in both the longitudinal and azimuthal directions to provide the desired resolution for all the appendages. For this case, 161 points were needed along the body, while only 145 points were used in the previous cases. In the azimuthal direction, 97 points were used to resolve one-half of the body, twice the previous number. Part of the 1,300,000-point grid in the half-space can be seen in Fig. 58.

At the time of the writing of this report, the flow calculations had been completed on a coarse 160,000 point version of this grid and the results were in the process of being analyzed. Figures 59 and 60 are plots of the pressure coefficient on the hull. An apparent effect of the sail on the stern planes can be seen in the smaller area of low pressure (dark green) on the top plane as compared with the others planes. Streamwise velocity profiles versus θ at $X/L = 0.978$ are shown in Fig. 61. While these profiles reflect the presence of the stern planes and even the sail, it is to be expected that, as with Configuration 3 (Figs. 33 and 34), much of the effect of the appendages has been lost here too because of the coarseness of the grid.

COMMENTS AND CONCLUSIONS

The DARPA SUBOFF program provided an excellent opportunity to examine the applicability of the DTNS RANS flow solvers as well as the surface representation and grid generation software. The results are very encouraging in that all of the geometries could be treated with this general software. The generation of complicated flow phenomena, such as vortices, was predicted realistically. The downstream convection of these phenomena, such as from the sail to the propeller plane, was captured in spite of the coarseness of the grids. But, it has also been shown that the ability to accurately capture and track the vortices formed is directly related to the grid resolution. Satisfactory results cannot be obtained without suitably dense grids and correspondingly adequate computer resources. The accuracy of the results will be determined by their comparison with the SUBOFF experimental data and with other computations.

Comments on Flow Solution

No method for solving the Navier-Stokes equations is perfect and each has its individual advantages and disadvantages. Central difference techniques have proven quite useful over the years and a central difference code, ISFLOW, has been developed at DTRC and applied to

submarine geometries [15]. The experience gained with both ISFLOW and the DTNS codes has shown that both central difference and upwind methods can be useful. Central difference techniques tend to consume less computer time than upwind schemes because they are less involved and often converge faster due to added dissipation. Thus they can yield an efficient capability for specific geometries such as appended bodies.

While central difference methods are very useful, considerable experience is necessary to adjust the amount of dissipation to achieve numerical stability. Although the DTNS codes are more complex than central difference codes and are more expensive to run, these negative factors are offset by the avoidance, through the use of upwind differences, of the complications of added dissipation. Since there is no added artificial dissipation to adjust, there are no arbitrary parameters to set. Therefore as long as the code works for one geometry it will work (within the limits of the present turbulence models) for any geometry as long as there is adequate grid resolution. Since no parameters, except the Reynolds number and perhaps the time step, need to be changed for any of the calculations, upwind differencing has rapidly become the choice of researchers on computational fluid dynamics for compressible flows. Similarly, the DTNS codes represent a major step forward in the development of useful predictive tools for all manner of incompressible fluid flows. This is a contrast to some of the previous methods which often need some baseline calculations in order to set parameters before accurate results can be obtained for a particular configuration.

Most of the RANS solutions obtained to date have been for steady flow situations. While there are important questions about the physical significance of unsteady RANS solutions, there is considerable interest in such solutions because of the importance of unsteady phenomena. Another advantage of the upwind techniques is that the diagonal dominance of the resulting systems of equations facilitates use of the methods to obtain unsteady solutions. The development of unsteady versions of the DTNS codes is currently underway and two-dimensional unsteady solutions are already being obtained.

In these SUBOFF applications DTNSA and DTNS3D were shown to be quite robust. Even though the codes were not developed specifically for these geometries, no fundamental difficulties were encountered in applying them to any of the geometries presented here as well as to an experimental configuration including supporting struts and tunnel floor [12]. All of the calculations demonstrated in this report were obtained with little or no recoding of the basic DTNS3D flow solver. Most of the boundaries could be accommodated with simple single line inputs as demonstrated in the appendix. Once a grid was generated the flow fields were relatively easy to obtain simply by prescribing the correct boundary conditions with the input. No parameters needed to be changed for any of the flow calculations except the time step, which had to be reduced for some cases because of stability considerations due to the complexity of the flow or the inadequacies of the grid. With computer codes such as this, where no arbitrary constants need to be modified for different flow computations, it is becoming increasingly easier for researchers with little computational fluid dynamics programming experience to compute complex flow fields. Navier-Stokes flow solvers must become more easily usable if they are ever going to become useful engineering tools and not remain merely specialized research codes. The authors feel that the integration of powerful grid generation tools such as NUGGET with general flow solvers such as DTNS3D is clearly a step in this direction.

To be useful, Navier-Stokes flow solvers also have to be efficient and accurate. By using a third order accurate scheme, the DTNS codes should fairly accurately represent the flow fields. Accuracy is lost somewhat near the boundaries but this can be offset by clustering of the grid points. Future work should investigate methods to extend the accuracy of high-order schemes to

the boundaries.

Another problem with using high-order accurate solvers is that they take extra computer time. Faster schemes which are still highly accurate and easy to use must be developed. The present codes use approximate factorization in all directions which is only conditionally stable. Convergence may be accelerated considerably by using a scheme such as LU-SSOR decomposition, which is unconditionally stable in three-dimensions. Such an approach should be investigated.

The most significant inadequacy of the present codes, and all other Reynolds-averaged Navier-Stokes solvers, is the lack of an adequate turbulence model. The Baldwin-Lomax model used here was developed for simple two-dimensional plate flows and clearly cannot model many of the complex flow patterns present in these flows such as separation, strong curvature effects, leading edge horseshoe vortices, and tip vortices to name a few. The $k-\epsilon$ model may perform better and it could be investigated with the present DTNS3D code with a minimum of effort if desired. In fact, the only reason why results computed with the $k-\epsilon$ model haven't yet been obtained for these geometries is the lack of time. However, even the $k-\epsilon$ turbulence model will be inadequate for many of these complex flow phenomena because of the underlying assumptions of isotropic flow. Significant research still needs to be done on developing good turbulence models for complex flows. Otherwise the next generation of Navier-Stokes flow solvers, which will be more efficient, more accurate, and easier to use, may be of limited use because of the inadequacy of the turbulence models in the complex flow areas of maximum interest.

Comments on Grid Generation

When a powerful flow code such as DTNS3D is available the majority of the human labor needed to obtain a solution is involved with the preprocessing of the geometry. For this reason, the tools available for grid generation and surface representation determine, to a large extent, the length of the overall CFD process. Investments in improving these tools will have a high payoff in the form of increased productivity of CFD investigators.

Because two-dimensional grids are easier to generate and control than fully three-dimensional grids, they should be manipulated (rotated, translated, stacked, etc.) to create the final three-dimensional grids whenever possible. A good two-dimensional grid generation capability is a must for efficient three-dimensional grid generation since two-dimensional grids are the main input to the three-dimensional grid generation process.

The shapes of the body and appendages were given in equation form in Reference 1 along with the location of the appendages on the body. Since the surfaces involved were relatively simple, they could be generated by rotations and translations of the appropriate plane curves given by the equations. However, after the appendages have been intersected with and joined to the body, it is a more difficult task to construct suitable surface grids needed as input to the elliptic grid generation procedure. As a result of such difficulties and the time constraints imposed on this project, the grids that were used represent a compromise, in both accuracy and efficiency, when compared with the ideal grids that could have been created with the expenditure of more time and labor. Improved interactive software will make it feasible to create better grids with reasonable effort. For instance, C-type, rather than H-type, grids should be used to more efficiently resolve the details of the flow around appendages with blunt leading edges. Such C-grids can certainly be created with the existing software. However, the efficient production of large grids involving imbedded C-grids calls for a rather powerful surface grid generation tool, one that facilitates the positioning of points in arbitrary patterns on complex surfaces. For now it is often more convenient to use algebraic procedures to create H-type surface grids on the bodies around appendage junctures since these procedures are simpler and easier to use.

Most of the cases were run on both coarse and fine grids in order to assess the effect of grid size on the efficiency of the program and the accuracy of the solution. The fine grids capture the details of the flow better than the coarse grids. Convergence of the solution to a steady state on the fine grid was accelerated through the use of an initial guess interpolated from the coarse grid solution. It is probable that in most cases the solution computed on a grid could be improved by a redistribution of the grid points without increasing their number. For example, concentrating points in the regions just downstream from the appendage tips and where the appendages join the body should provide better definition of the vortices. The ability to redistribute points quickly and efficiently as well as the ability to create more complex grid configurations such as imbedded grids are goals of research in grid generation that will lead to improved solutions at less cost.

ACKNOWLEDGEMENTS

The authors acknowledge with gratitude the contributions of Mr. Ronald Miller, who improved the Apollo version of PLOT3D and computed the SUBOFF submission data from the raw results, and Mr. Steven Fisher, who developed the interpolation software used in the data conversion process. CRAY-XMP computer time was supplied by the David Taylor Research Center and CRAY-2 time was provided by the Numerical Aerodynamics Simulation Program of the National Aeronautics and Space Administration.

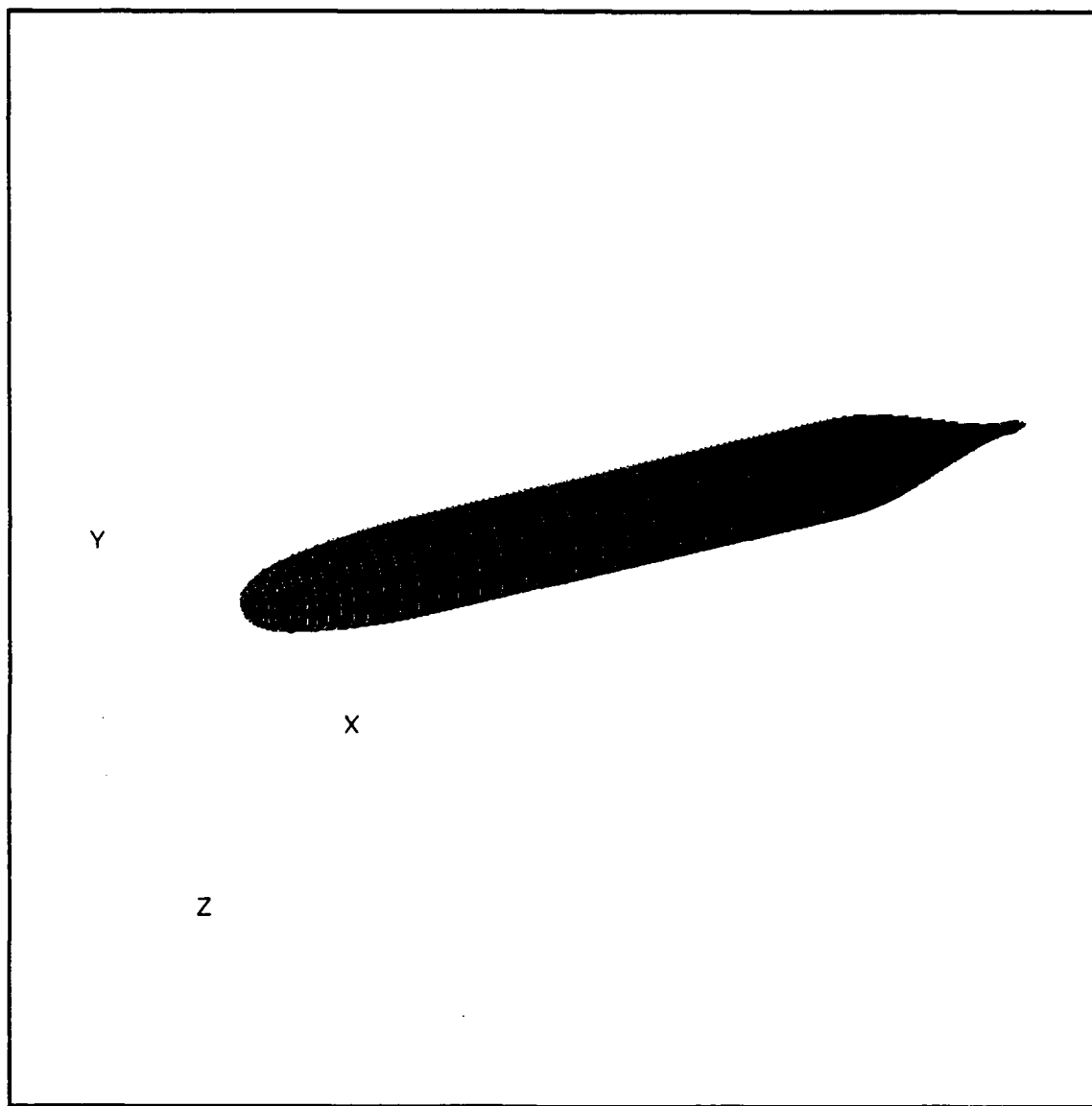


Fig. 1. Unappended body with definition of coordinate system, configuration 1.

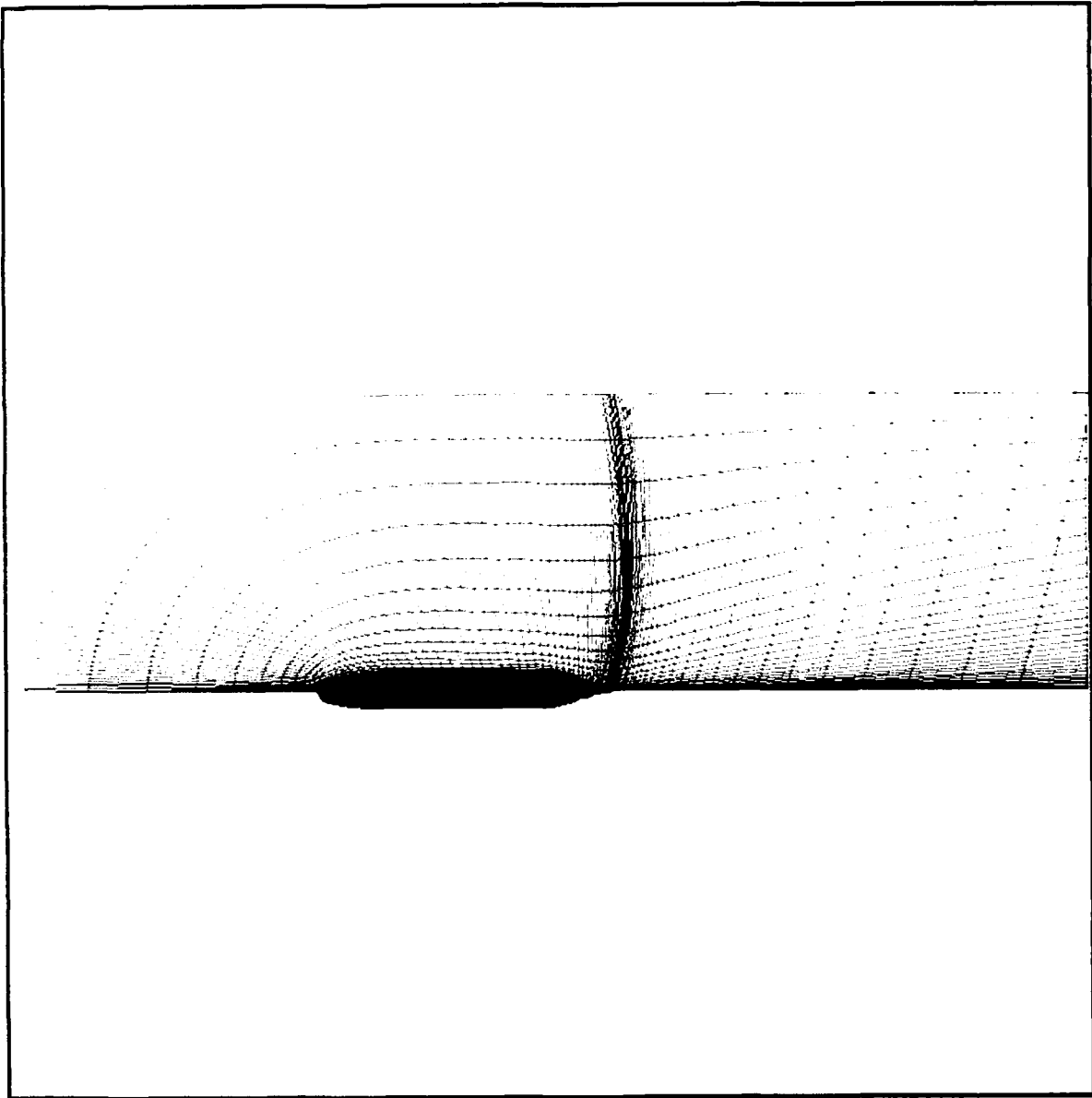


Fig. 2. Grid in top center plane for unappended body.

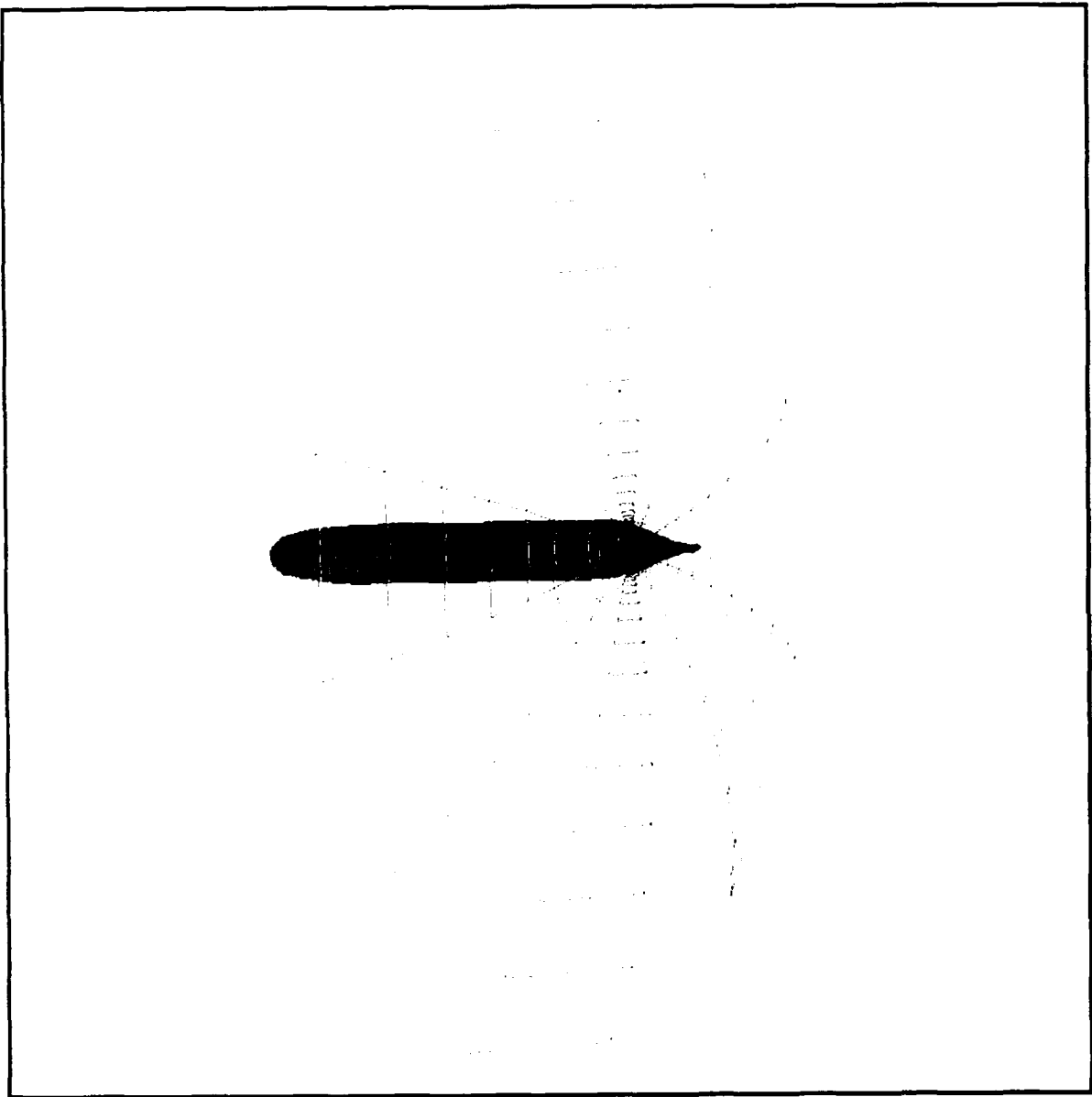


Fig. 3. Cross-sectional grid surface for unappendaged body.

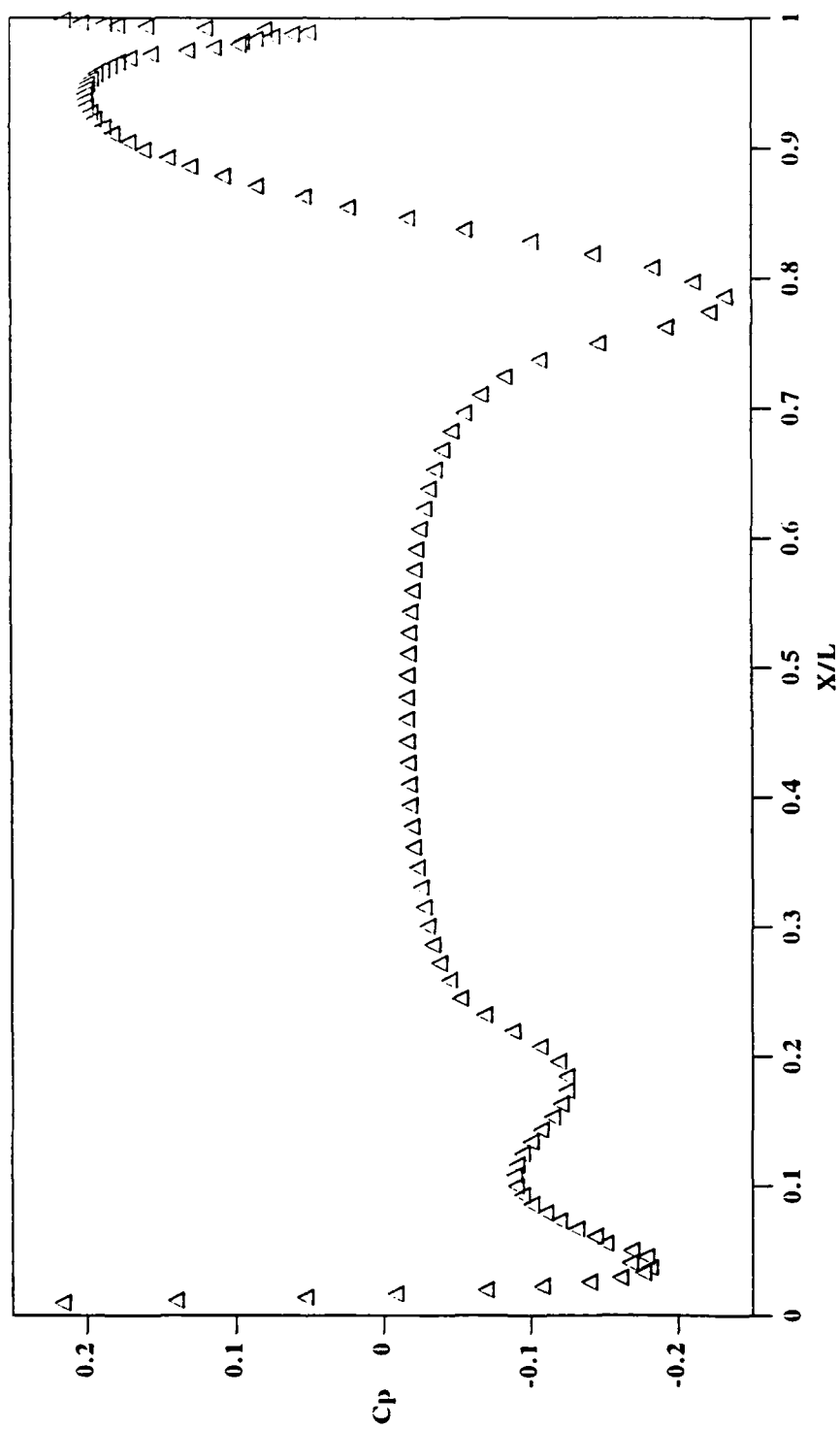


Fig. 4. Computed pressure coefficient on unappended body.

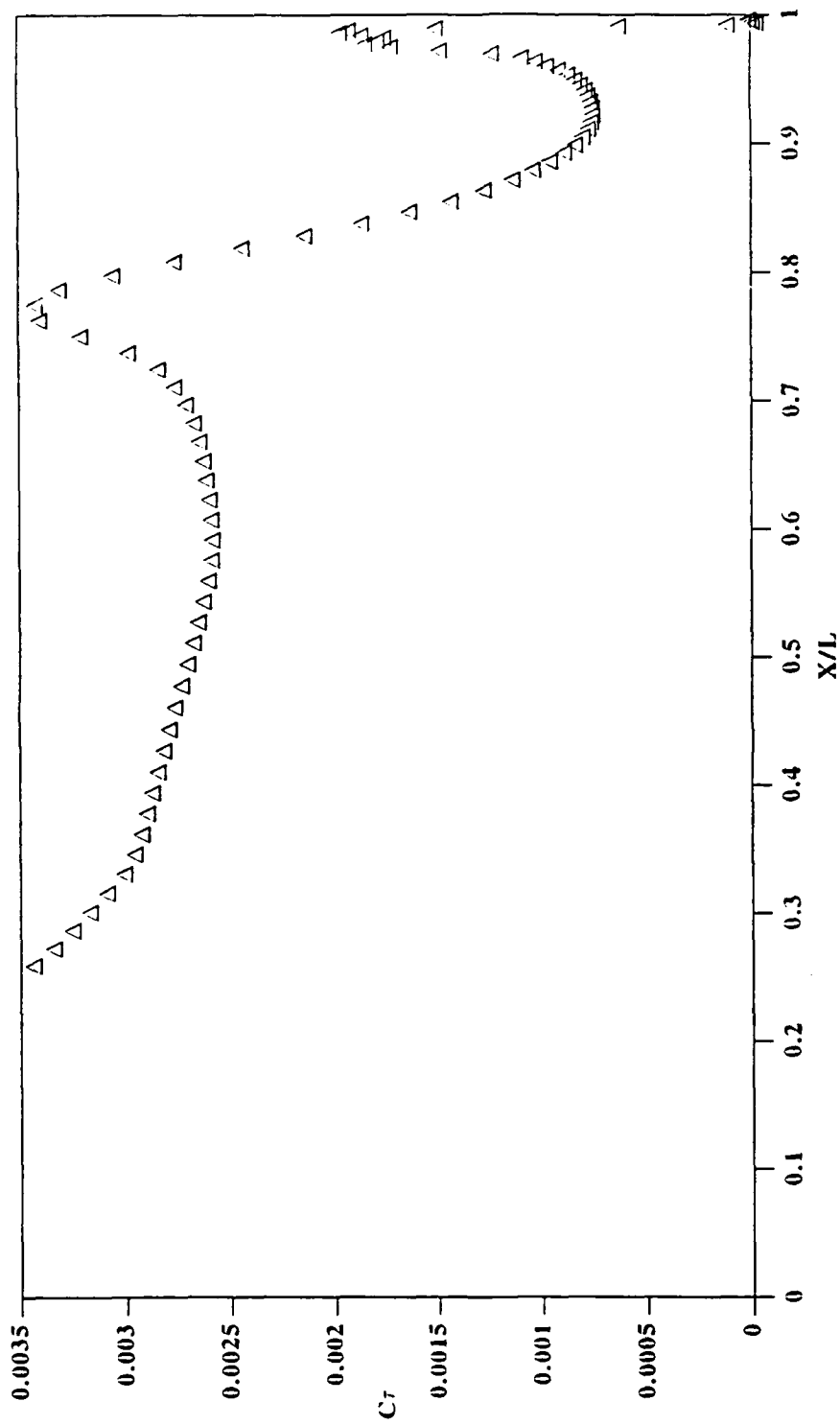


Fig. 5. Computed wall shear stress on unappended body.

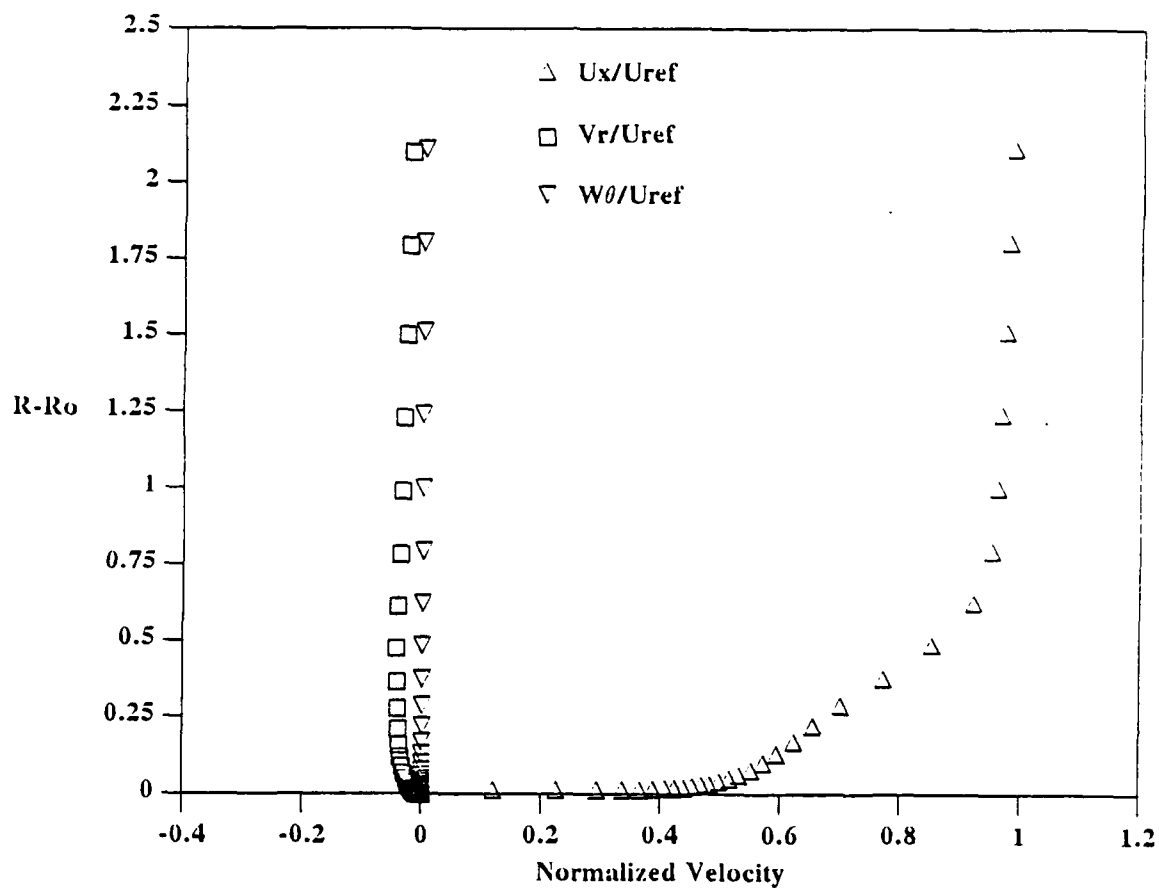


Fig. 6. Mean velocity profiles at $X/L = 0.978$ for unappended body.

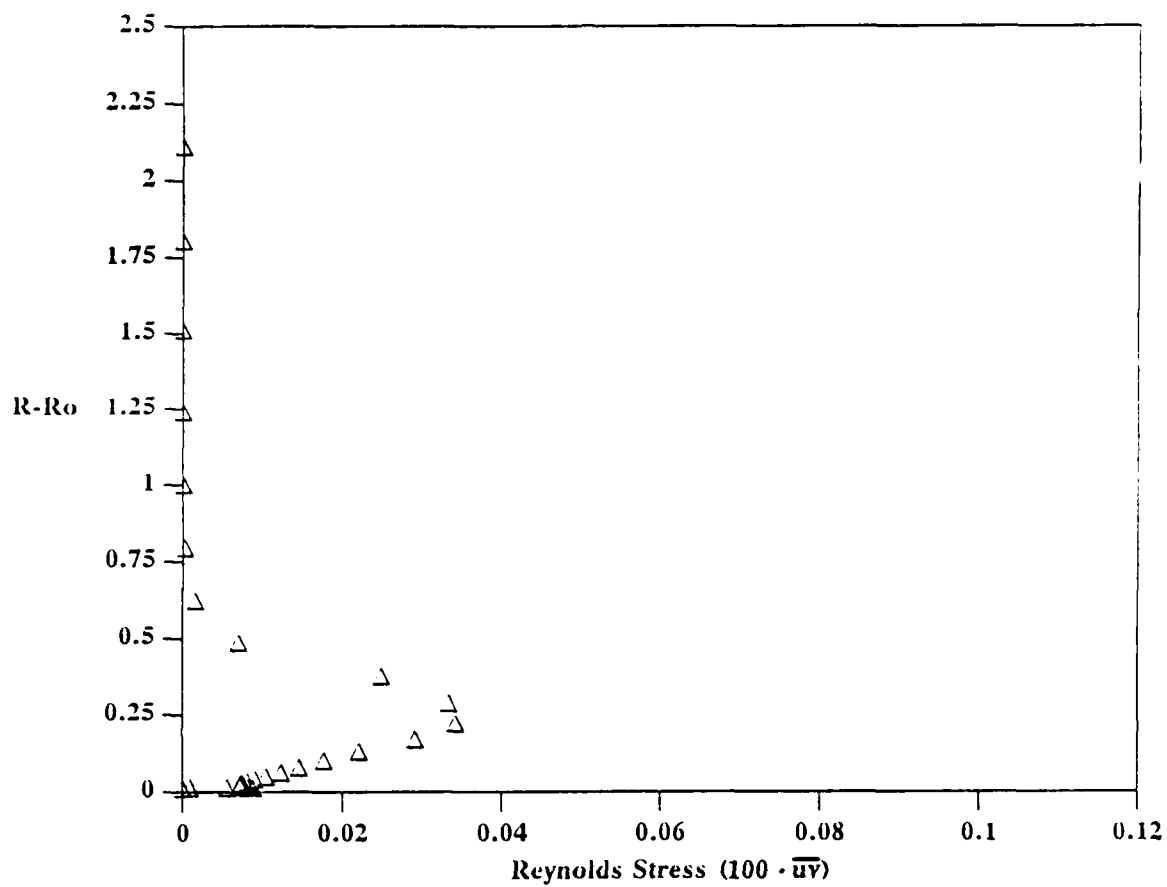


Fig. 7. Shear stress at $X/L = 0.978$ for unappended body.

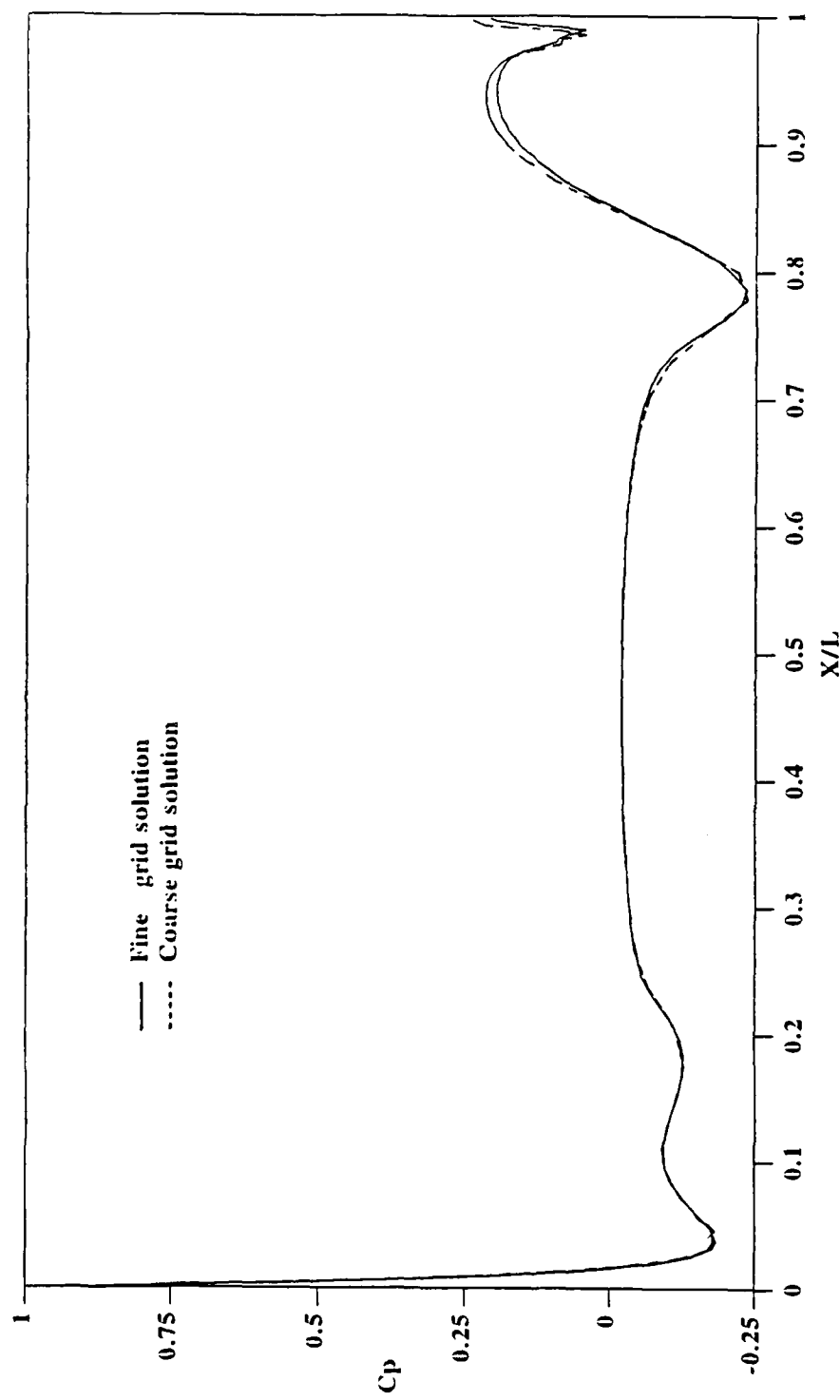


Fig. 8. Pressure coefficients on unappended body computed with coarse and fine grids.

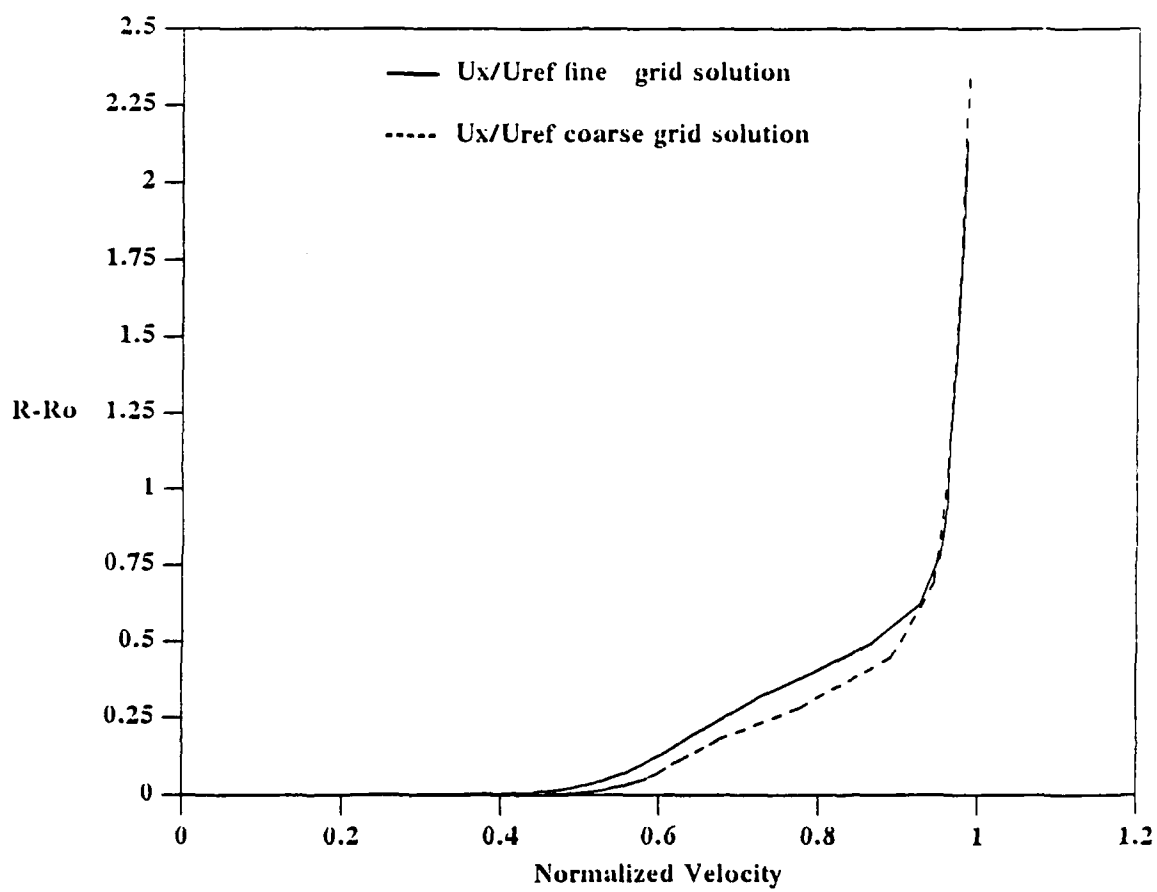


Fig. 9. Streamwise velocity profiles at $X/L = 0.978$ for unappended body computed with coarse and fine grids.

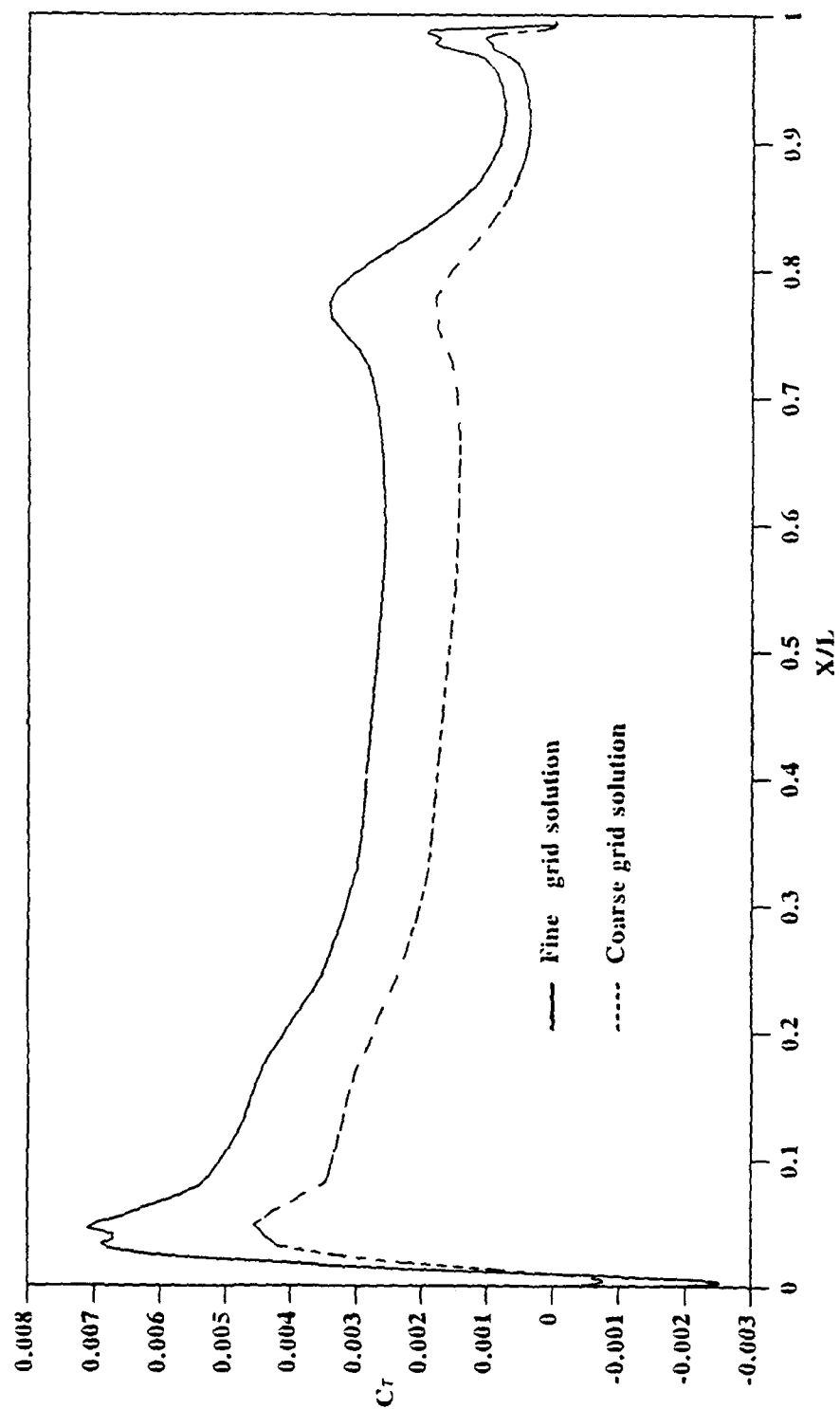


Fig. 10. Wall shear stresses for unappended body computed with coarse and fine grids.

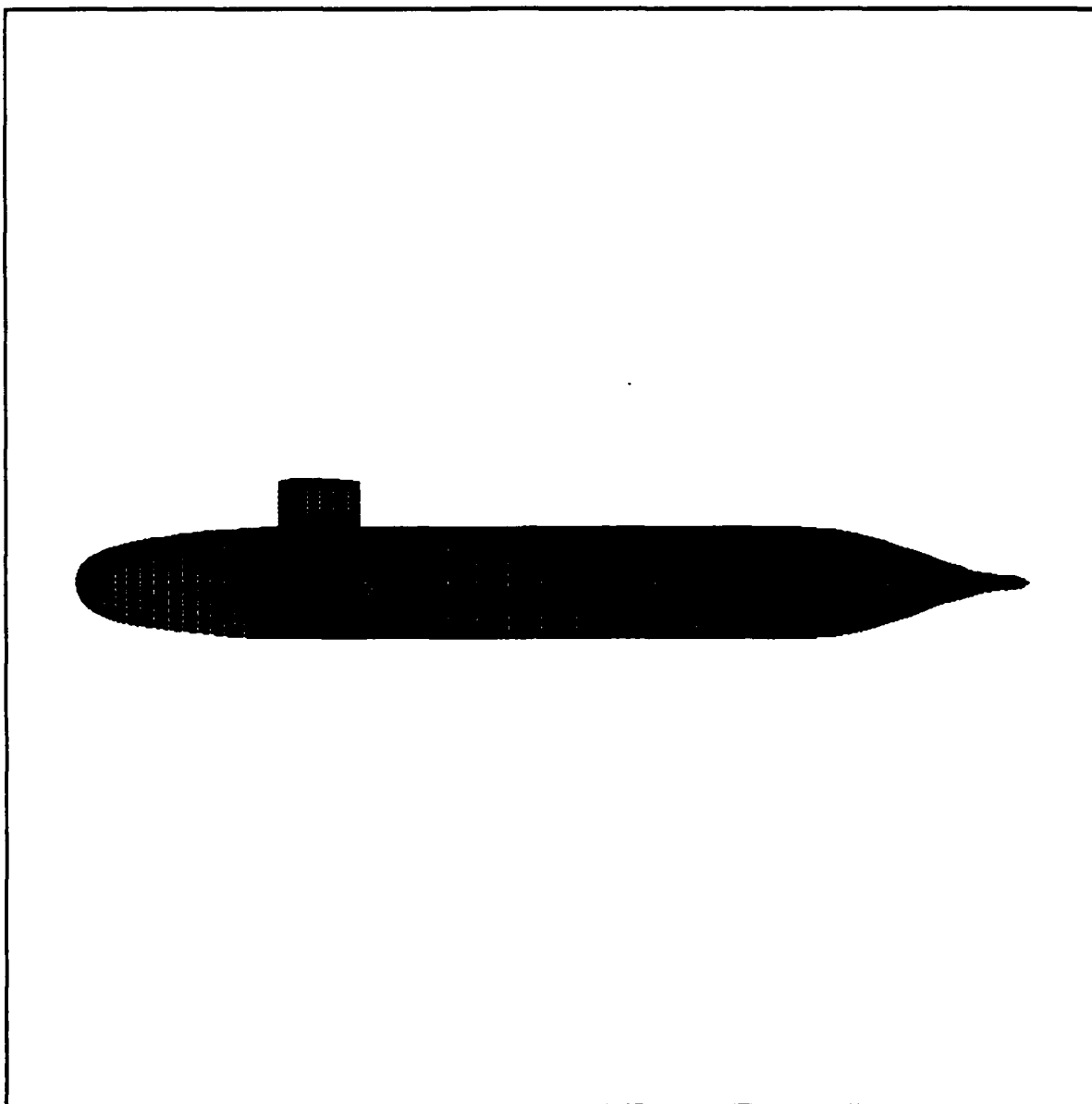


Fig. 11. Body with sail, configurations 2, 4, and 5.

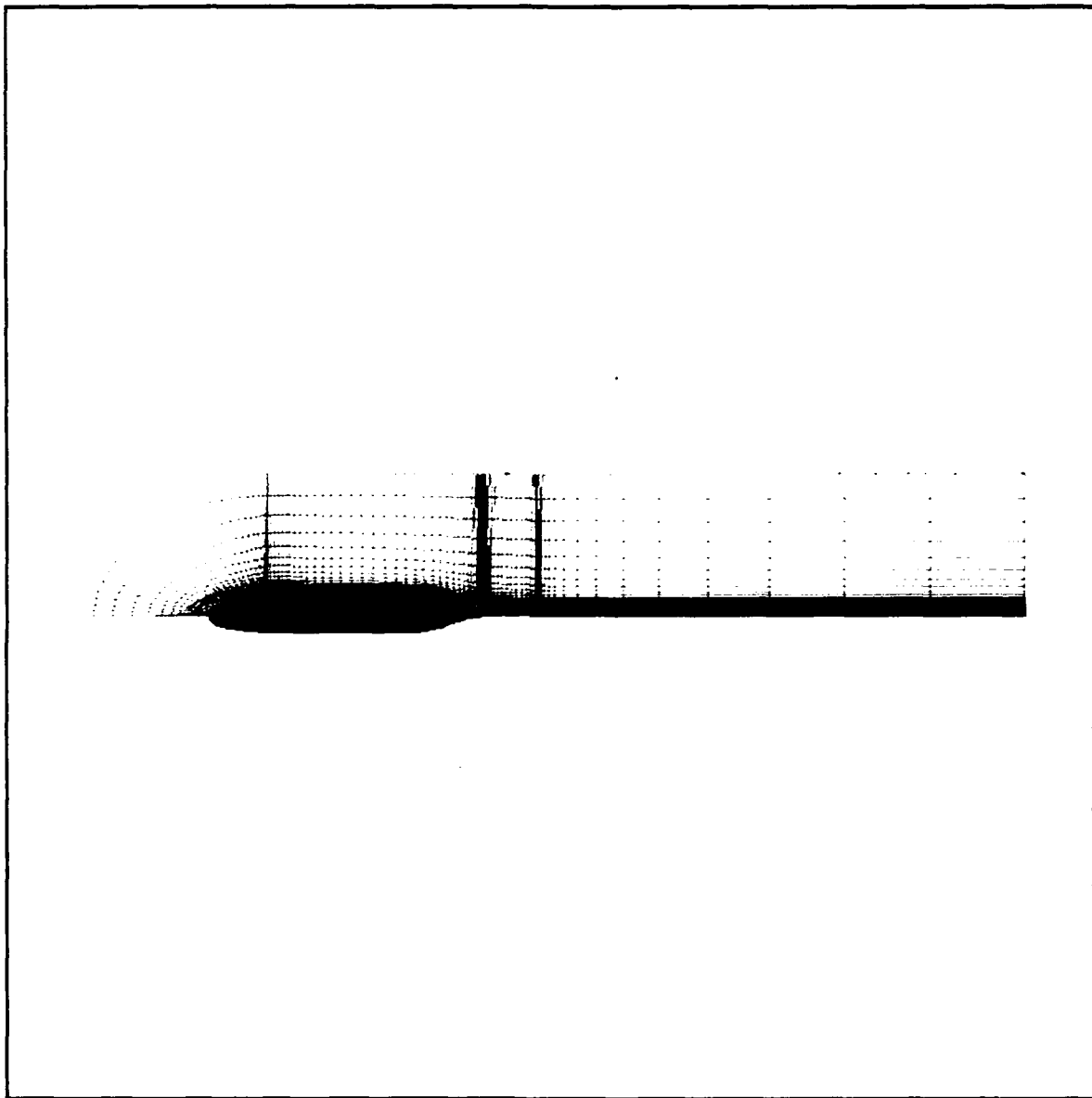


Fig. 12. Upper grid surface for body with sail.

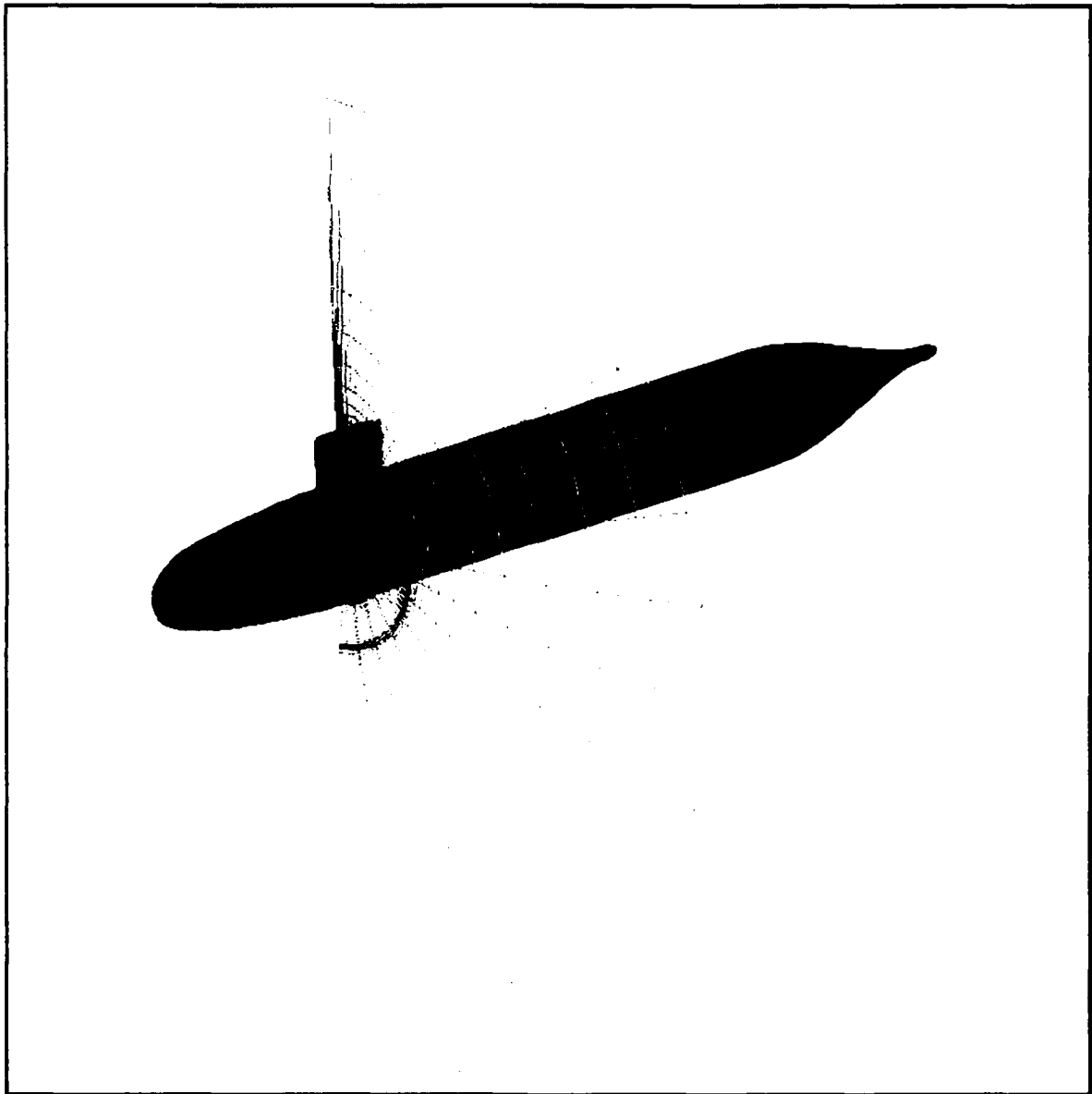


Fig. 13. Cross-sectional grid surface for body with sail.

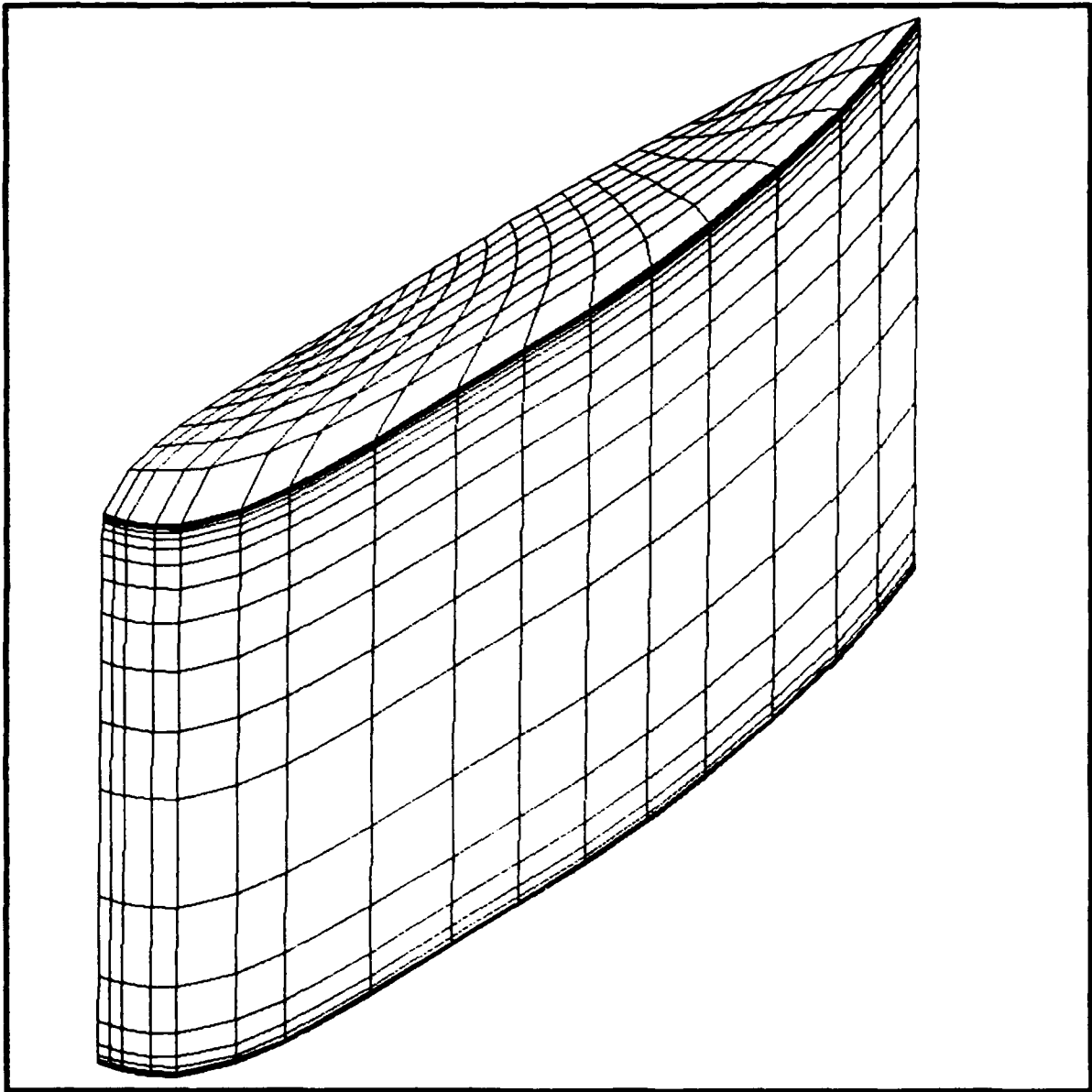


Fig. 14. Surface grid on sail with cap.

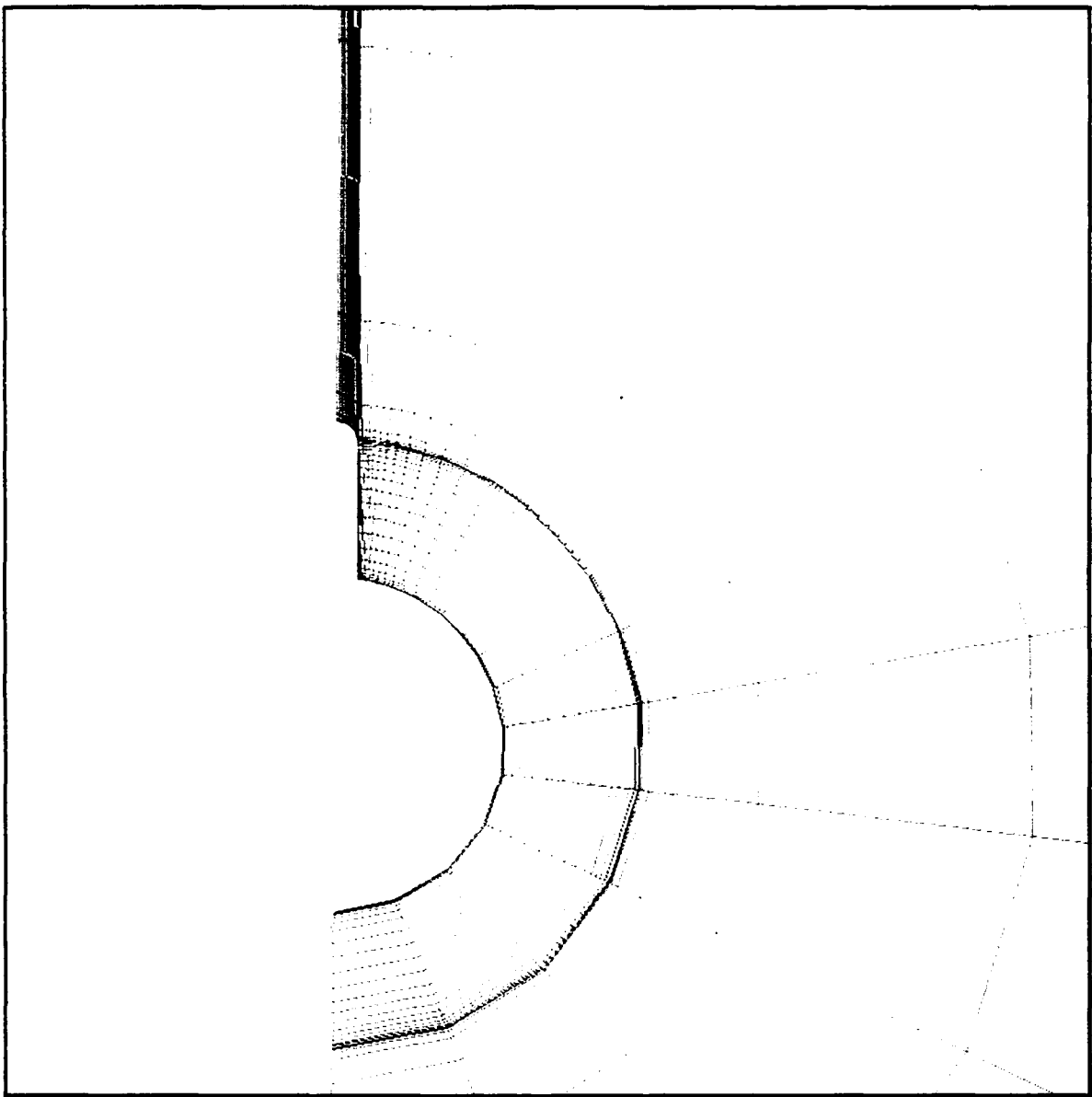


Fig. 15. Cross-sectional grid surface for body with sail.

PARTICLE TRACES
 DAPPAZ WITH SAIL
 DAVID TAYLOR RESEARCH CENTER

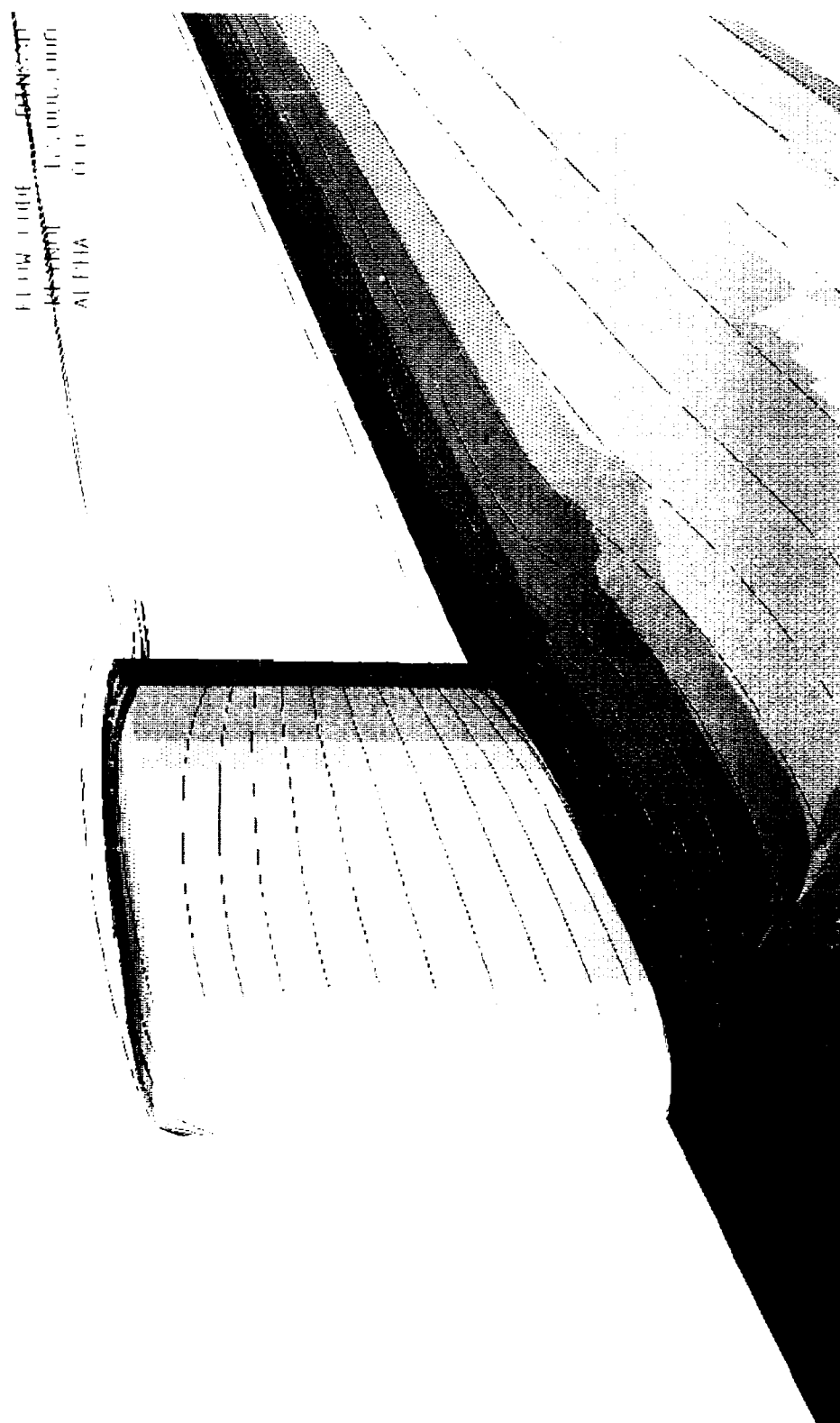


Fig. 16. Particle traces computed with coarse grid for body with sail.

PARTICLE TRACES
 DAPPED WITH SAIL
 DAVID TAYLOR RESEARCH CENTER

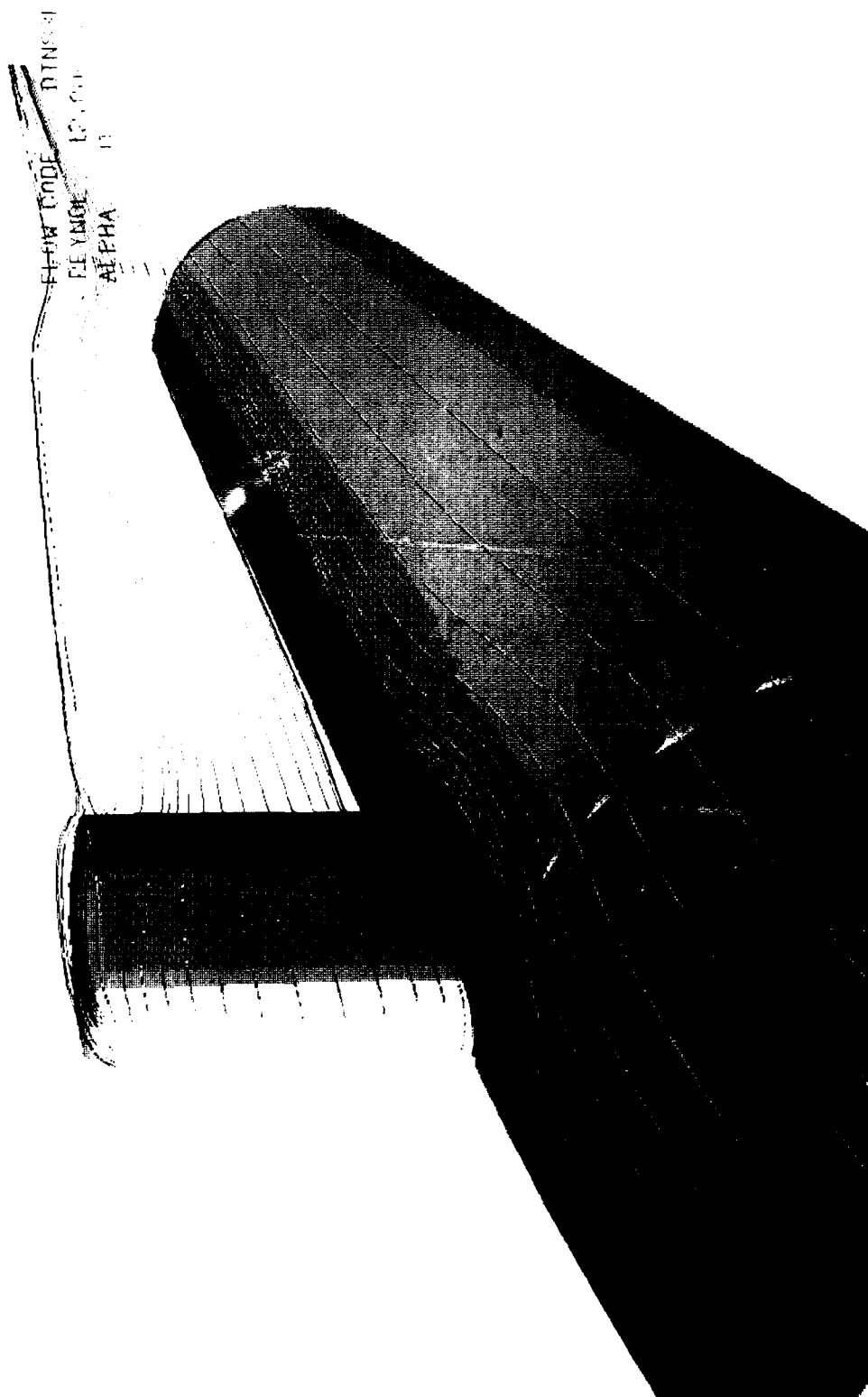


Fig. 17. Particle traces computed with refined grid for body with sail.

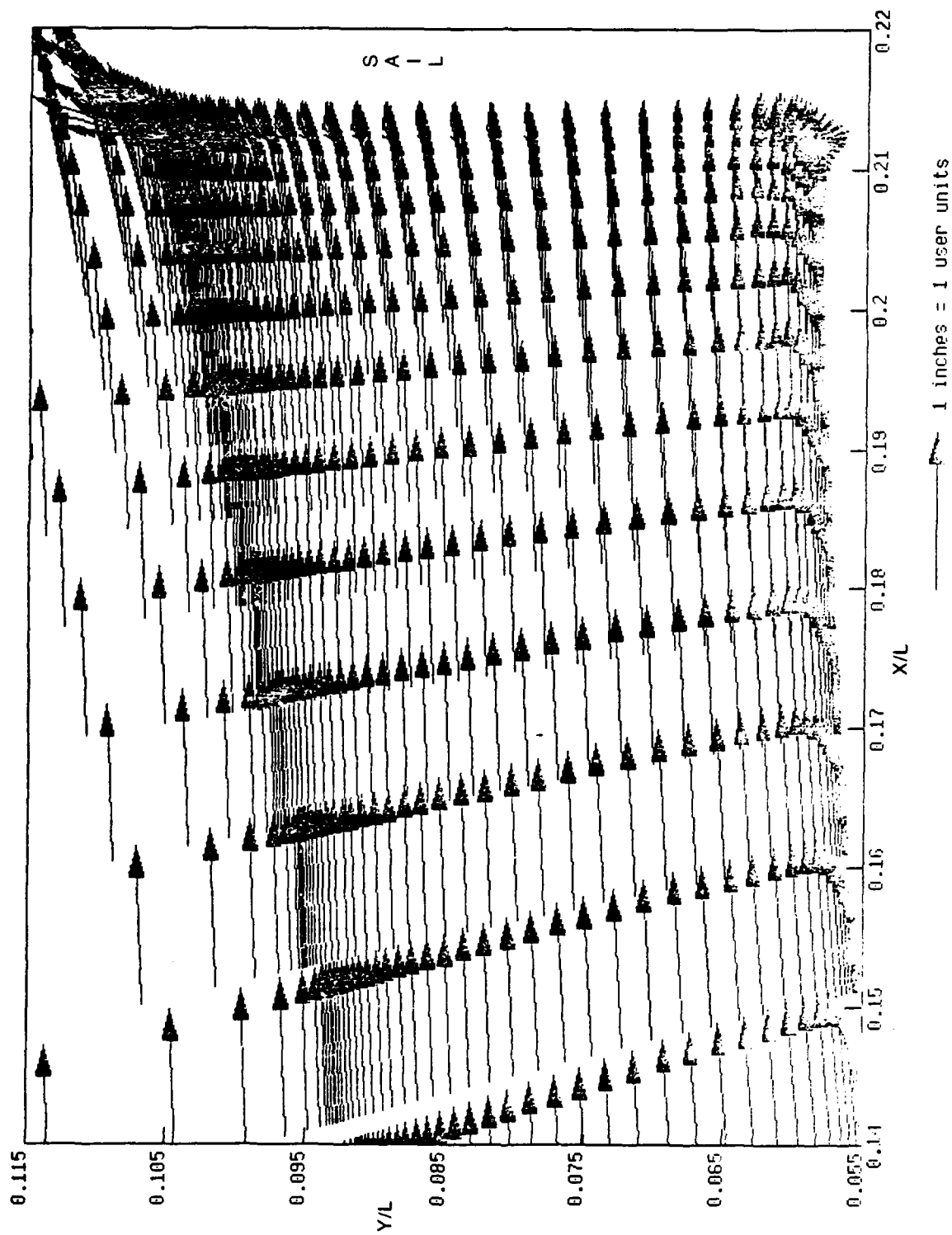


Fig. 18. Velocity vectors in the top center plane in front of the sail.

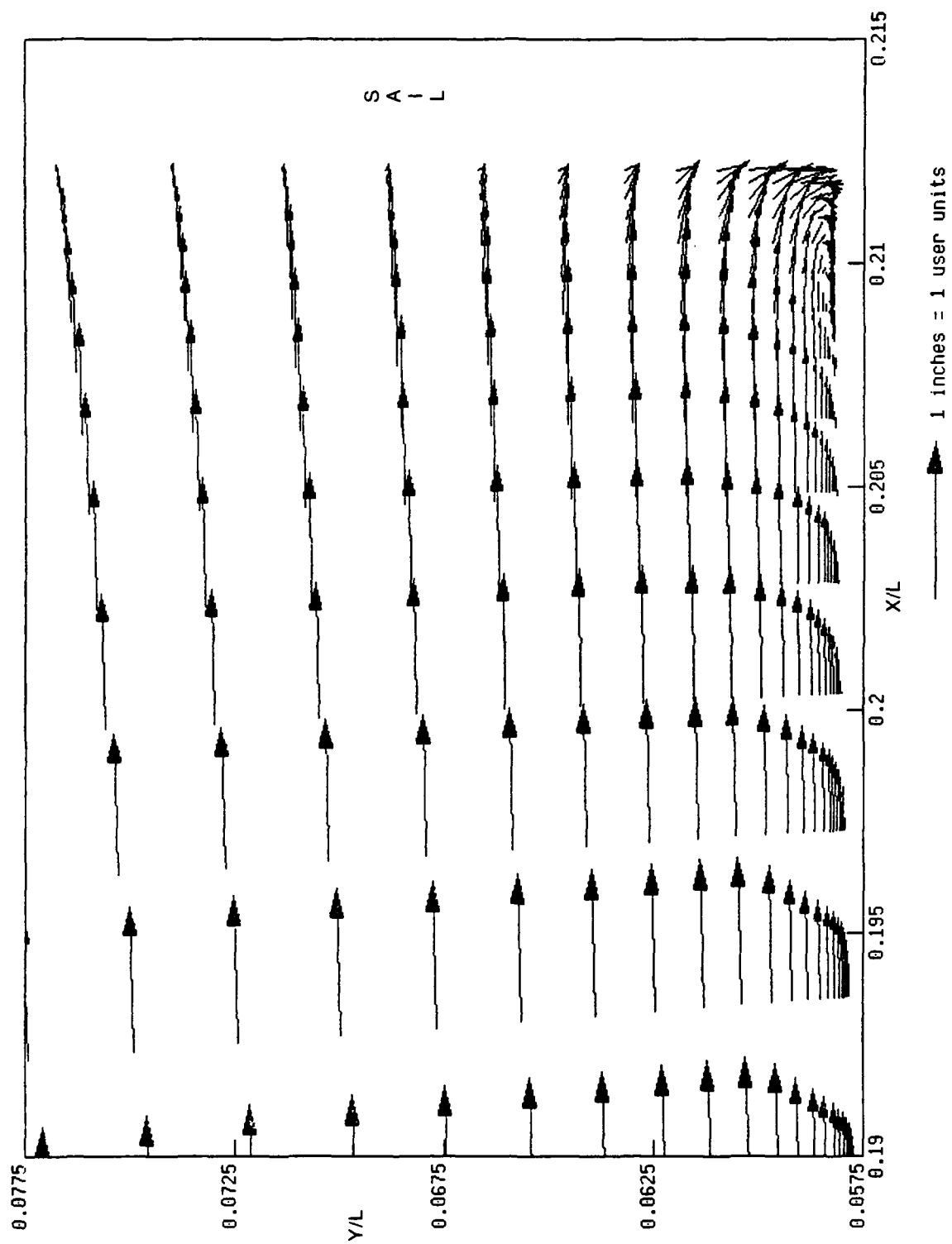


Fig. 19. Detail of corner flow in the top center plane in front of the sail.

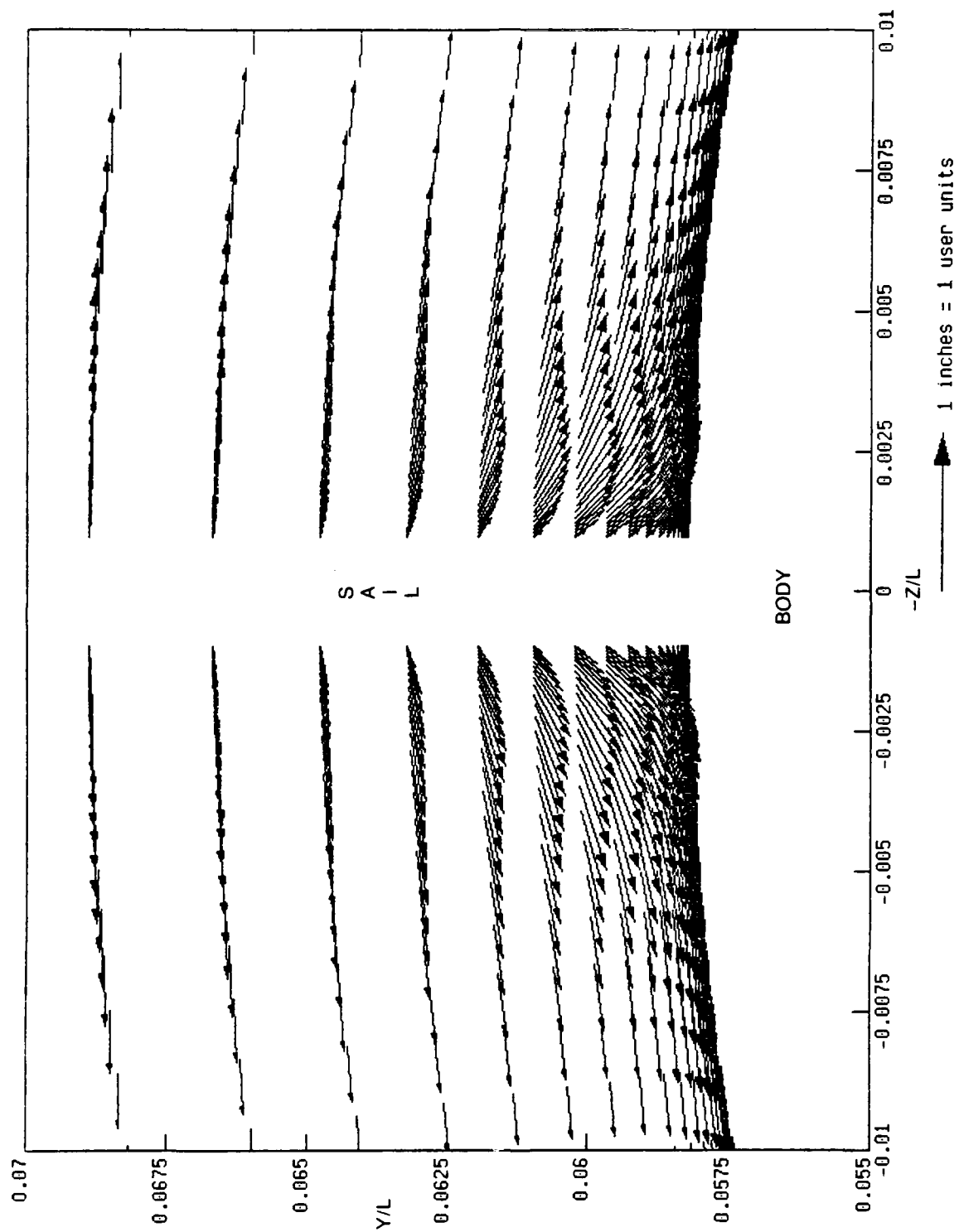


Fig. 20. Crossflow velocity vectors at the base of the sail immediately downstream from the leading edge.

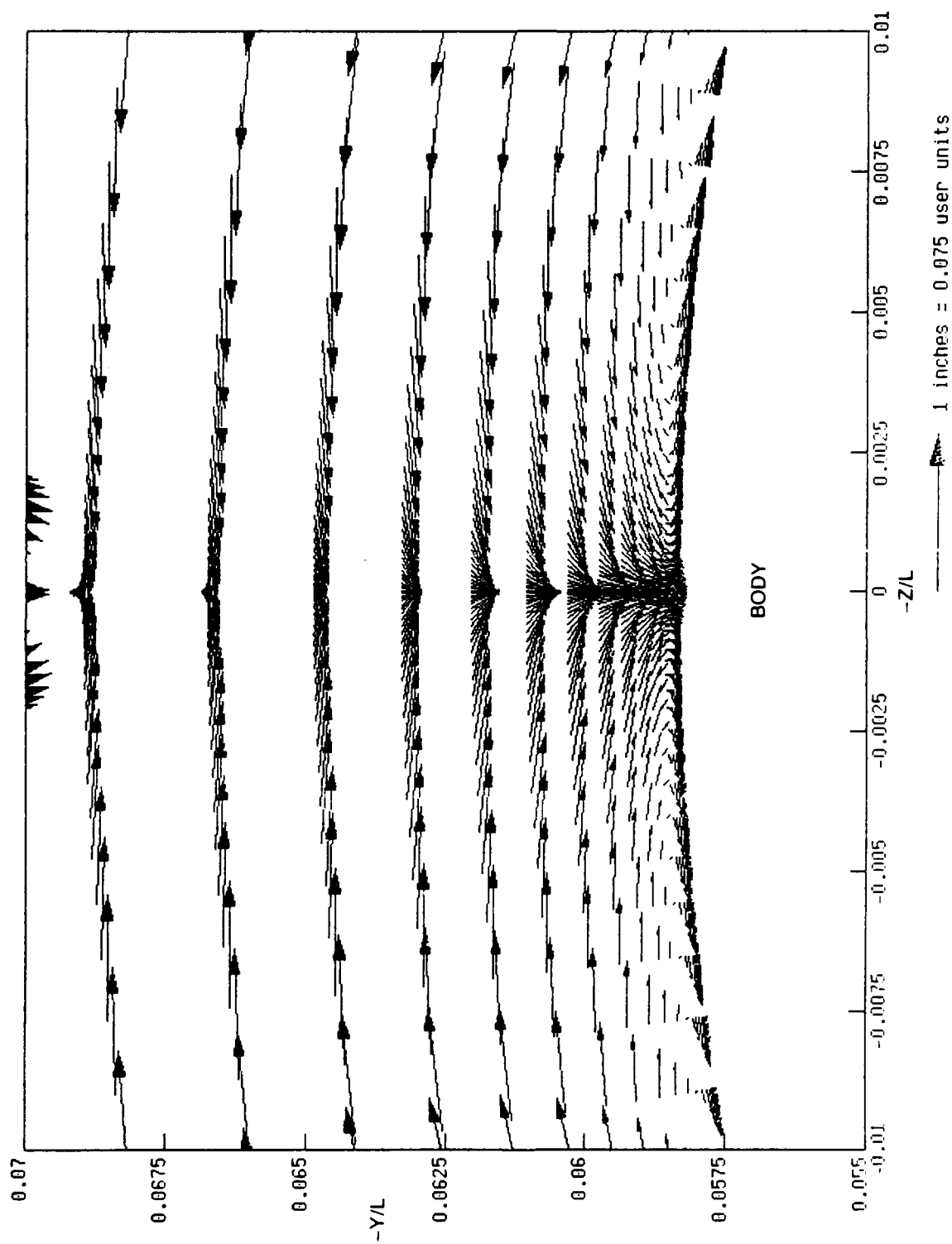


Fig. 21. Crossflow velocity vectors at the base of the sail immediately downstream from the trailing edge.

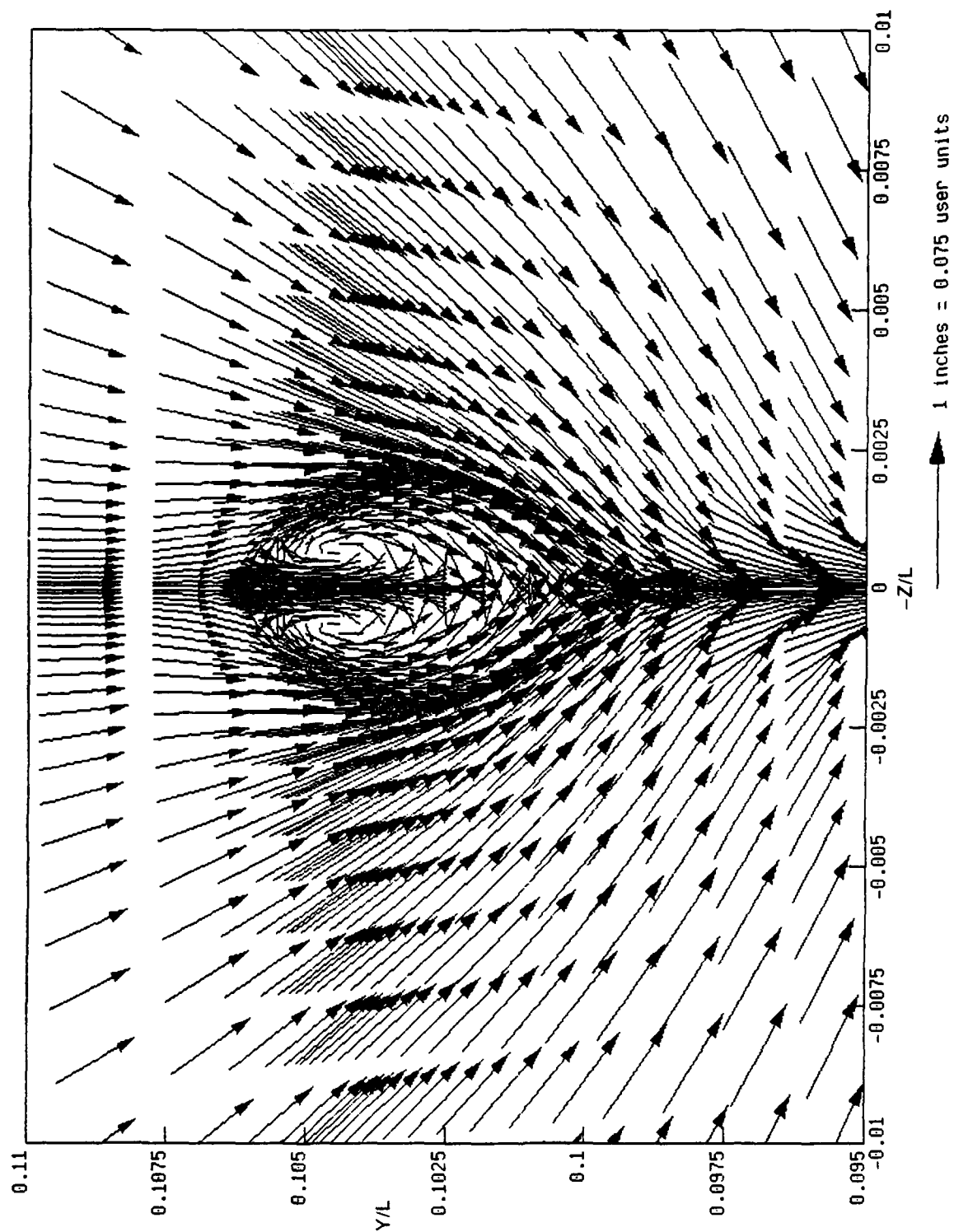


Fig. 22. Crossflow velocity vectors at the tip of the sail immediately downstream from the trailing edge.

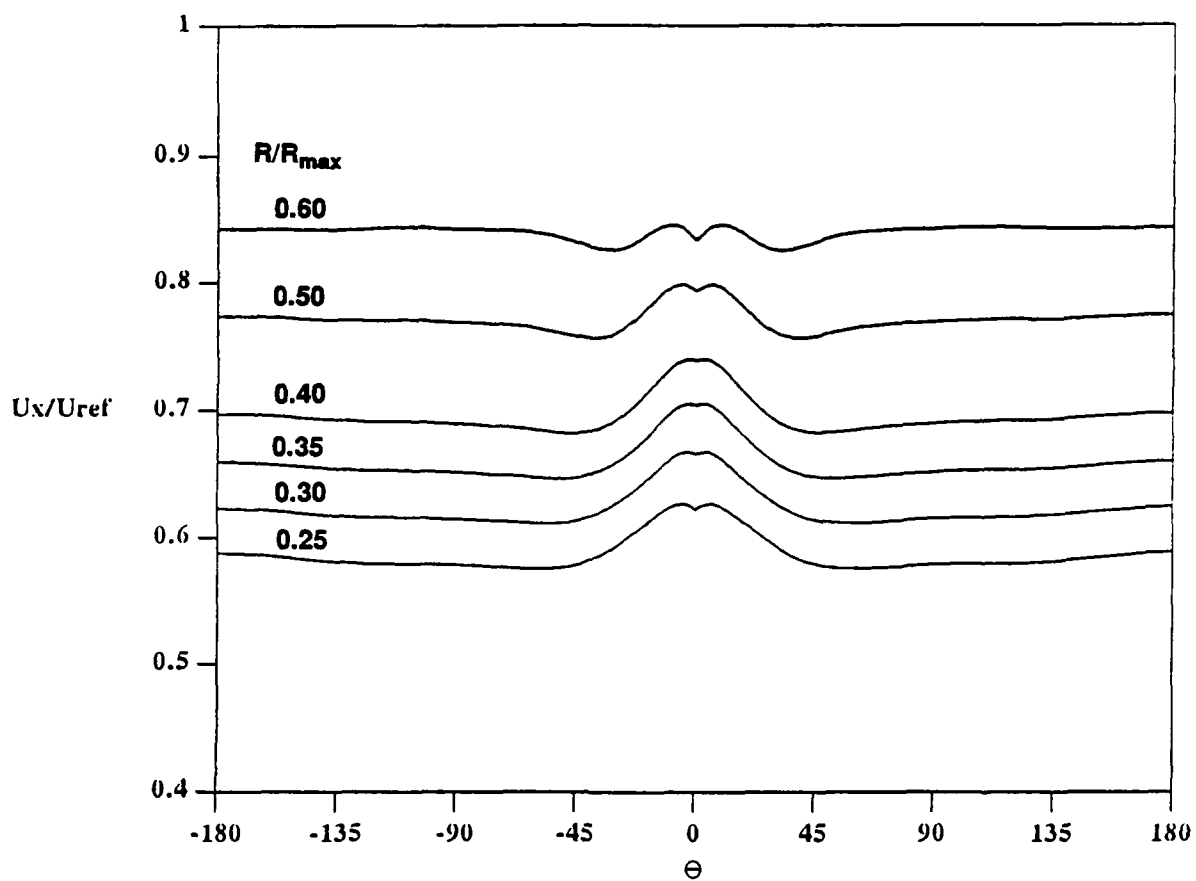


Fig. 23. Streamwise velocity profiles for body with sail at $X/L = 0.978$ and $R/R_{max} = 0.25, 0.30, 0.35, 0.40, 0.50$, and 0.60 .

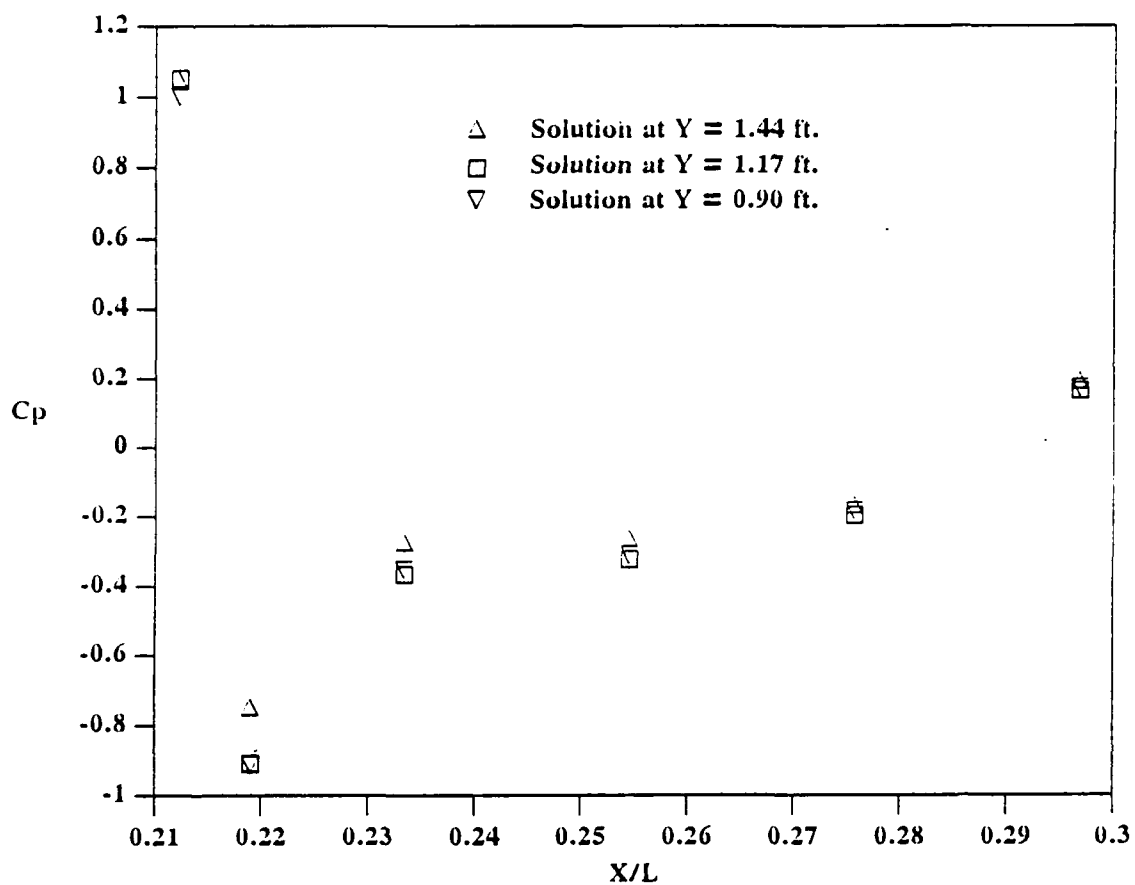


Fig. 24. Pressure coefficient on the sail at three heights.

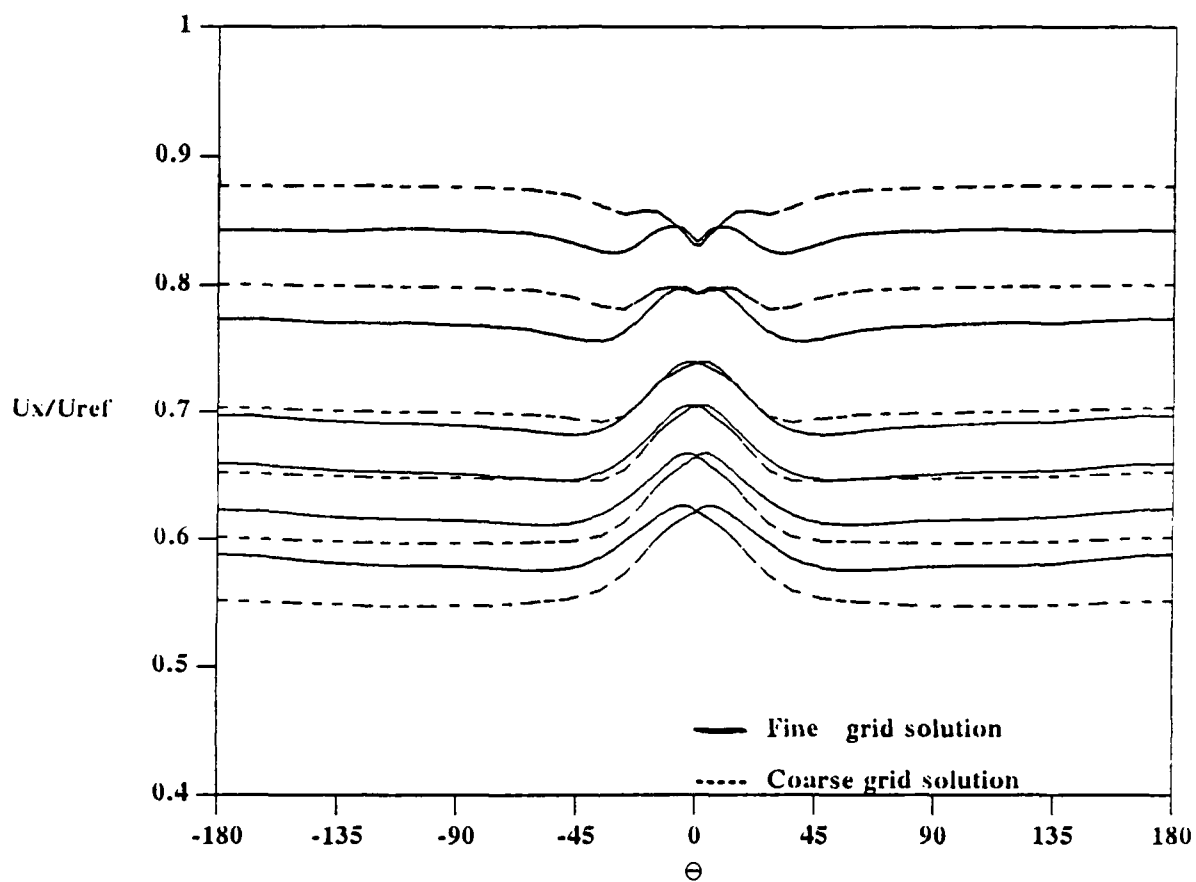


Fig. 25. Streamwise velocity profiles for body with sail at $X/L = 0.978$ computed with coarse and fine grids.

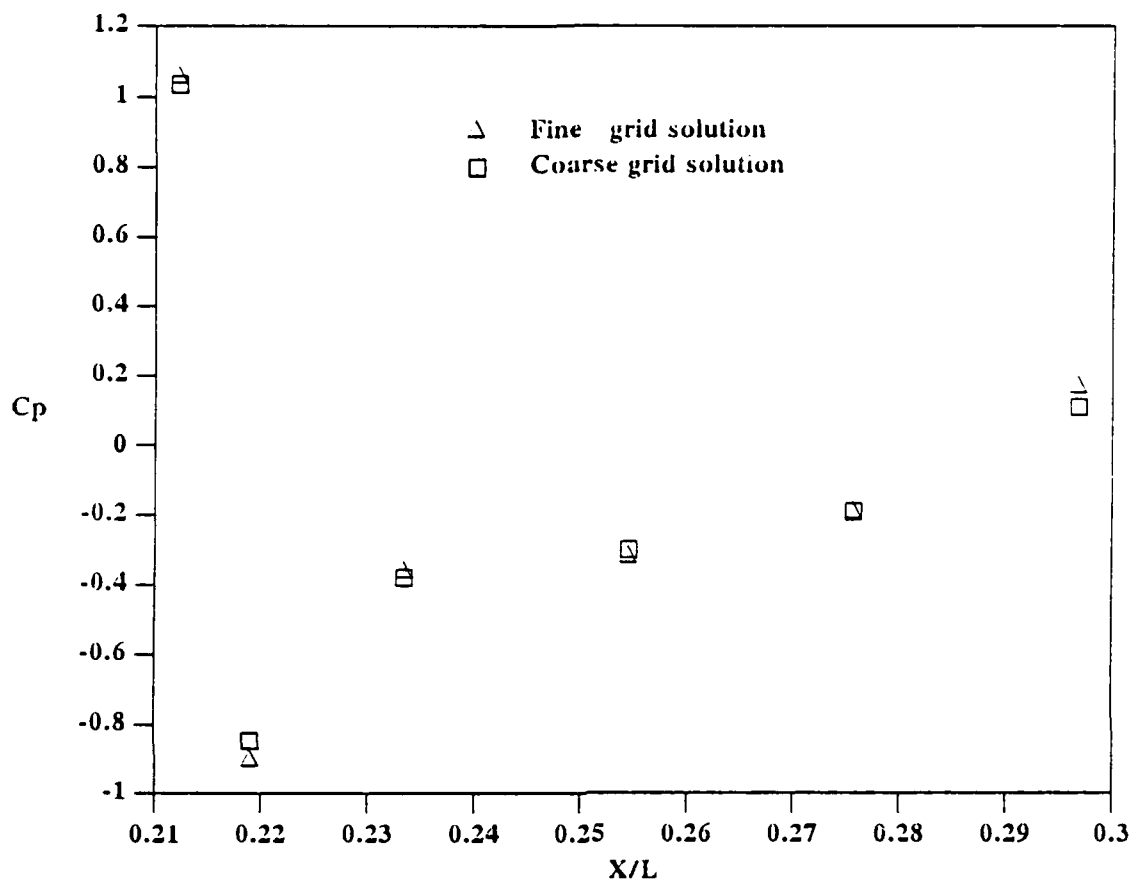


Fig. 26. Pressure coefficients on the sail at $Y = 1.17$ feet computed with coarse and fine grids.

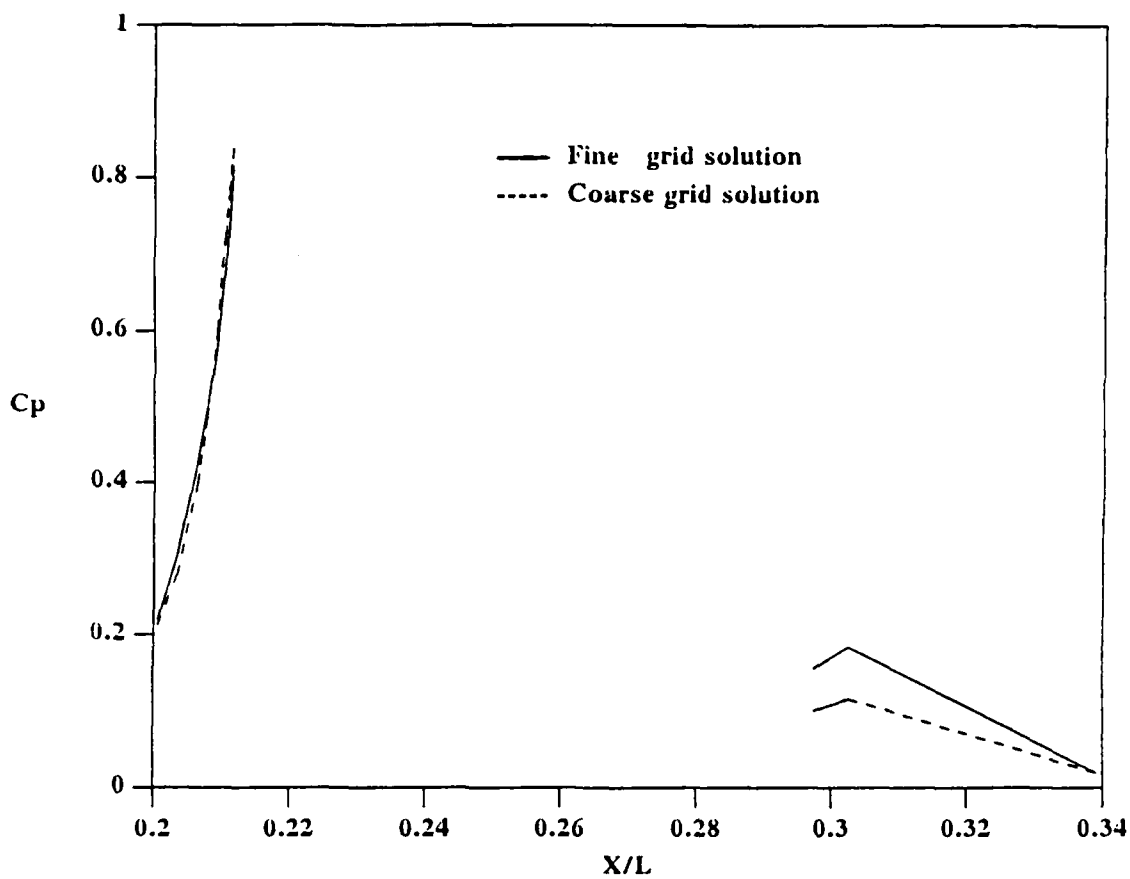


Fig. 27. Pressure coefficients on the hull surface centerline upstream and downstream of the sail computed with coarse and fine grids.

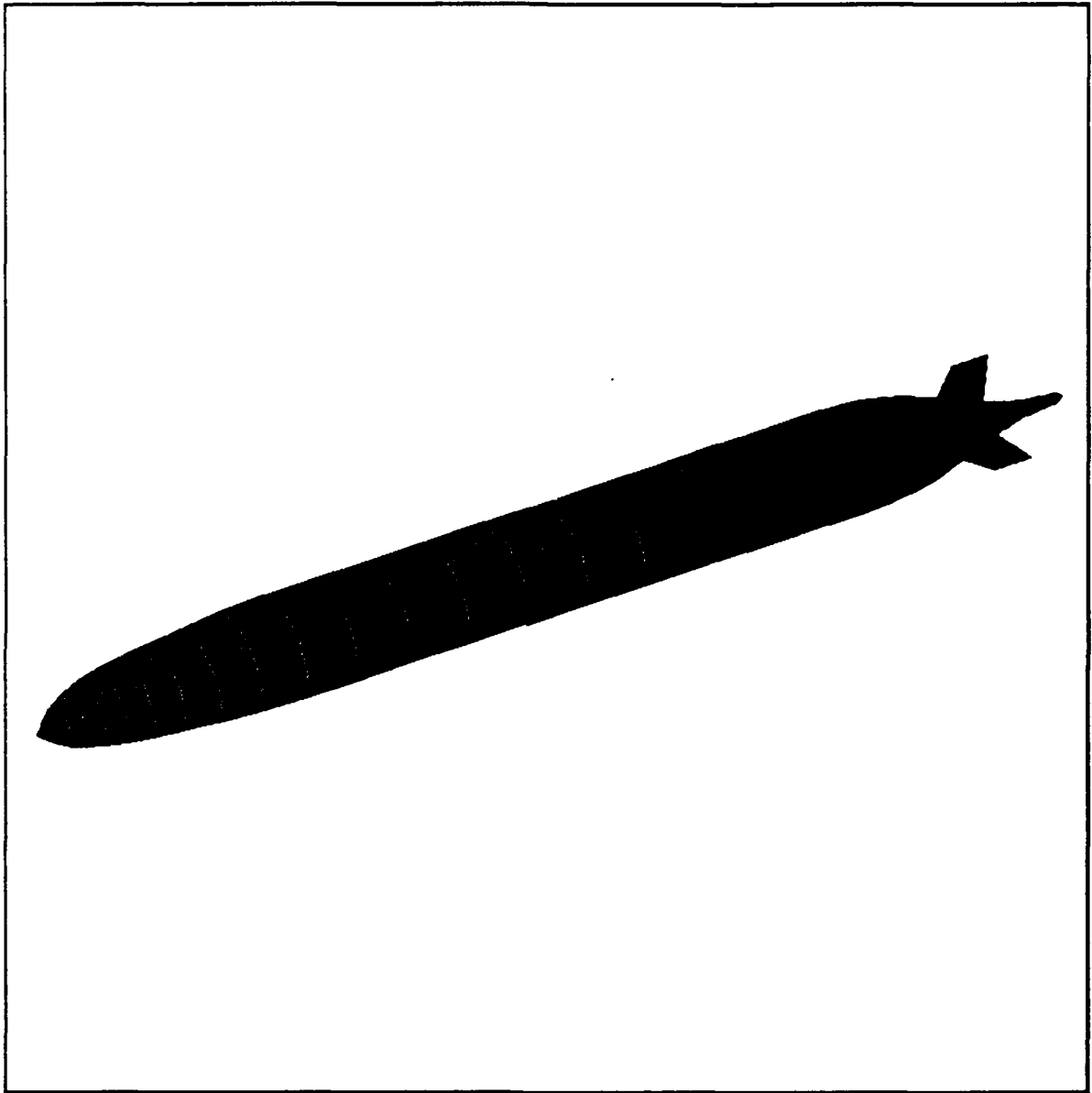


Fig. 28. Body with stern appendages, configuration 3.

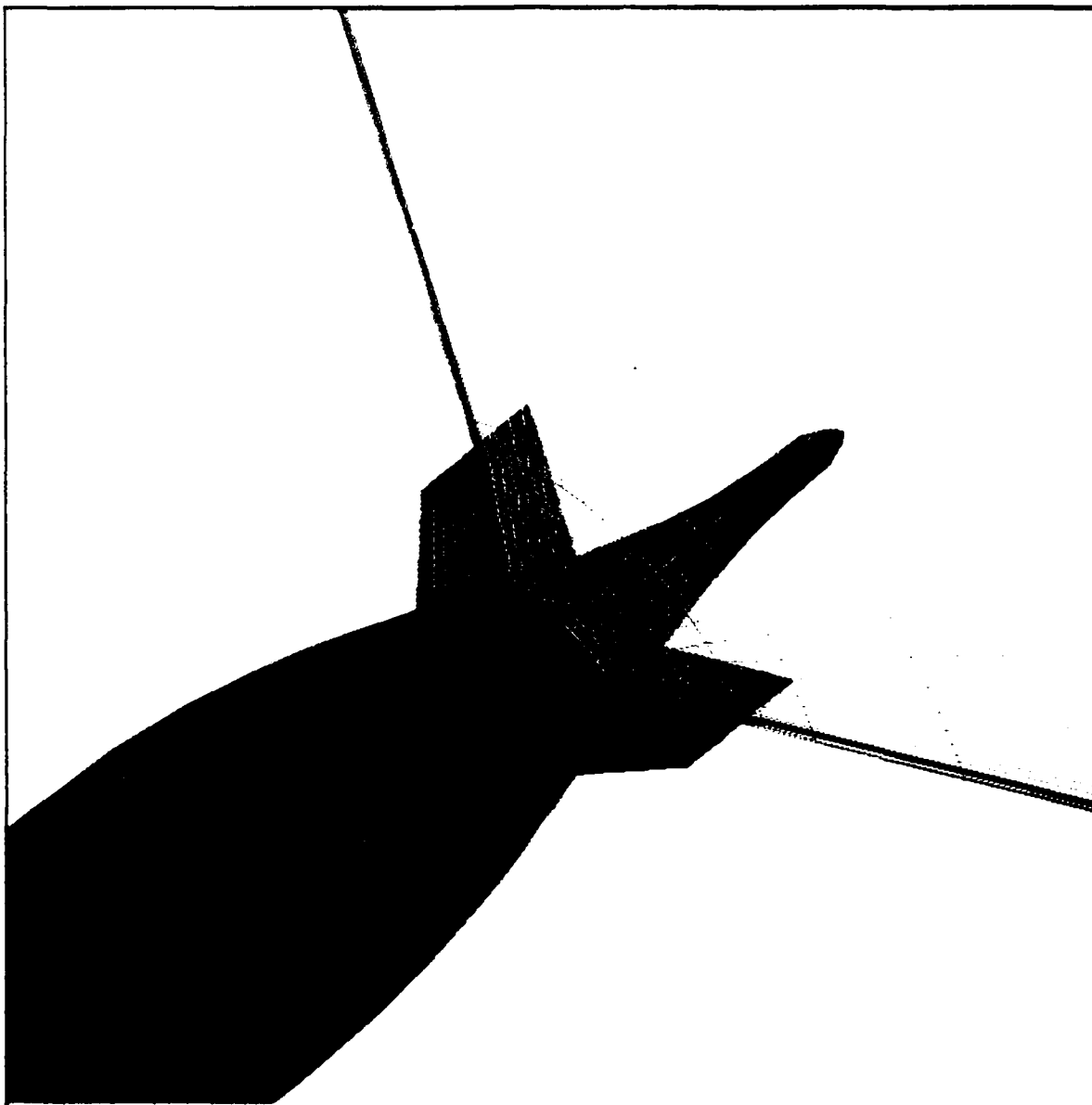


Fig. 29. Cross-sectional grid surface for body with stern appendages.

PARTICLE TRACES
 DARPA2 WITH STERN PLANES
 DAVID TAYLOR RESEARCH CENTER

FLOW CODE 0THSRD
 REYNOL 12,000,000
 ALPHA 0.0

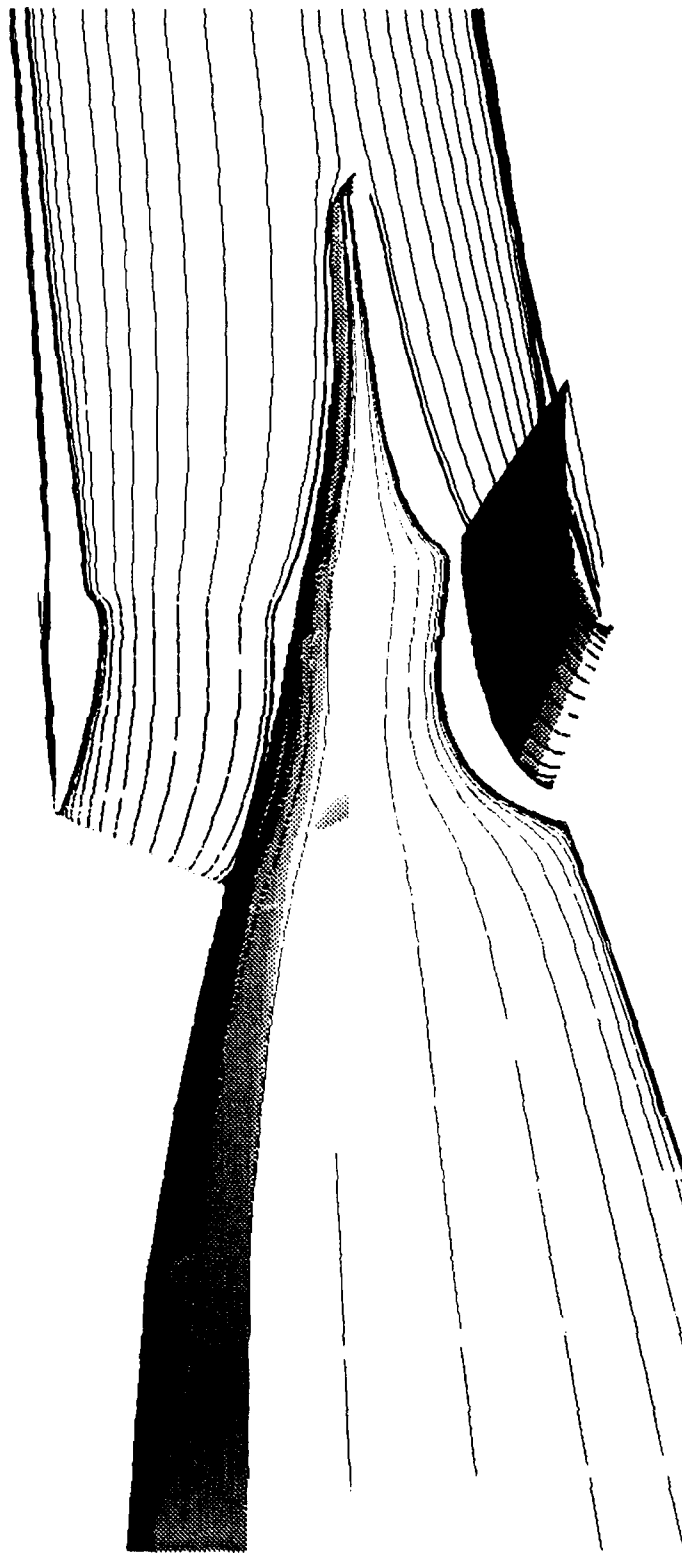


Fig. 30. Particle traces for body with stern appendages.

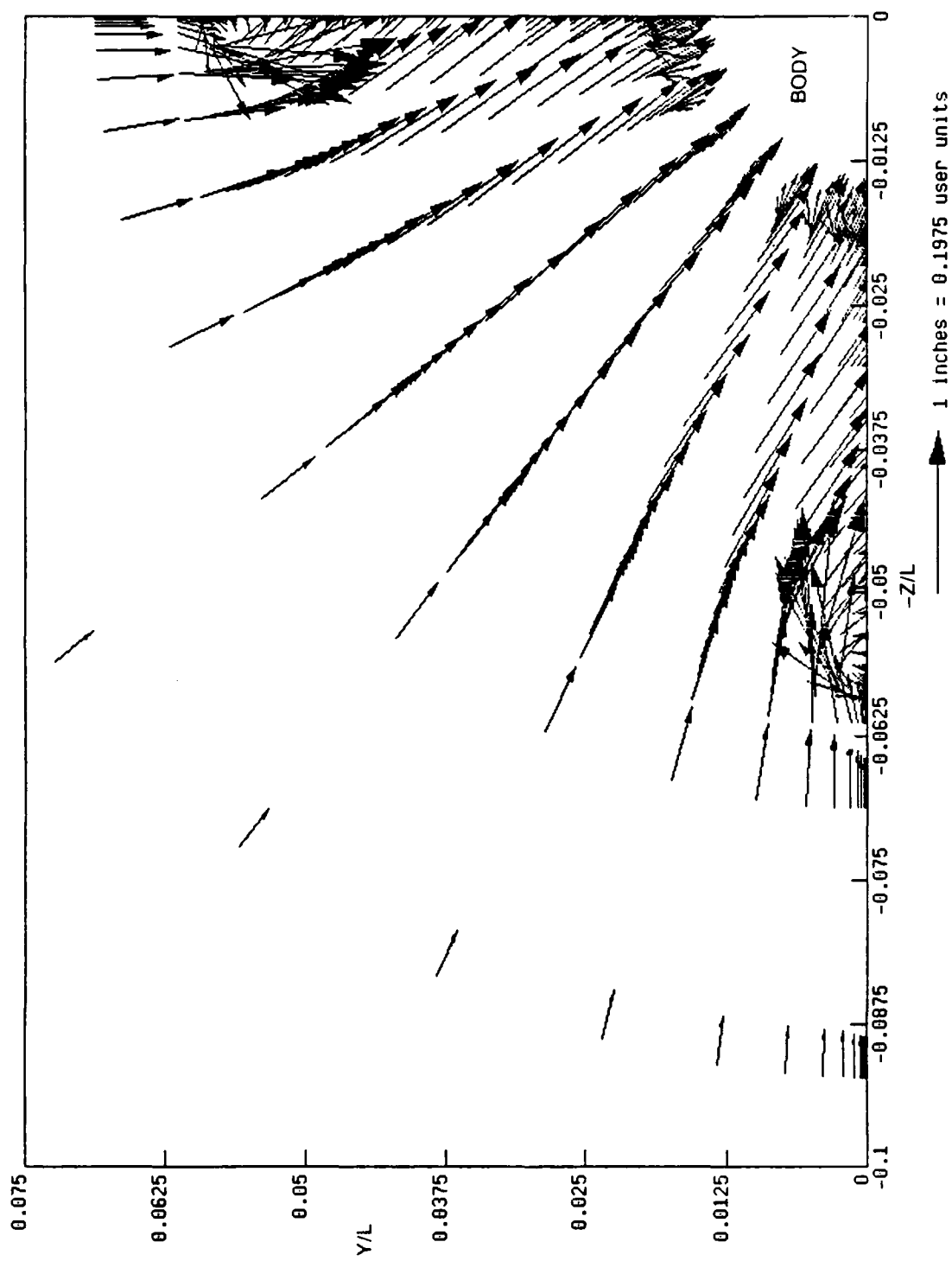


Fig. 31. Crossflow velocity vectors at stern plane trailing edges.

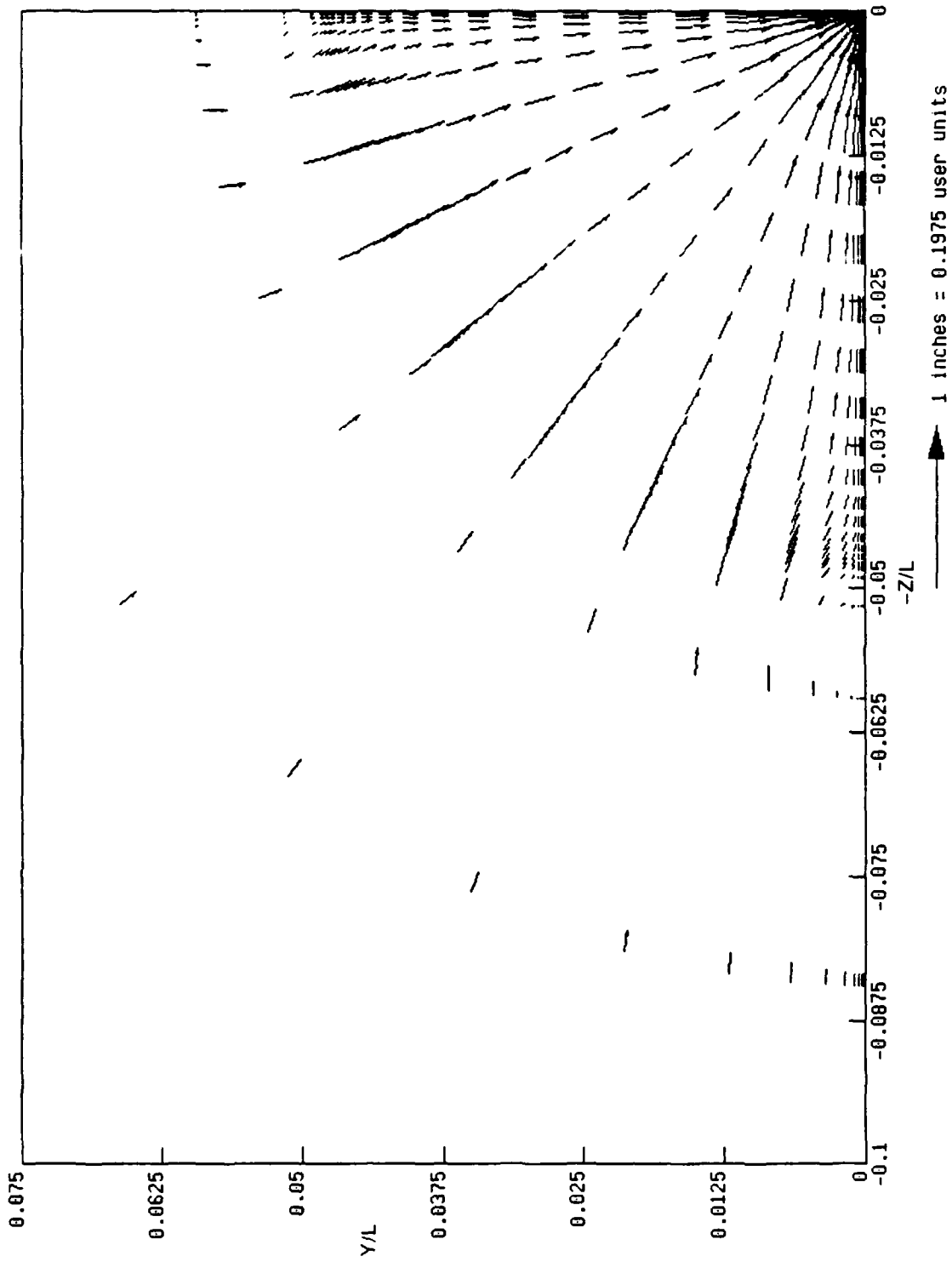


Fig. 32. Crossflow velocity vectors at $X/L = 1.0$.

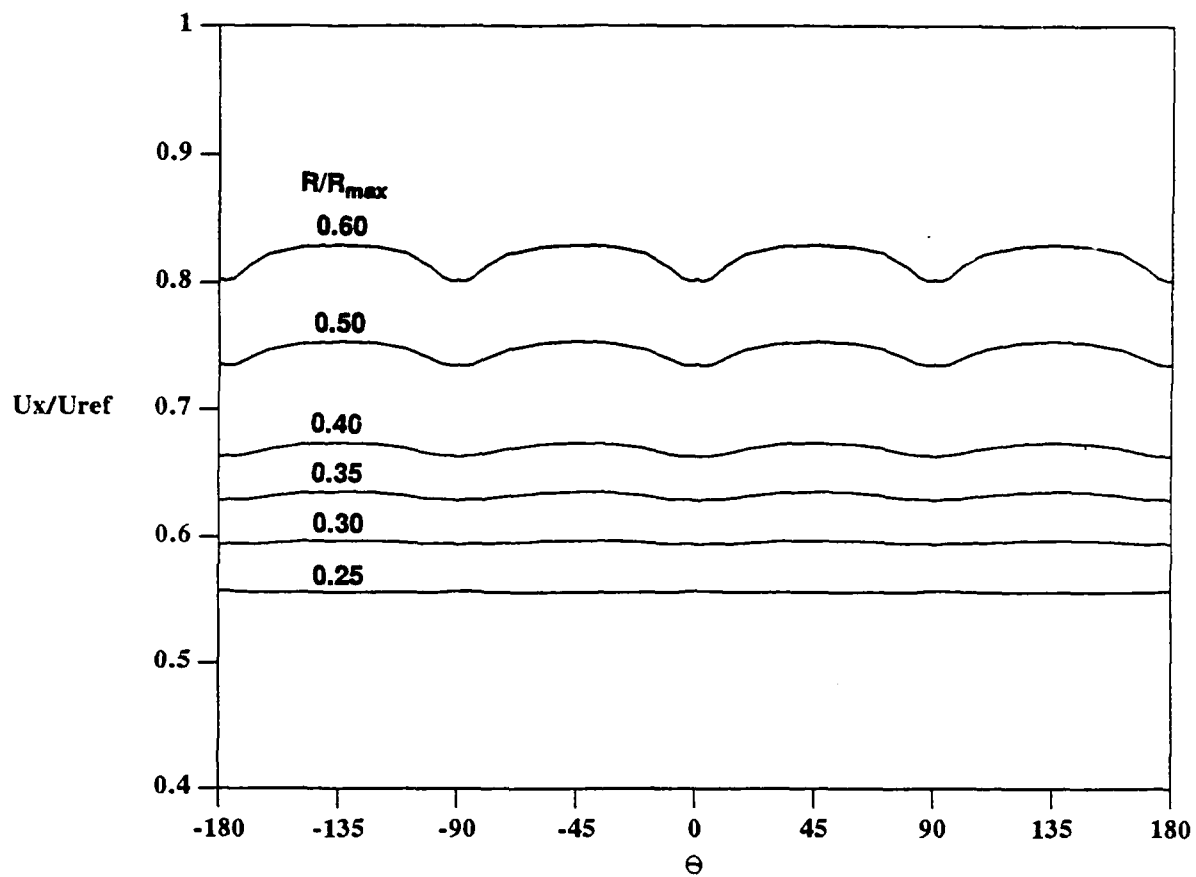


Fig. 33. Streamwise velocity profiles for body with stern appendages at $X/L = 0.978$ and $R/R_{max} = 0.25, 0.30, 0.35, 0.40, 0.50$, and 0.60 .

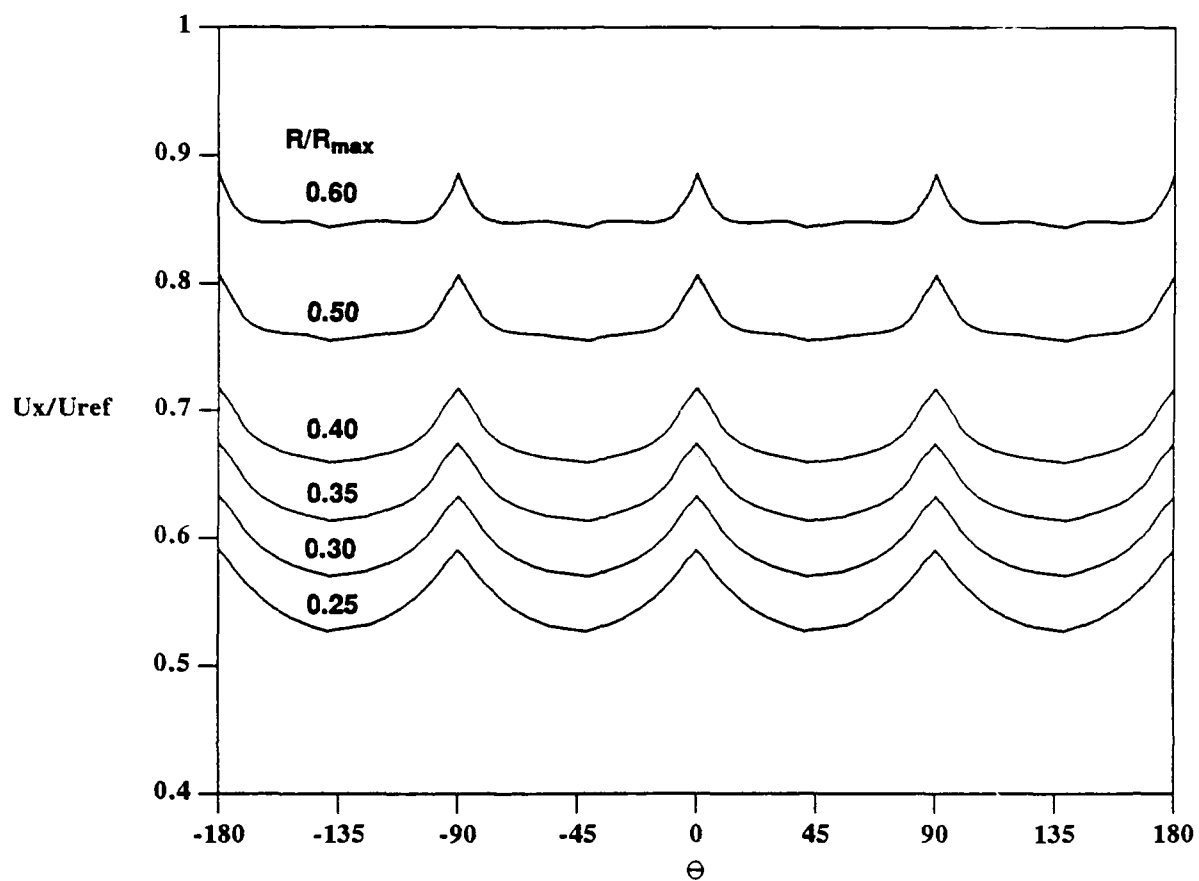


Fig. 34. Streamwise velocity profiles for body with stem appendages at $X/L = 0.978$ obtained with refined grid.

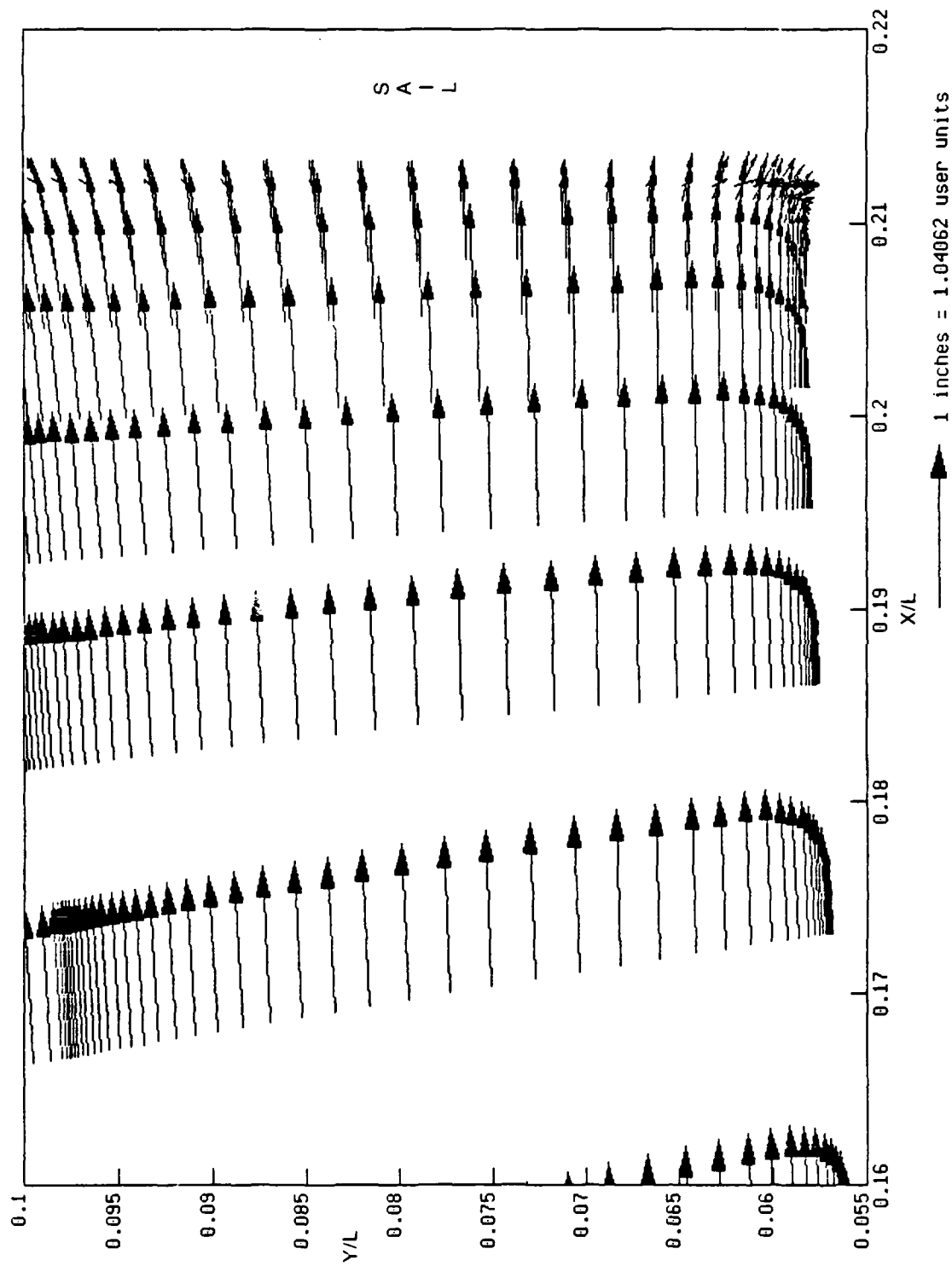


Fig. 35. Velocity vectors in the top center plane in front of the sail for an angle of attack of two degrees.

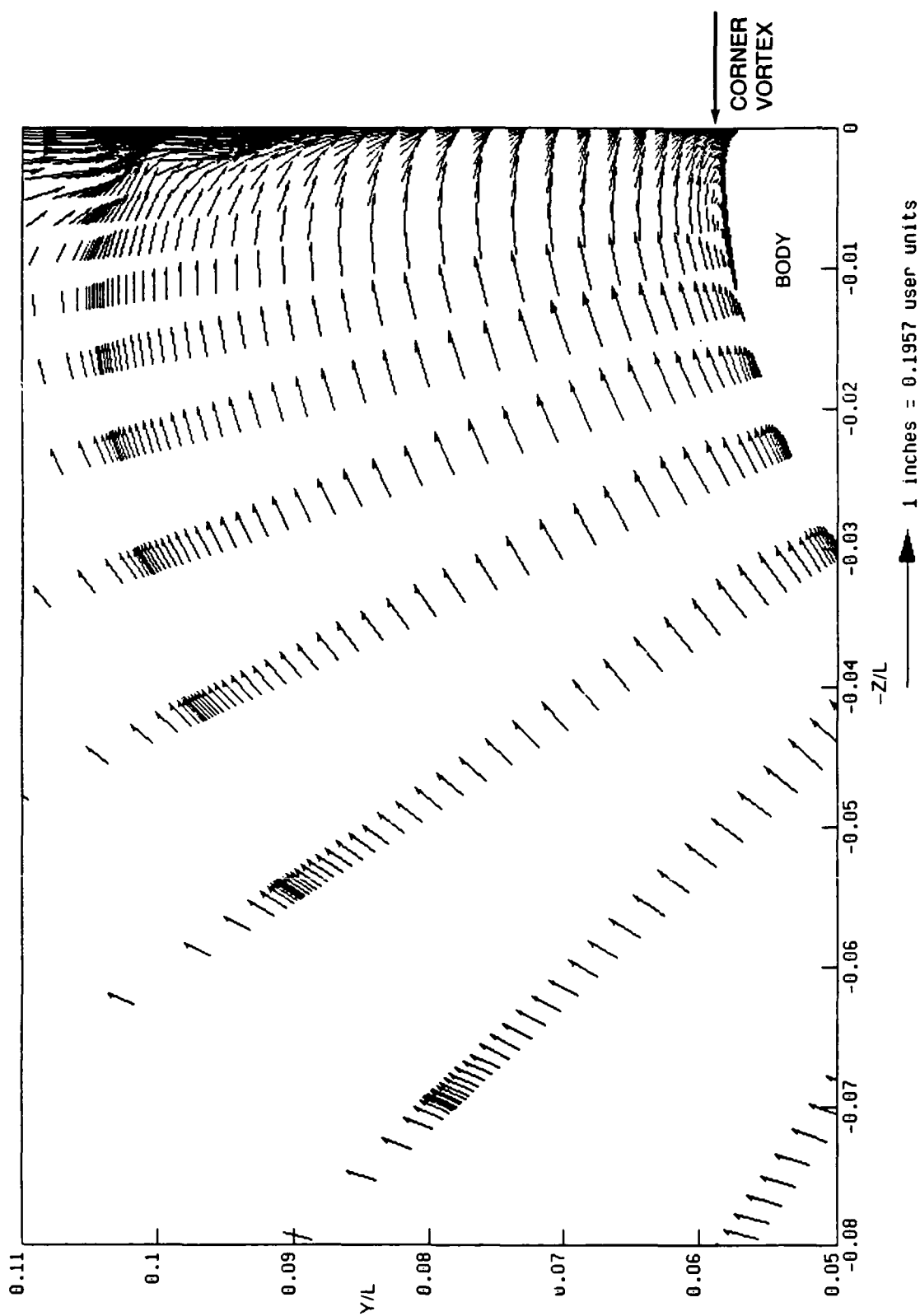


Fig. 36. Crossflow velocity vectors immediately downstream from the sail trailing edge for an angle of attack of two degrees.

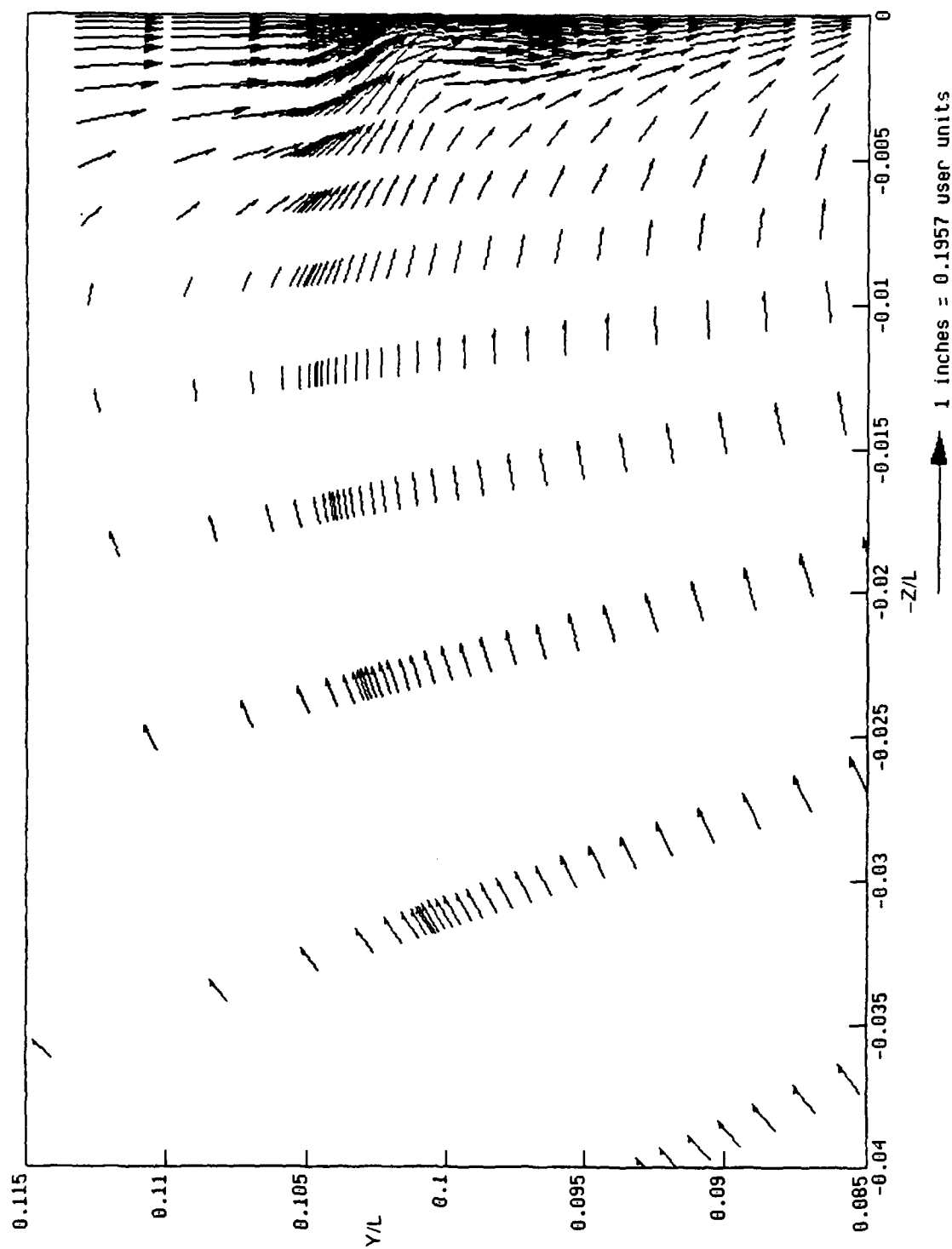


Fig. 37. Crossflow velocity vectors near the tip of the sail immediately downstream from the trailing edge for an angle of attack of two degrees.

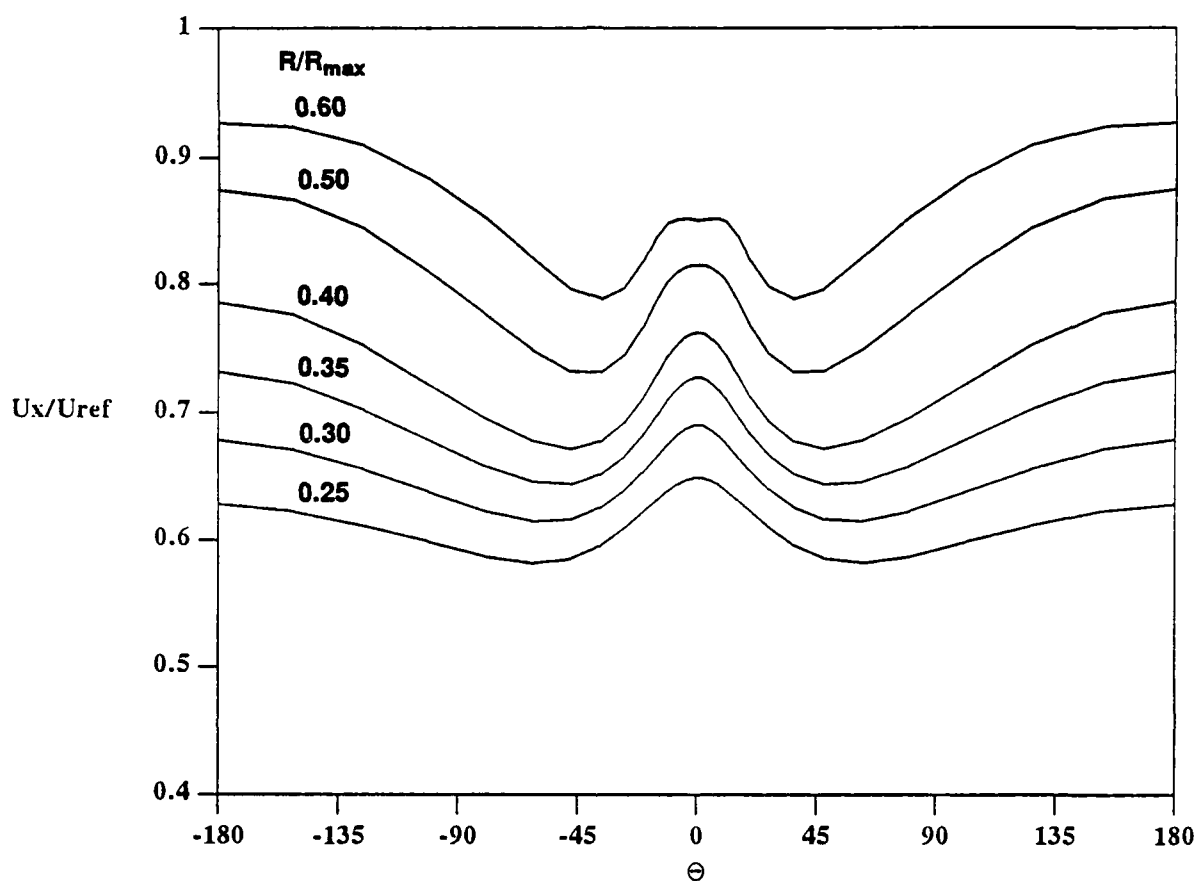


Fig. 38. Streamwise velocity profiles at $X/L = 0.978$ and $R/R_{max} = 0.25, 0.30, 0.35, 0.40, 0.50$, and 0.60 for body with sail at an angle of attack of two degrees.

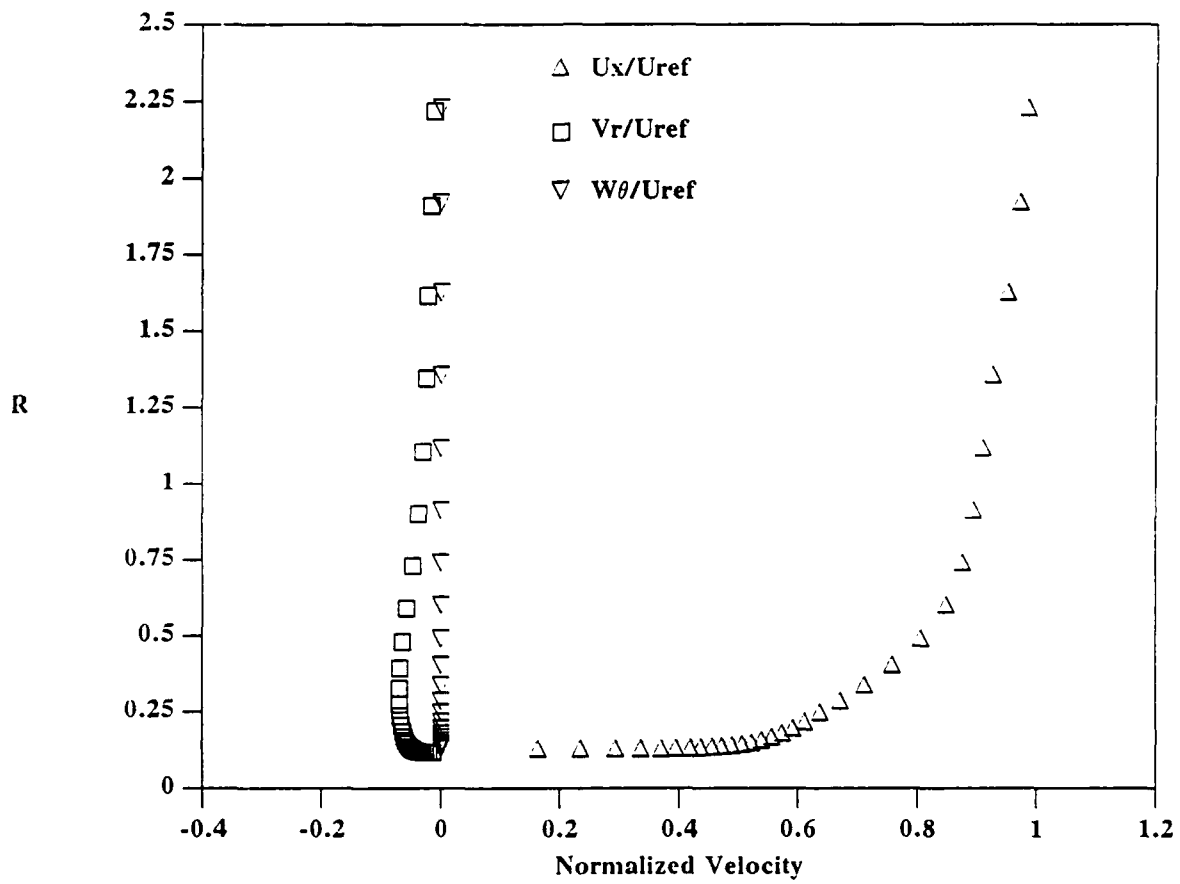


Fig. 39. Mean velocity profiles in the top center plane at $X/L = 0.978$ for body with sail at an angle of attack of two degrees.

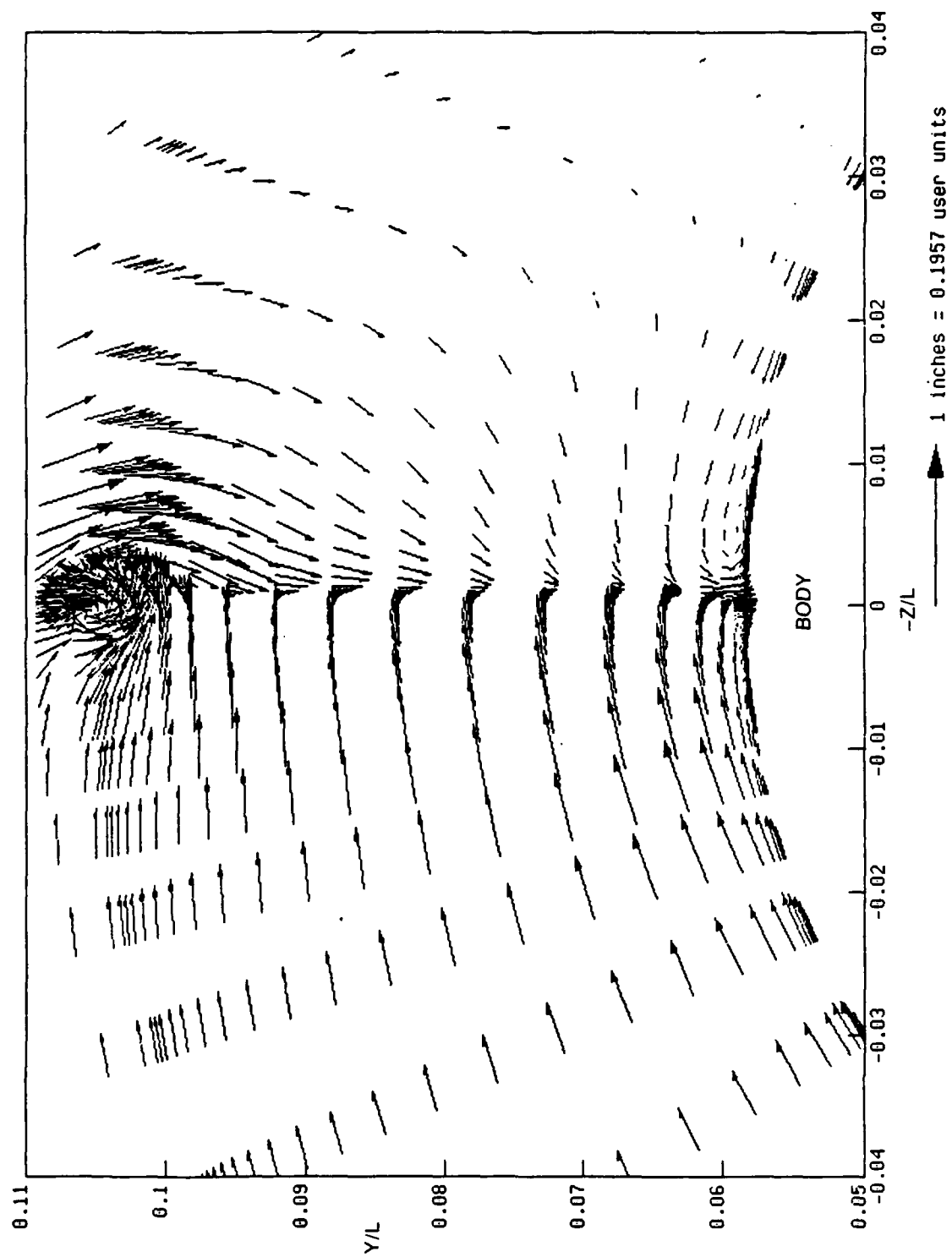


Fig. 40. Crossflow velocity vectors at the sail trailing edge for an angle of yaw of two degrees.

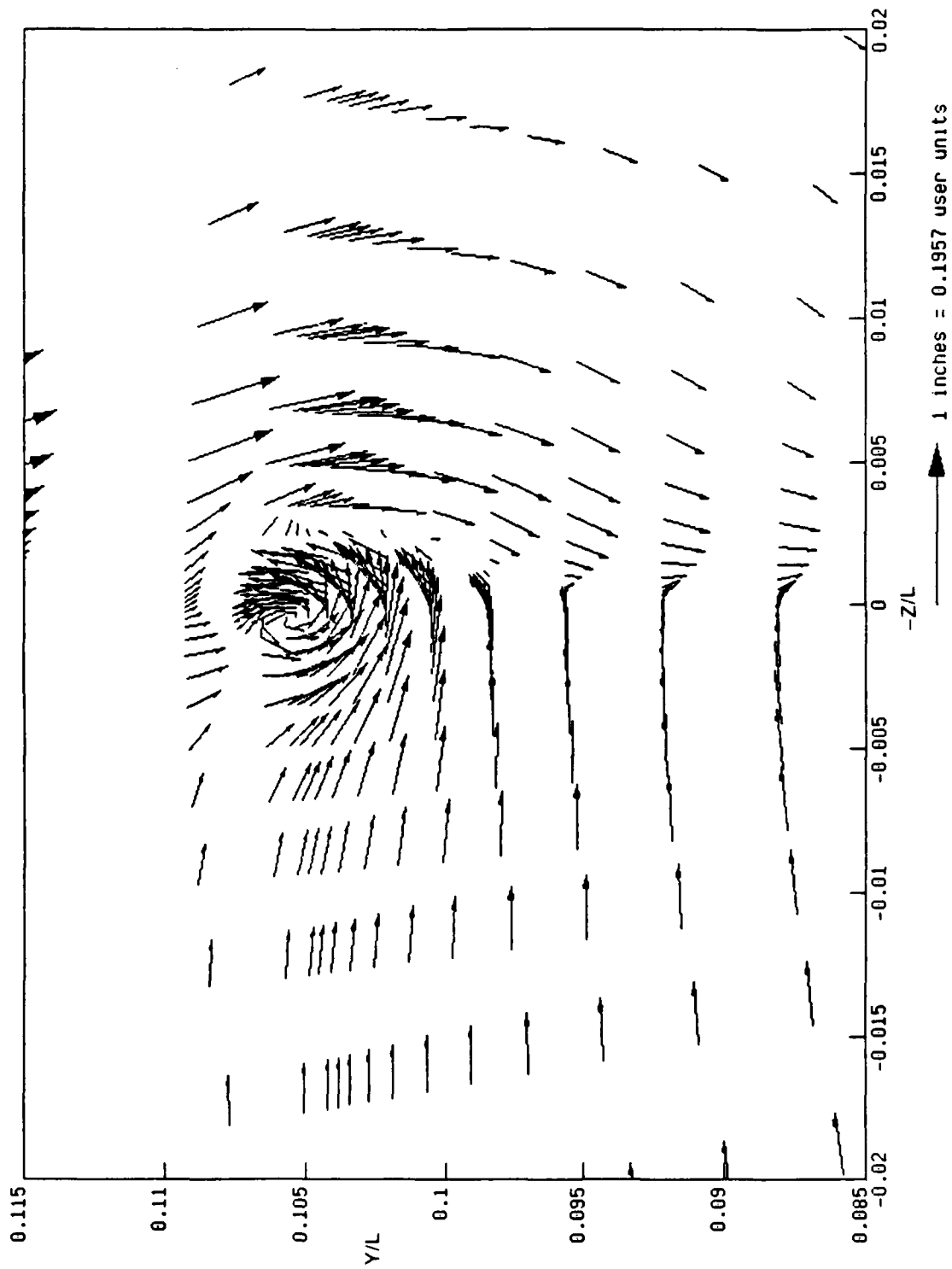


Fig. 41. Detail of the crossflow near the tip of the sail at the trailing edge for an angle of yaw of two degrees.

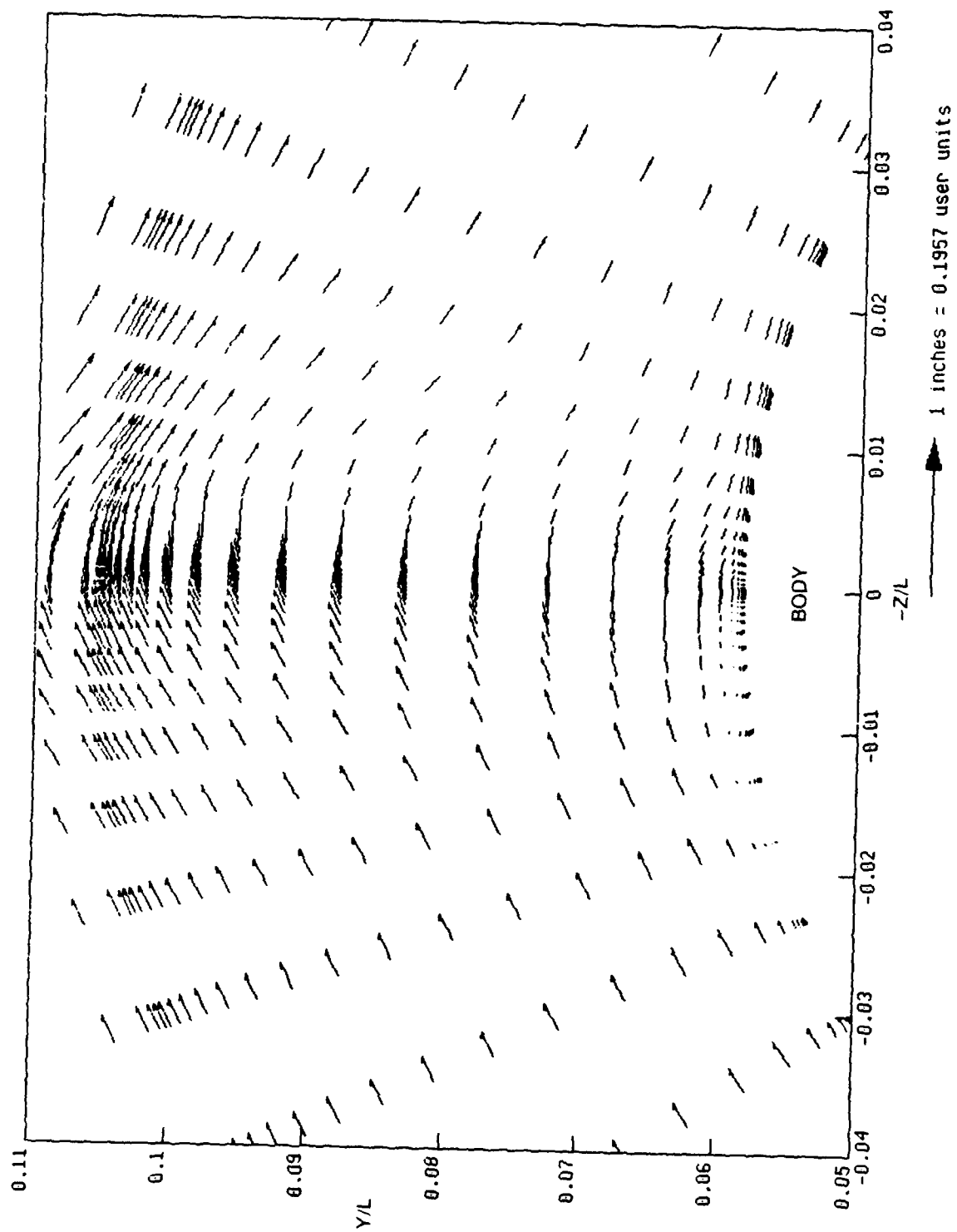


Fig. 42. Crossflow velocity vectors downstream from the sail for an angle of yaw of two degrees.

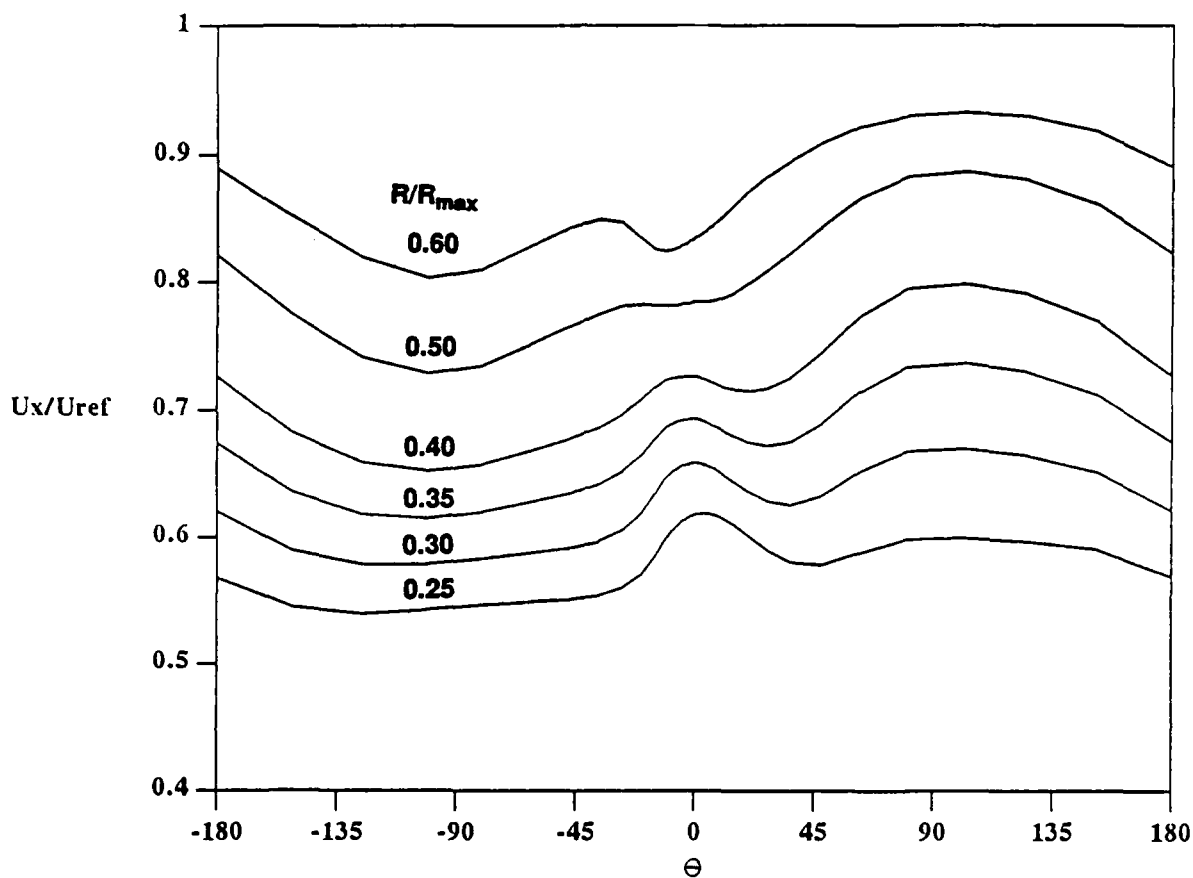


Fig. 43. Streamwise velocity profiles at $X/L = 0.978$ and $R/R_{max} = 0.25, 0.30, 0.35, 0.40, 0.50$, and 0.60 for body with sail at an angle of yaw of two degrees.

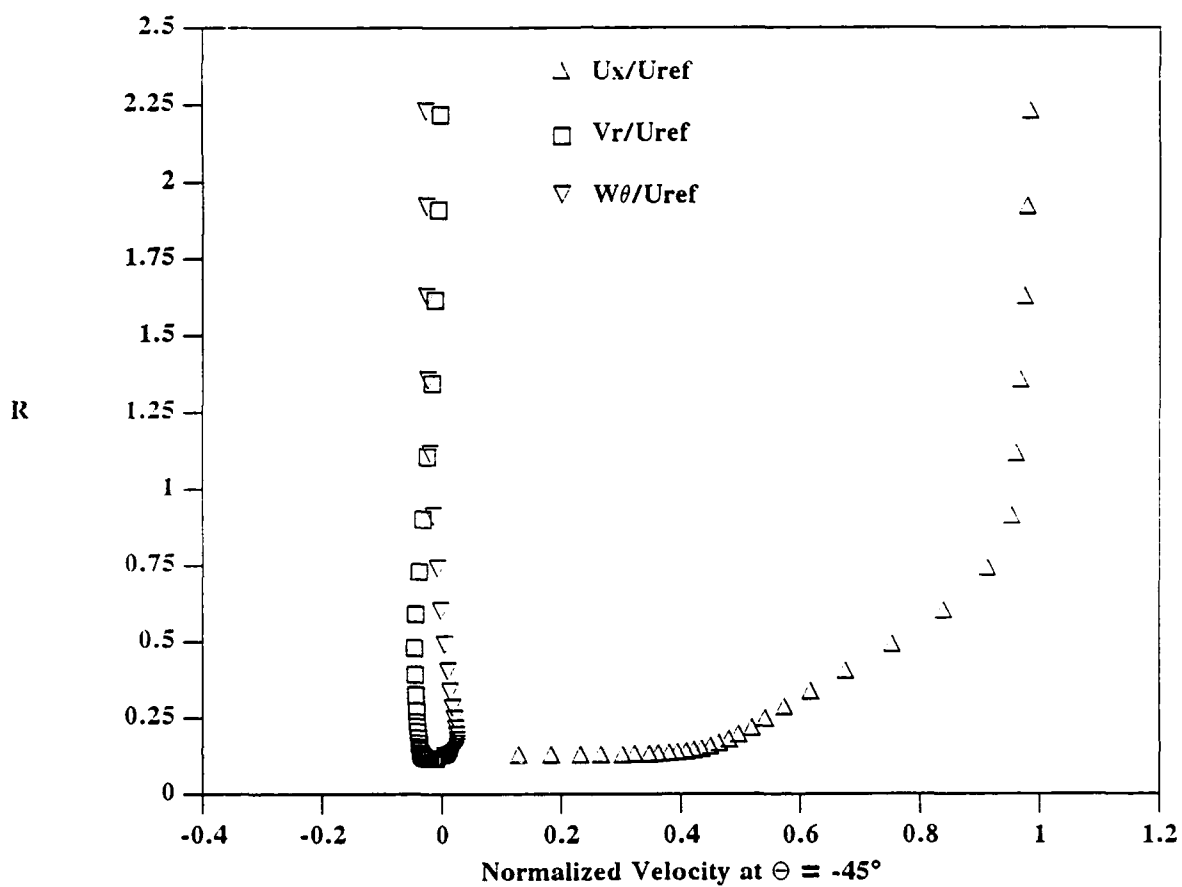


Fig. 44. Mean velocity profiles on the leeward side of the hull at $X/L = 0.978$ for body with sail at an angle of yaw of two degrees.

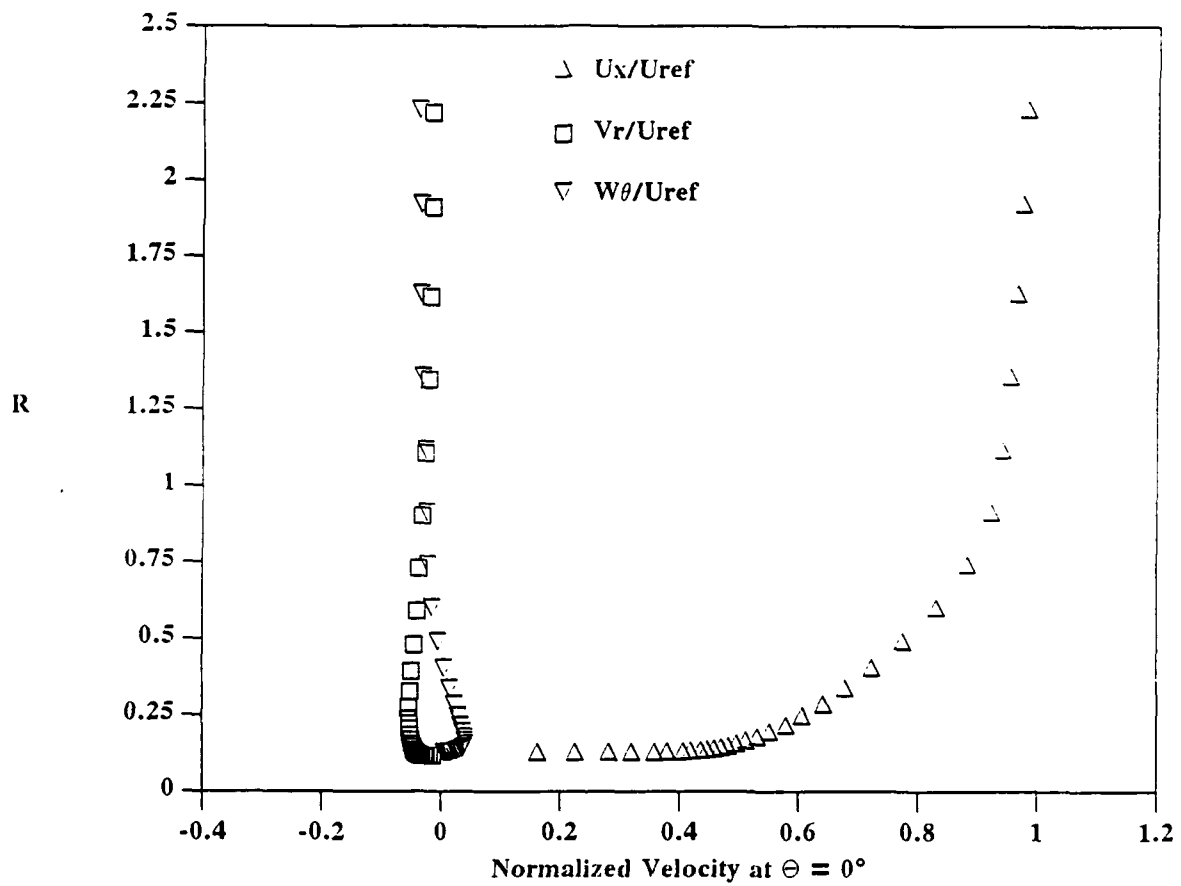


Fig. 45. Mean velocity profiles in the top center plane at $X/L = 0.978$ for body with sail at an angle of yaw of two degrees.

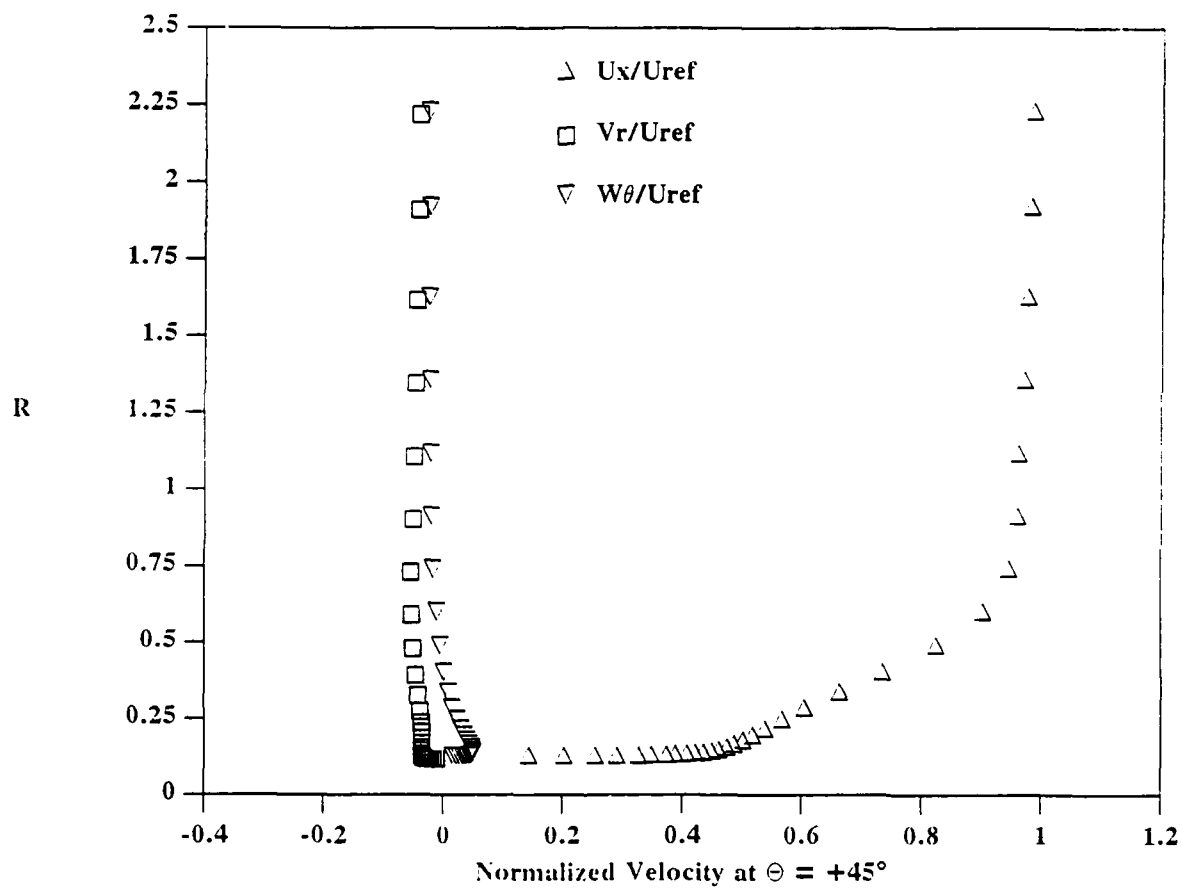


Fig. 46. Mean velocity profiles on the windward side of the hull at $X/L = 0.978$ for body with sail at an angle of yaw of two degrees.

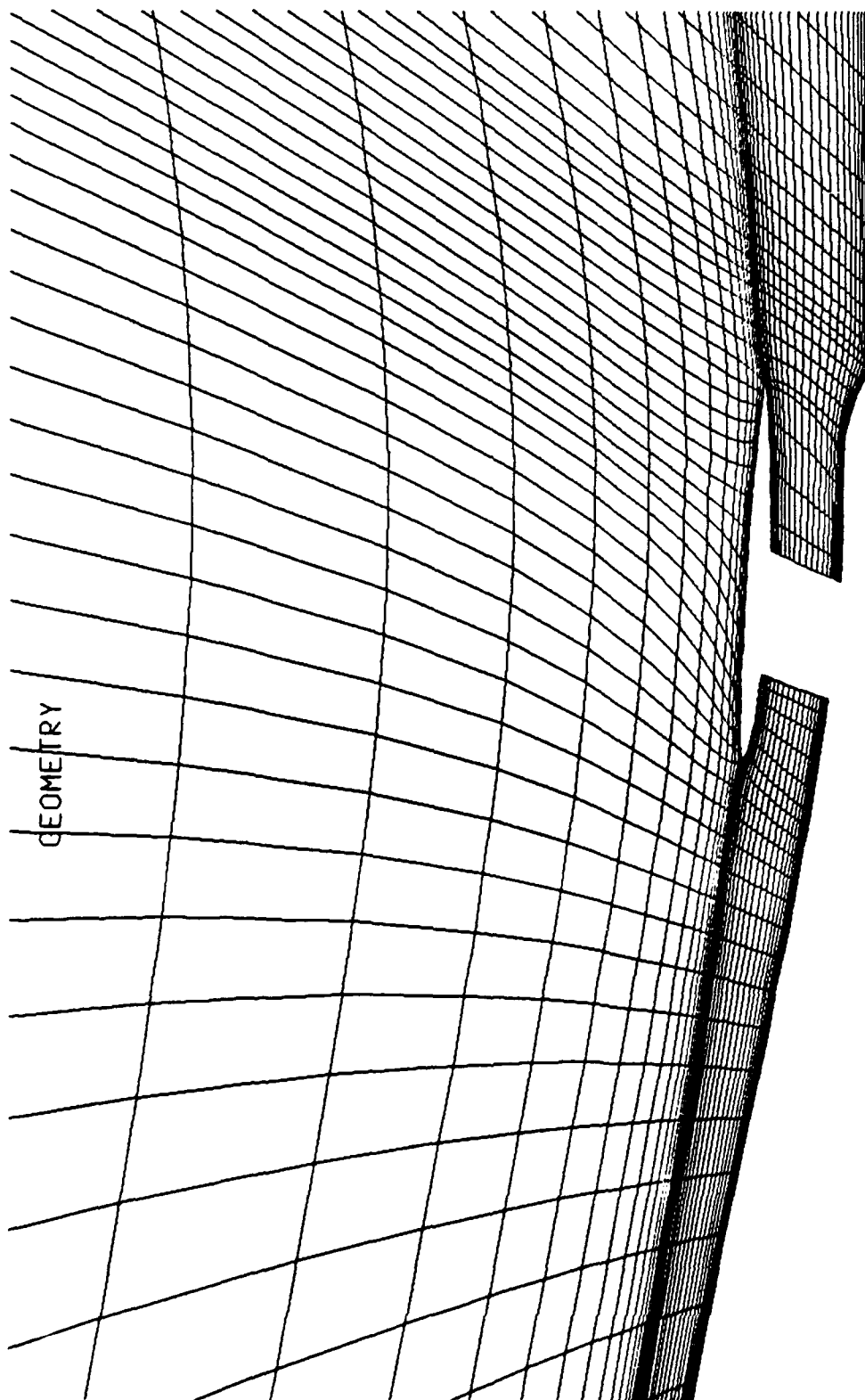


Fig. 47. Grid cross section in strut center plane of body with ring wing 1.

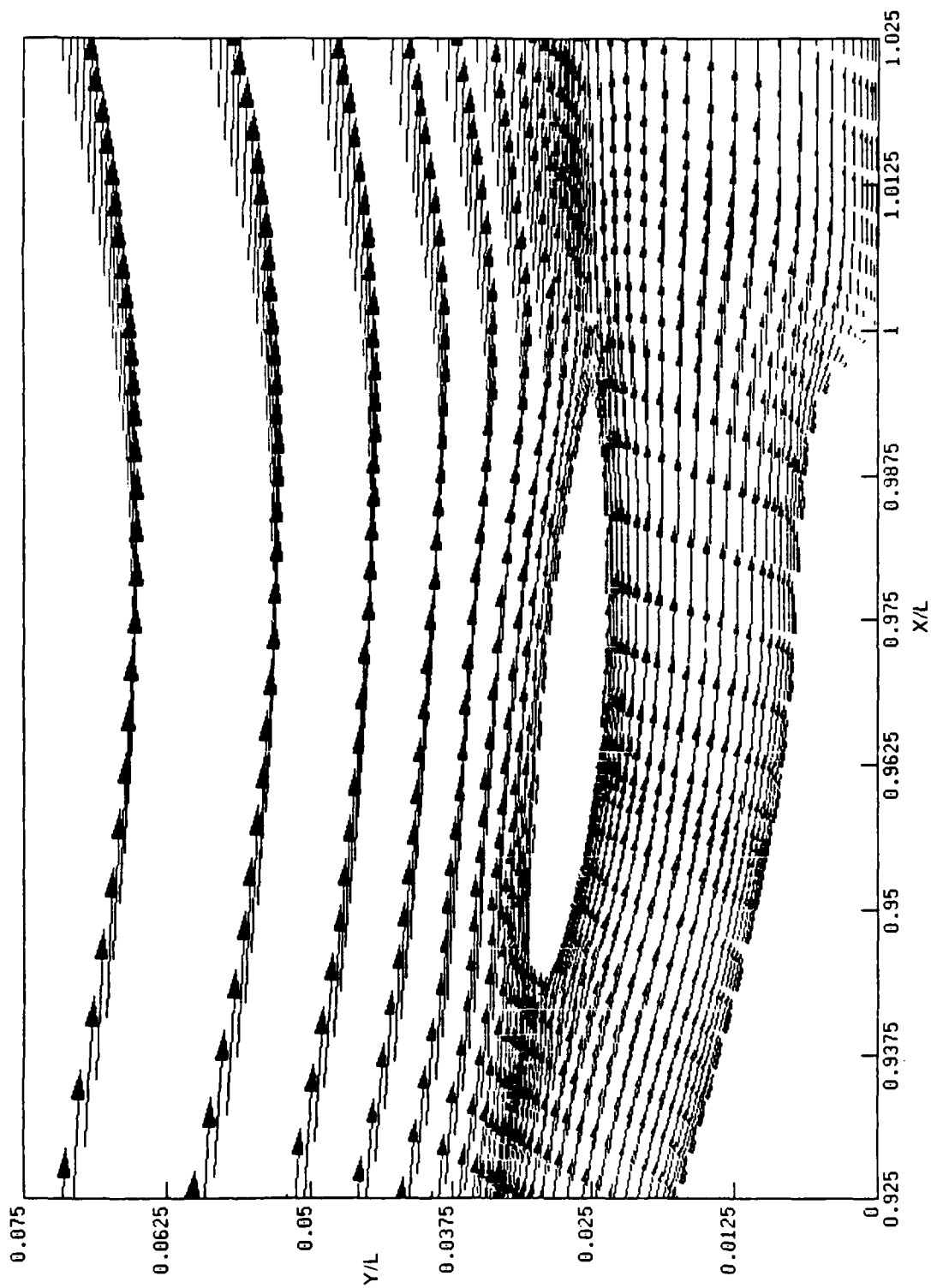


Fig. 48. Velocity vectors in top center plane for body with ring wing 1.

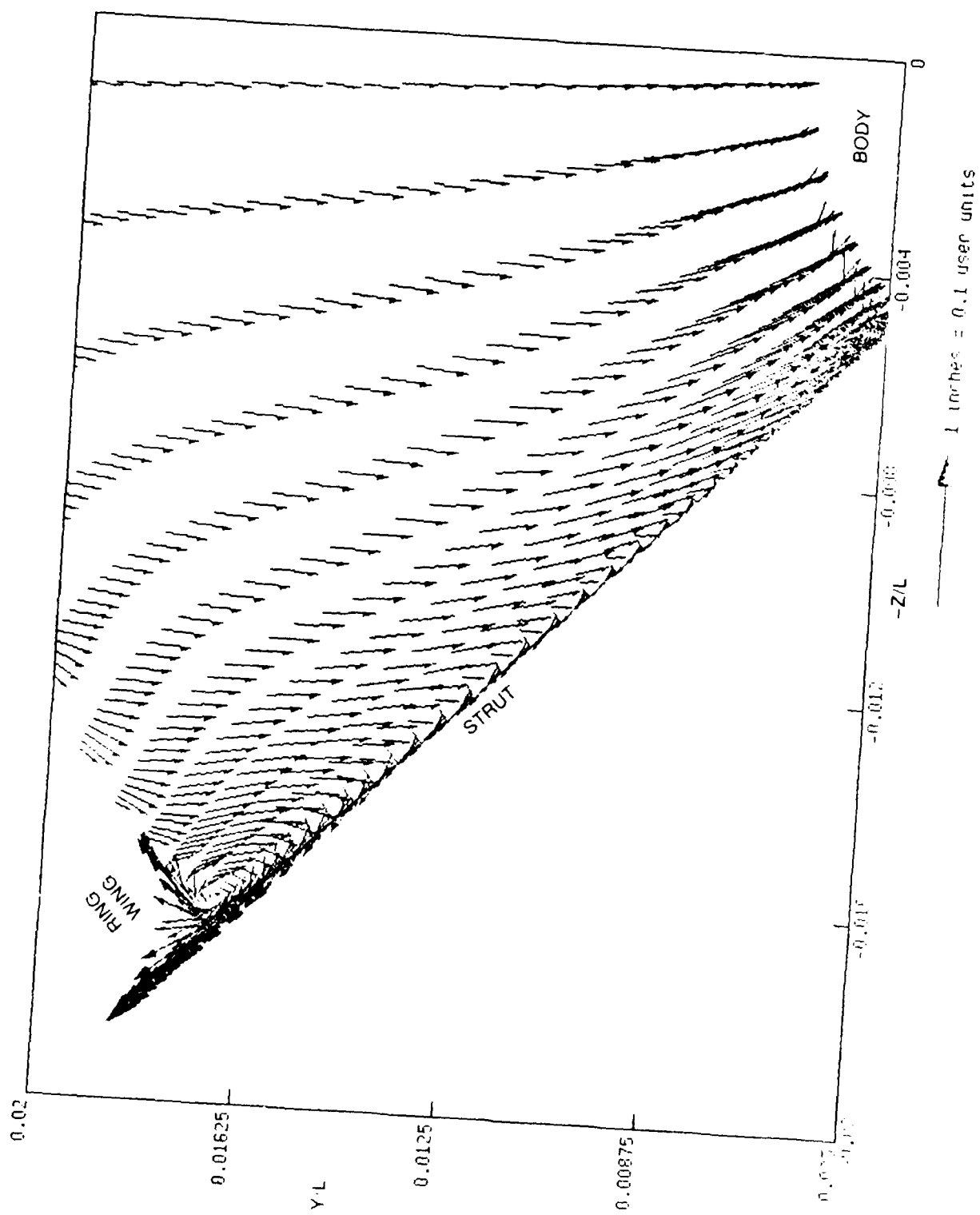


Fig. 49. Crossflow velocity vectors at $X/L = 0.97$ for body with ring wing 1.

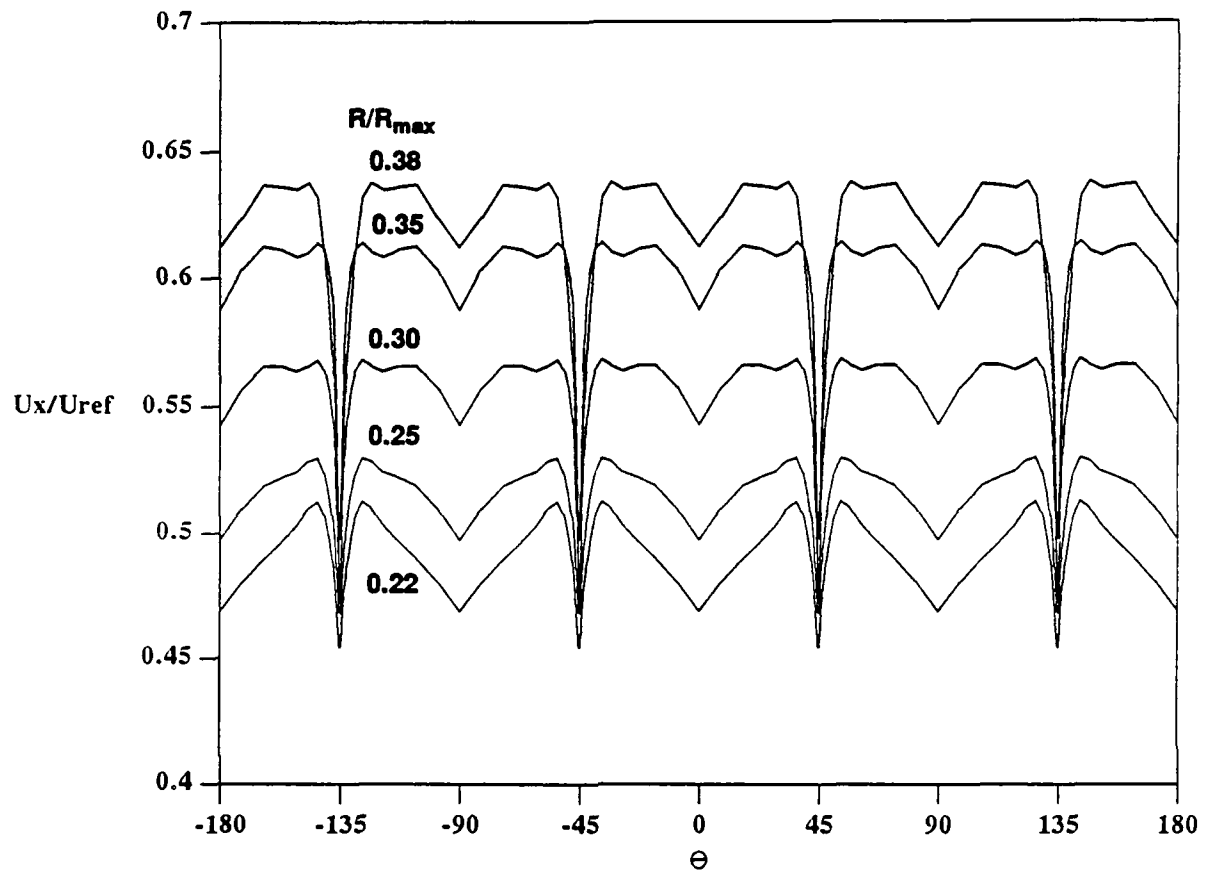


Fig. 50. Streamwise velocity profiles at $X/L = 0.978$ and $R/R_{max} = 0.22, 0.30, 0.35,$ and 0.38 for body with ring wing 1.

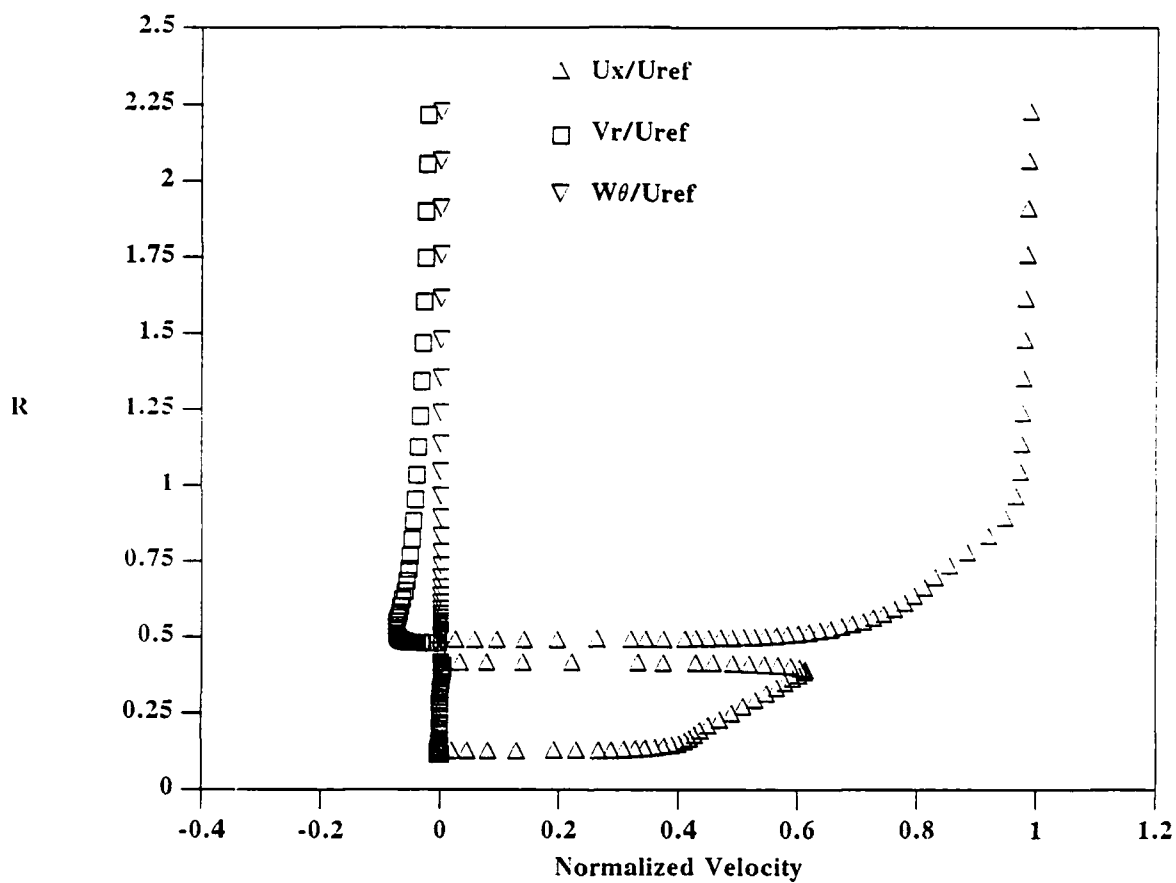


Fig. 51. Mean velocity profiles in the top center plane at $X/L = 0.978$ for body with ring wing 1.

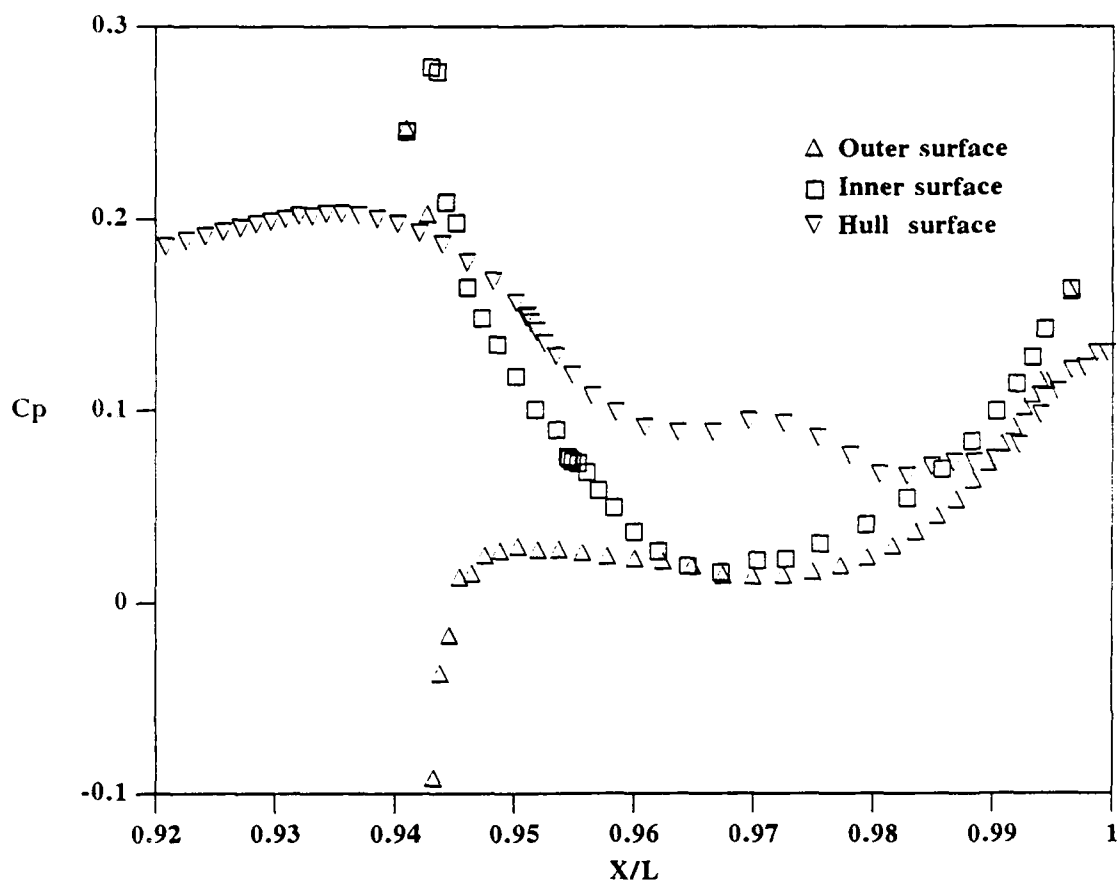


Fig. 52. Pressure coefficient on hull and ring wing 1.

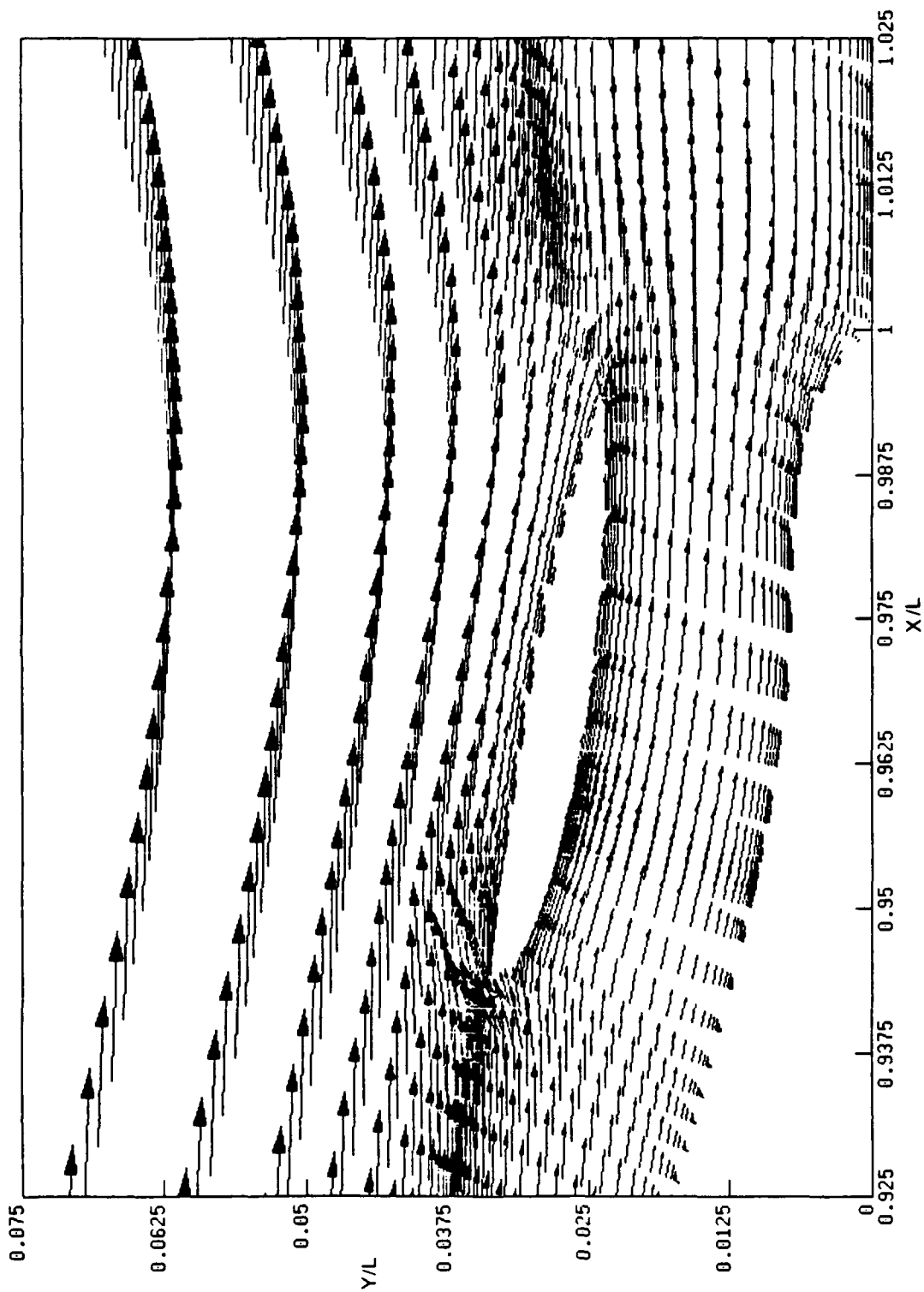


Fig. 53. Velocity vectors in top center plane for body with ring wing 2.

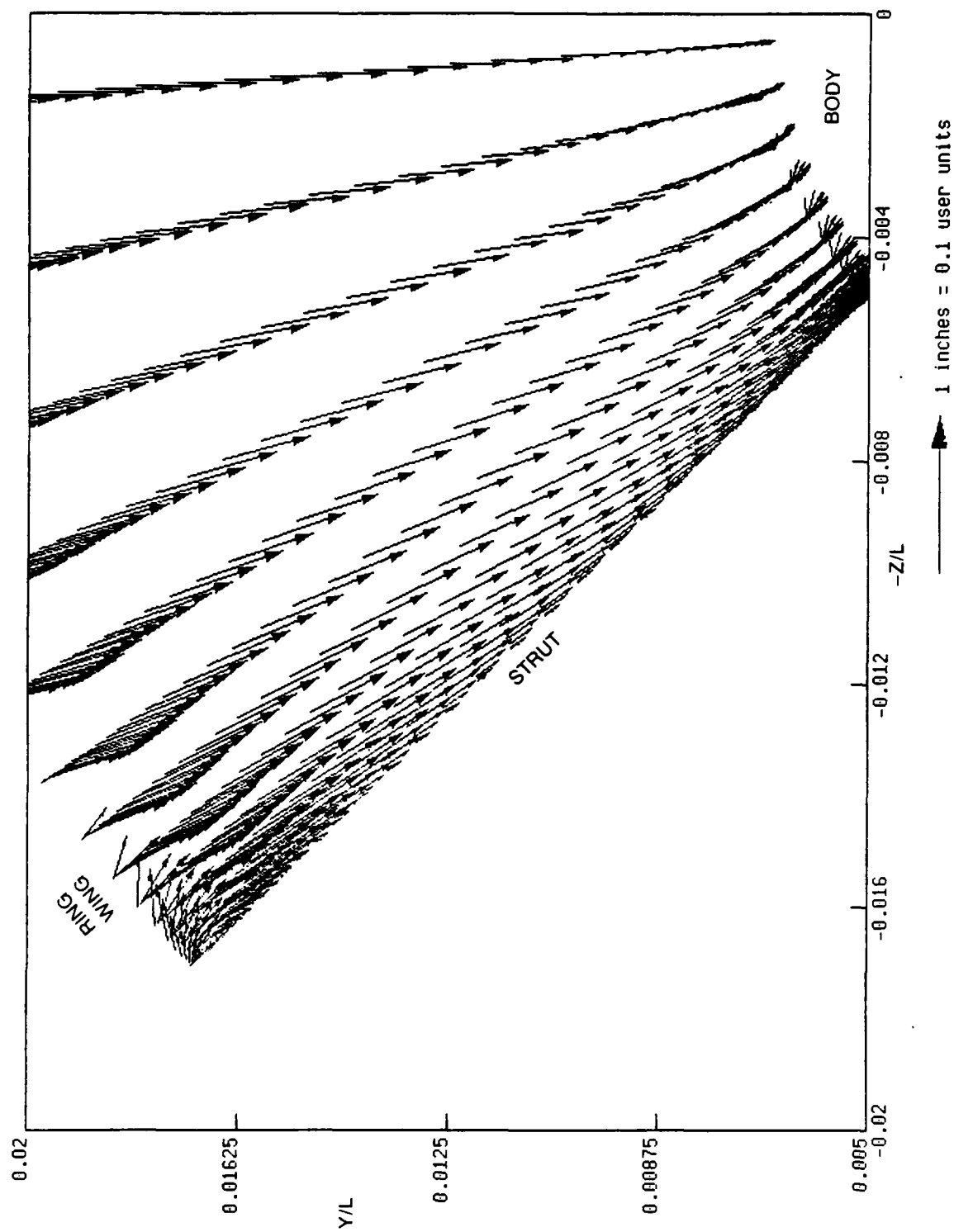


Fig. 54. Crossflow velocity vectors at $X/L = 0.97$ for body with ring wing 2.

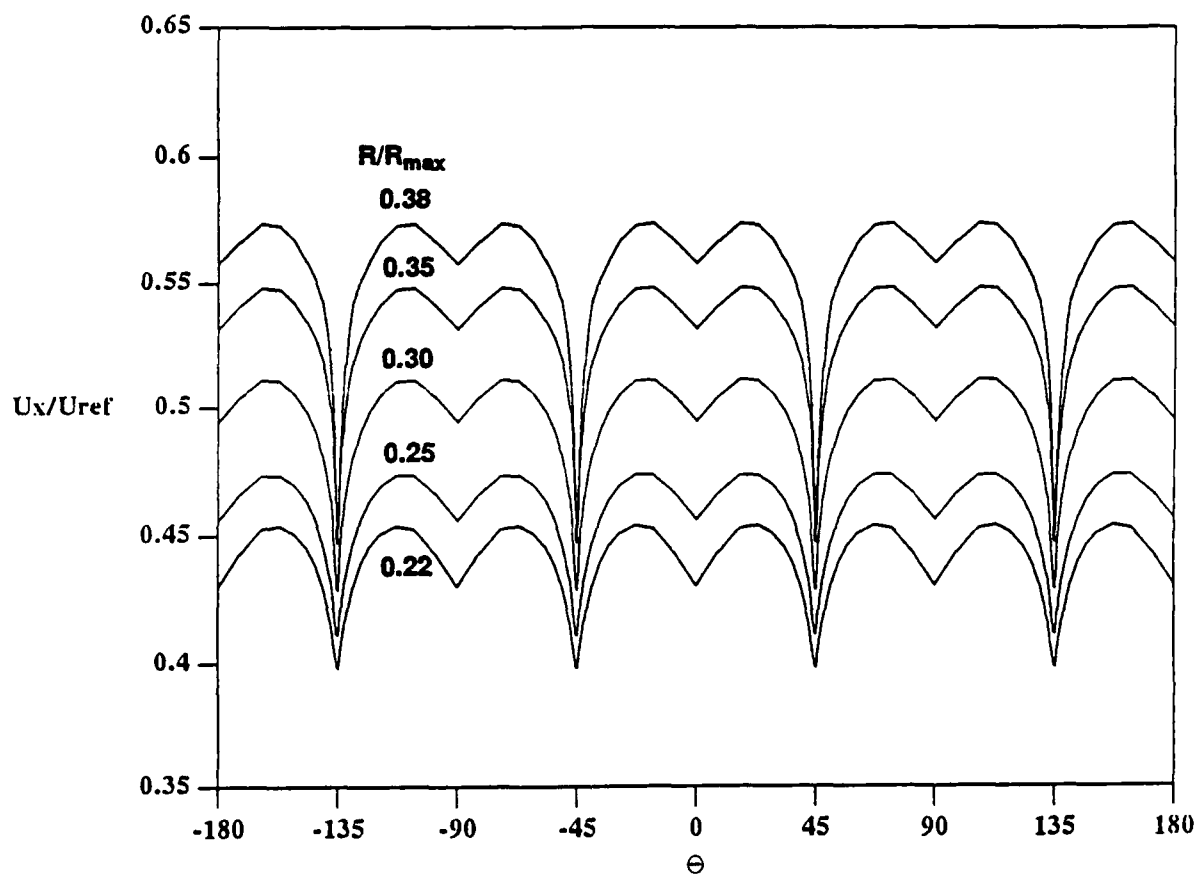


Fig. 55. Streamwise velocity profiles at $X/L = 0.978$ and $R/R_{max} = 0.22, 0.30, 0.35,$ and 0.38 for body with ring wing 2.

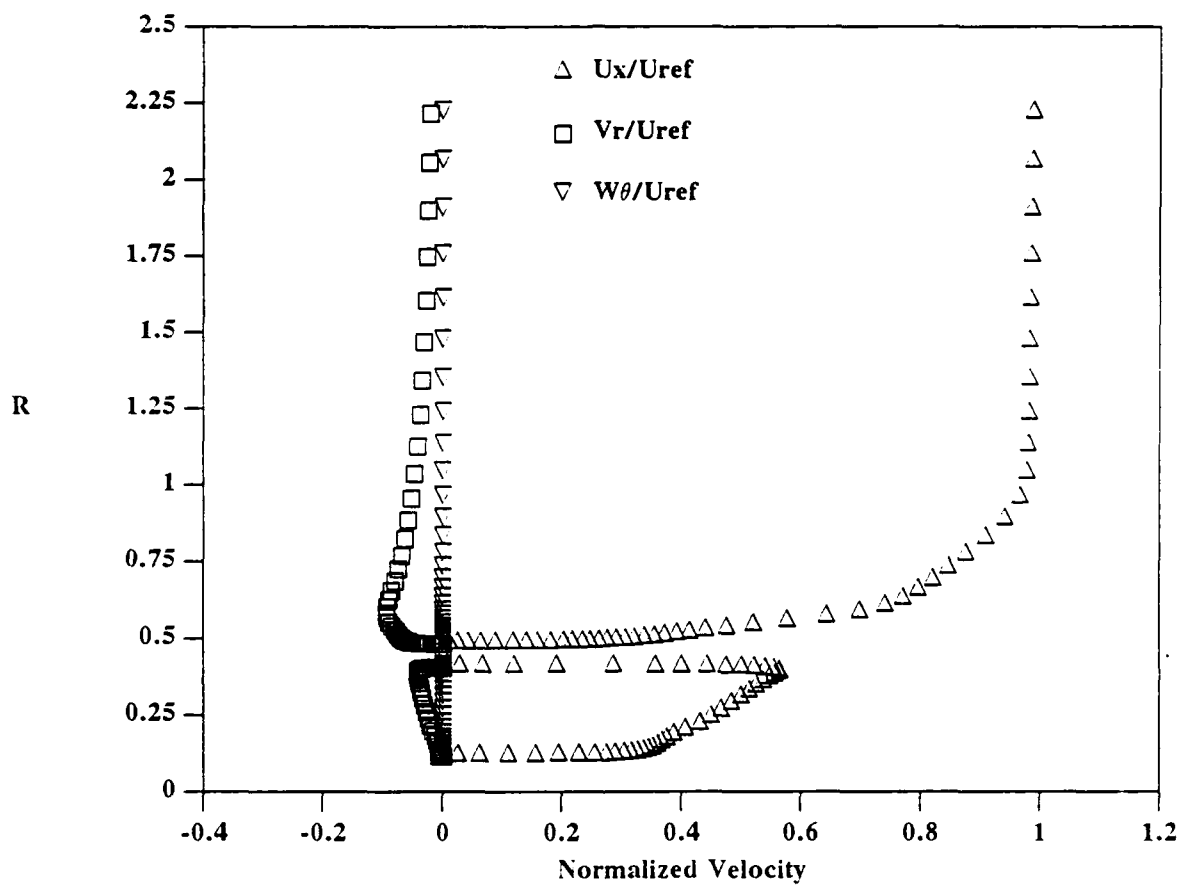


Fig. 56. Mean velocity profiles in the top center plane at $X/L = 0.978$ for body with ring wing 2.

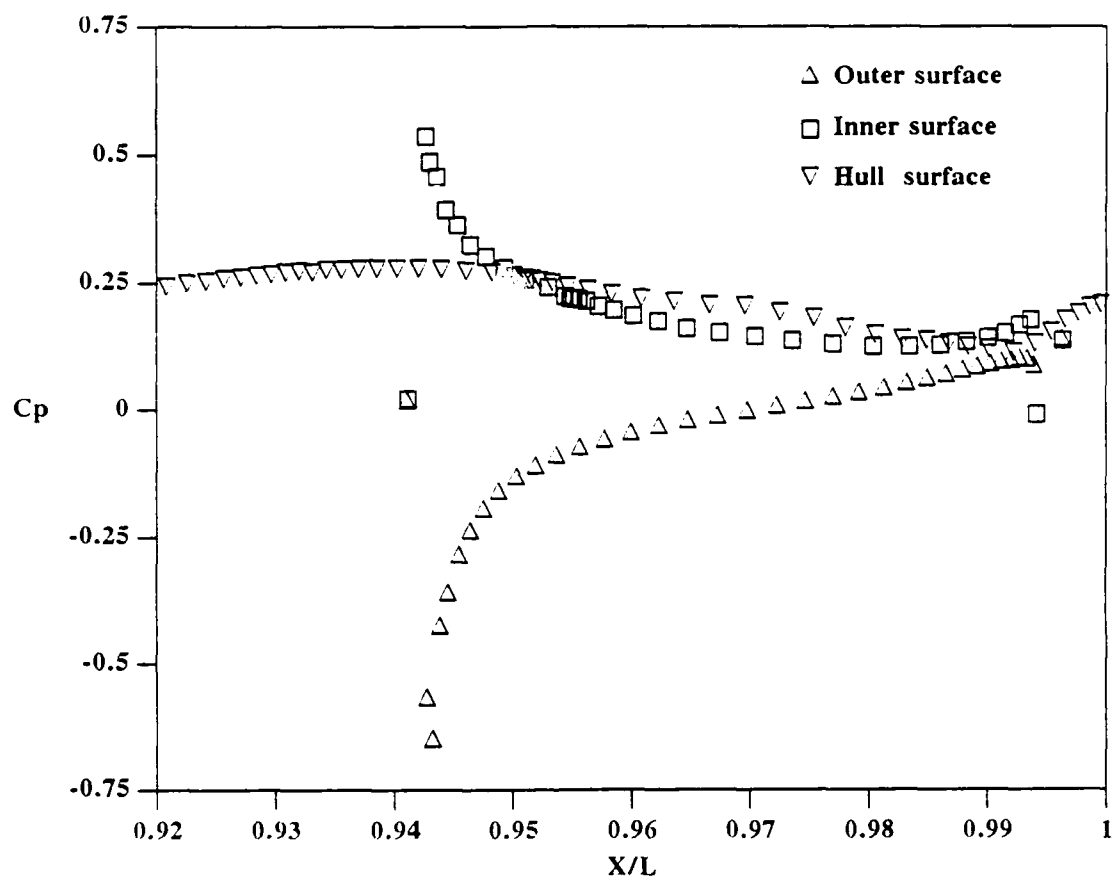


Fig. 57. Pressure coefficient on hull and ring wing 2.

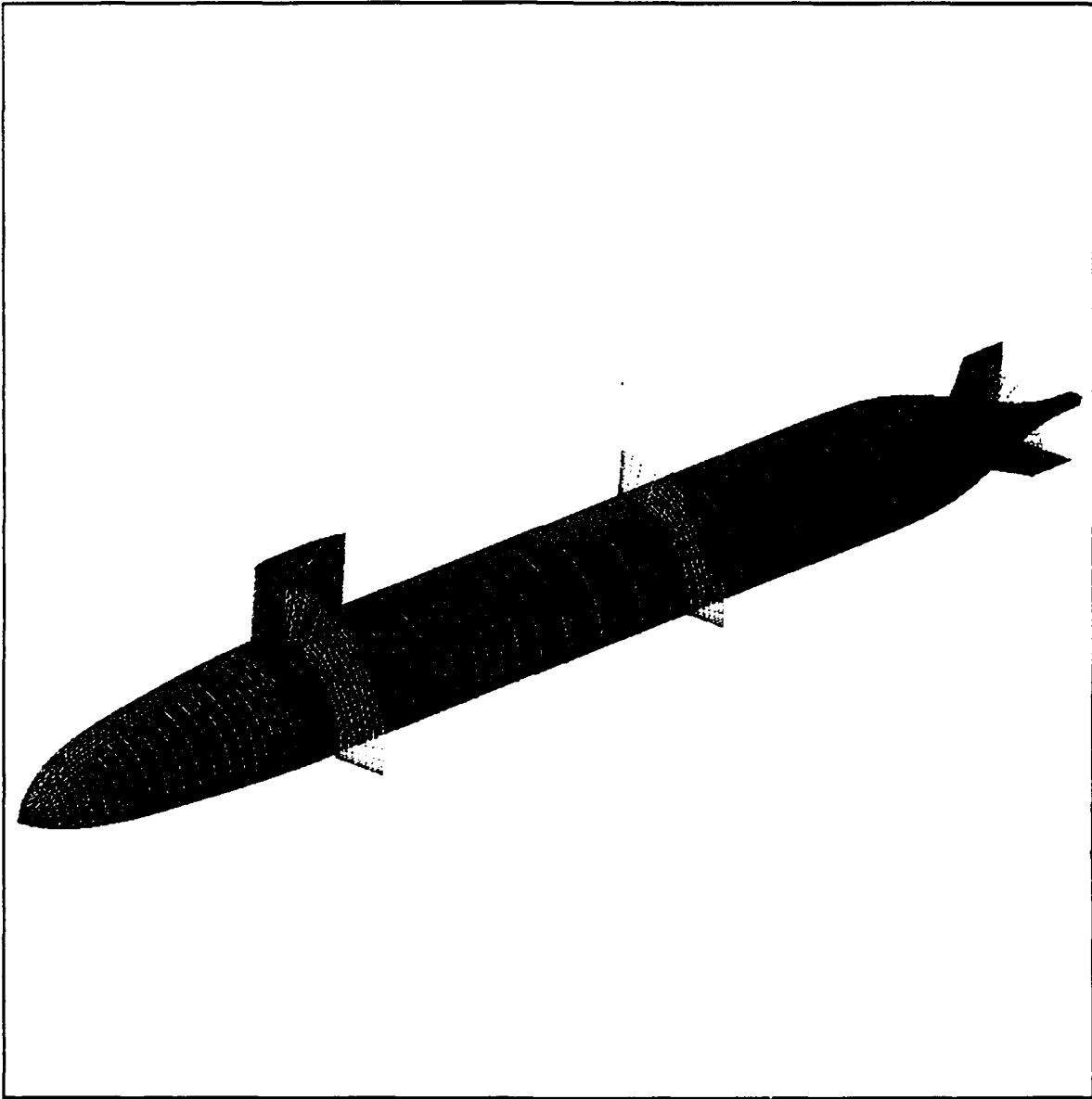


Fig. 58. Grid cross sections for hull with sail and stern planes, configuration 8.

1.00000
0.95000
0.90000
0.85000
0.80000
0.75000
0.70000
0.65000
0.60000
0.55000
0.50000
0.45000
0.40000
0.35000
0.30000
0.25000
0.20000
0.15000
0.10000
0.05000
0.00000
-0.05000
-0.10000
-0.15000
-0.20000
-0.25000
-0.30000
-0.35000
-0.40000
-0.45000
-0.50000

Pressure coefficient on hull with sail and stern planes.

Pressure coefficient on hull with sail and stern planes.

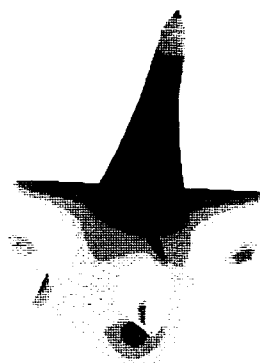


Fig. 59. Pressure coefficient on hull with sail and stern planes.

1.00000
-0.95000
-0.90000
-0.85000
-0.80000
-0.75000
-0.70000
-0.65000
-0.60000
-0.55000
-0.50000
-0.45000
-0.40000
-0.35000
-0.30000
-0.25000
-0.20000
-0.15000
-0.10000
-0.05000
0.00000
0.05000
0.10000
0.15000
0.20000
0.25000
0.30000
0.35000
0.40000
0.45000
0.50000

PRESSURE
DAPPAL W/SAIL AND STERN PLANE
DAVID TAYLOR RESEARCH CENTER

Pressure
Coefficient
Legend
Page 20



Fig. 60. Pressure coefficient in stern plane region on hull with sail and stern planes.

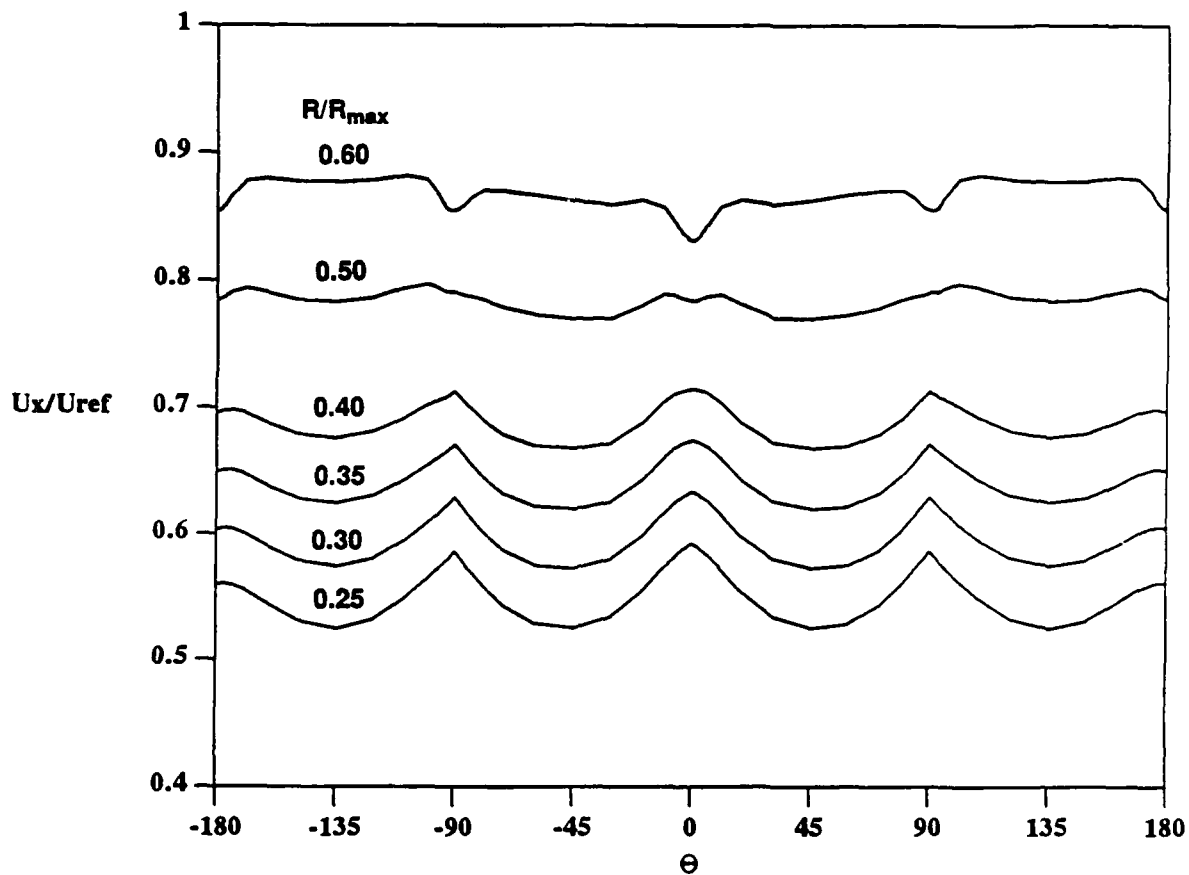


Fig. 61. Streamwise velocity profiles for body with sail and stern appendages at $X/L = 0.978$ and $R/R_{max} = 0.25, 0.30, 0.35, 0.40, 0.50$, and 0.60 .

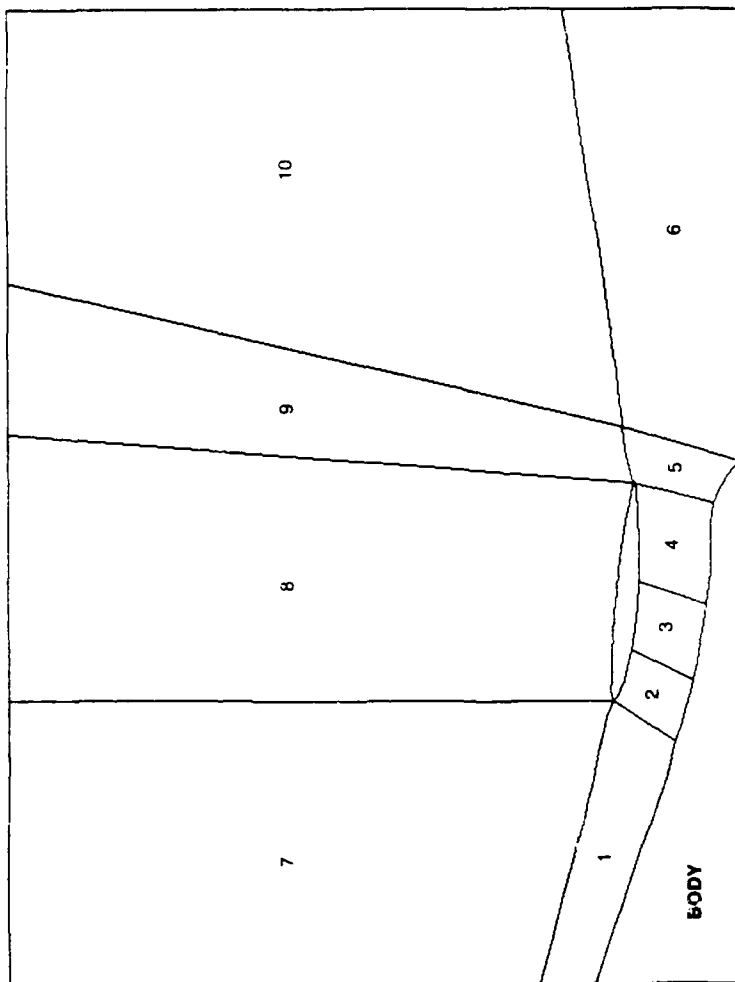
THIS PAGE INTENTIONALLY LEFT BLANK

APPENDIX

DTNS3D BOUNDARY CONDITION INPUT FOR 10-BLOCK RING WING GEOMETRY

Block No.
Boundary
Condition
Other
Parameters

1	1	NOFLOW	1	3	F	6	1	ZONALB	5	4	T
1	2	NOSLIP	0	0	F	6	2	NOFLOW	1	3	F
1	3	REFLECT	0	3	F	6	3	REFLECT	0	3	F
1	4	ZONALB	2	1	T	6	4	PRESET	0	0	F
1	5	ZONALB	7	2	T	6	5	ZONALB	10	2	T
1	6	TANGNT	0	0	F	6	6	TANGNT	0	0	F
2	1	ZONALB	1	4	T	7	1	NOFLOW	1	3	F
2	2	NOSLIP	0	0	F	7	2	ZONALB	1	5	T
2	3	REFLECT	0	3	F	7	3	REFLECT	0	3	F
2	4	ZONALB	3	1	T	7	4	ZONALB	8	1	T
2	5	NOSLIP	0	0	F	7	5	FREEST	0	0	F
2	6	TANGNT	0	0	F	7	6	TANGNT	0	0	F
3	1	ZONALB	2	4	T	8	1	ZONALB	7	4	T
3	2	NOSLIP	0	0	F	8	2	NOSLIP	0	0	F
3	3	REFLECT	0	3	F	8	3	REFLECT	0	3	F
3	4	ZONALB	4	1	T	8	4	ZONALB	9	1	T
3	5	NOSLIP	0	0	F	8	5	FREEST	0	0	F
3	6	NOSLIP	0	0	F	8	6	TANGNT	0	0	F
4	1	ZONALB	3	4	T	9	1	ZONALB	8	4	T
4	2	NOSLIP	0	0	F	9	2	ZONALB	5	5	T
4	3	REFLECT	0	3	F	9	3	REFLECT	0	3	F
4	4	ZONALB	5	1	T	9	4	ZONALB	10	1	T
4	5	NOSLIP	0	0	F	9	5	FREEST	0	0	F
4	6	TANGNT	0	0	F	9	6	TANGNT	0	0	F
5	1	ZONALB	4	4	T	10	1	ZONALB	9	4	T
5	2	NOSLIP	0	0	F	10	2	ZONALB	6	5	T
5	3	REFLECT	0	3	F	10	3	REFLECT	0	3	F
5	4	ZONALB	6	1	T	10	4	PRESET	0	0	F
5	5	ZONALB	9	2	T	10	5	FREEST	0	0	F
5	6	TANGNT	0	0	F	10	6	TANGNT	0	0	F



CORRESPONDING BLOCKS IN CROSS SECTION

INPUT

NOTE: Boundary Conditions Include —

NOFLOW — No Flow Across Boundary

NOSLIP — No Slip on a Solid Surface

REFLECT — Reflection Boundary

ZONALB — Interface Between Two Blocks

T — Indicates Grid Overlap to be Added to Maintain Accuracy Across Inter-block Boundaries.

TANGNT — Flow Tangent to Boundary

PRESET — User Programmed Condition

FREEST — Far-field Condition

The input consists of six lines for each of the 10 blocks. Each line specifies the type of boundary condition to be applied on one of the six block sides.

THIS PAGE INTENTIONALLY LEFT BLANK

REFERENCES

1. Groves, N.C., T.T. Huang, and M.S. Chang, "Geometric Characteristics of DARPA SUBOFF Models," David Taylor Research Center, Ship Hydromechanics Dept. Report DTRC/SHD-1298-01 (1989).
2. Huang, T.T., H.-L. Liu, N.C. Groves, "Experiments of the DARPA SUBOFF Program," DTRC Report SHD-1298-02 (1989).
3. Coleman, R.M., "Generation of Boundary-Fitted Coordinate Systems Using Segmented Computational Regions," in Numerical Grid Generation (Ed. Thompson, J.F.), pp. 633-651, *Proceedings of a Symposium on the Numerical Generation of Curvilinear Coordinate Systems*, Nashville, TN, USA, 1982; Elsevier Science, New York (1982).
4. Coleman, R.M. and M.L. Brabanski, "Numerical Grid Generation for Three-Dimensional Geometries Using Segmented Computational Regions," in Numerical Grid Generation in Computational Fluid Dynamics (Ed. Häuser, J. and Taylor, C.), pp. 197-216, *Proceedings of the International Conference on Numerical Grid Generation in Computational Fluid Dynamics*, Landshut, West Germany, 1986. Pineridge Press, Swansea, United Kingdom (1986).
5. Coleman, R.M., "Adaptive Techniques for Boundary Grid Generation," in Numerical Grid Generation in Computational Fluid Dynamics '88 (Ed. Sengupta, S. et al.), pp. 339-349, *Proceedings of the Second Conference on Grid Generation in Computational Fluid Dynamics*, Miami, FL, USA, 1988; Pineridge Press, Swansea, United Kingdom (1988).
6. Chakravarthy S.R. and S. Osher, "A New Class of High Accuracy TVD Schemes for Hyperbolic Conservation Laws," AIAA Paper No. 85-0363 (1985).
7. Gorski, J.J., "Multiple Block Calculations of the Navier-Stokes Equations for Incompressible Flows," *Proceedings of the 12th U.S.-Federal Republic of Germany Data Exchange Meeting*, Bethesda, MD, USA (1988).
8. Gorski, J.J., "Solutions of the Incompressible Navier-Stokes Equations Using an Upwind-differenced TVD Scheme," in Lecture Notes in Physics, Vol. 323 (Ed. Dwoyer, D.L., Hussaini, M.Y. and Voigt, R.G.), pp. 278-282, *Proceedings of the 11th International Conference on Numerical Methods in Fluid Dynamics*, Williamsburg, VA, USA, 1988; Springer-Verlag, Berlin and Heidelberg, West Germany, (1989).
9. Gorski, J.J., "TVD Solutions of the Incompressible Navier-Stokes Equations with an Implicit Multigrid Scheme," AIAA Paper No. 88-3699, in *Proceedings of the AIAA/ASME/SIAM/APS First National Fluid Dynamics Congress*, Vol. 1, pp. 394-401, 1988; American Institute of Aeronautics and Astronautics, Washington, DC (1988).
10. Gorski, J.J., "Incompressible Cascade Calculations Using an Upwind Differenced TVD Scheme," in Advances and Applications in Computational Fluid Dynamics (Ed. Baysal, O.), Vol. 66, pp. 61-69, *Proceedings of the ASME Winter Annual Meeting*, Chicago, IL, USA, 1988; American Society of Mechanical Engineers, New York (1988).
11. Gorski, J.J., "A New Near-Wall Formulation for the $k-\epsilon$ Equations of Turbulence," AIAA Paper No. 86-0556 (1986).
12. Haussling, H.J., J.J. Gorski, and R.M. Coleman, "Computation of Incompressible Fluid Flow About Bodies with Appendages," *Proceeding of the International Seminar on Supercomputing in Fluid Flow*, Lowell, MA, USA, (1989).

13. Brabanski, M.L., "DPAC: A Code for Interactive Curve Parameterization," DTRC Report CMLD-87/34 (1987).
14. McKee, J.M. and R.J. Kazden, "G-PRIME B-spline Manipulation Basic Mathematical Subroutines," DTRC Report 77/0036 (1977).
15. Lin, C.-W., G. Smith, and S. Fisher, "Numerical Flow Simulation on DARPA Submarine Configurations," DTRC Ship Hydromechanics Dept. Report, in preparation.

INITIAL DISTRIBUTION

Copies

- 1 DARPA/G. Jones
- 4 ONR
 - 1 1121 S. Ramberg
 - 1 1132F S. Lekoudis
 - 1 1132F E. Rood
 - 1 1215 J. Fein
- 1 USNA/B. Johnson
- 4 NRL
 - 1 4400 J. Boris
 - 1 4401 W. Sandberg
 - 1 4420 H. Wang
 - 1 4430 D. Fyfe
- 3 NAVSEA
 - 1 55W E. Comstock
 - 1 55W3 H. Chatterton
 - 1 55W33 C. Chen
- 1 NUSC
 - 1 44 A. Carlson
- 12 DTIC
- 2 Boeing Aircraft Company
 - 1 A. Mitchell
 - 1 W.-H. Jou
- 1 C.S. Draper Laboratory
 - 1 T.F. Tureaud
- 1 Batelle Research
 - 1 A.J. Bruckheim
- 2 Jason Associates Corp.
 - 1 P.I. Nakayama
 - 1 J. Taft
- 1 Los Alamos National Lab.
 - 1 W. Gregory

Copies

- 2 McDonnell Douglas Corp.
 - 1 T. Cebeci
 - 1 D.N. Smyth
- 1 Sandia National Laboratory
 - 1 J. Nunziato
- 2 Science Applications International Corp.
 - 1 N. Salvesen
 - 1 D.R. Thayer
- 2 University of Iowa
 - 1 V.C. Patel
 - 1 F. Stern
- 1 ARL/Penn. State Univ.
 - 1 R.E. Henderson
- 2 Mass. Inst. of Tech.
 - 1 Dept. of Ocean Eng./
P. Slavounos
 - 1 Dept. of Mech. Eng./
A. Patera
- 1 Univ. of Missouri - Rolla
 - 1 Dept. of Mech. and Aero. Eng./
S. C. Lee
- 1 Arnold Eng. Dev. Center
 - 1 J.A. Benek
- 1 Newport News Shipbuilding
 - 1 J.M. Miller
- 1 Calif. Research & Technology
 - 1 T. Isbelle
- 1 Bolt, Beranek & Newman
 - 1 S. Breit
- 1 Johns Hopkins Univ.
 - 1 Dept. of Biomedical Eng./
A.S. Popel

CENTER DISTRIBUTION

Copies	Code	Name	Copies	Code	Name
1	1235	G. Lamb	1	3510	G. Gray
1	1270	J. Slomski			
1	1270	T. Tai	1	342.1	TIC (C)
			1	342.2	TIC (A)
1	15	W.B. Morgan	10	3432	Reports Control
1	1500	D. Goldstein			
1	1501	W.-C. Lin			
1	1501	R. Coleman			
1	1501	J. Gorski			
25	1501	H. Haussling			
5	1504				
1	1521	W. Lindenmuth			
1	1522	M. Wilson			
1	154	J. McCarthy			
1	1541	B. Webster			
1	1542	T. Huang			
1	1542	Y.-T. Lee			
1	1543	P. Purtell			
1	1543	D. Coder			
1	1544	F. Peterson			
1	1544	C. Dai			
1	1544	K.-H. Kim			
1	1544	A. Reed			
1	1544	C.-I. Yang			
1	156	D. Cieslowski			
1	1564	J. Feldman			
1	1564	R. Ames			
1	1564	M. Martin			
1	17	M.A. Krenzke			
1	18	G. Kerr			
1	1802	H. Lugt			
1	184	M. Hurwitz			
2	1843	R. VanEseltine			
1	1843	R. Miller			
1	19	M.M. Sevik			
1	2704	E. Quandt			
1	2720	B. Hwang			
1	2740	Y.F. Wang			
1	2741	T. Calvert			
1	2741	F. Rodriguez			